Dissertation zur Erlangung des Doktorgrades
der Fakultät für Chemie und Pharmazie
der Ludwig-Maximilians-Universität München

Nanostructured Transparent Conducting Oxide Electrodes through Nanoparticle Assembly

Von

Yujing Liu

Henan, China

2012

Erklärung

Diese Dissertation wurde im Sinne von § 7 der Promotionsordnung vom 28. Novermber 2011 von Herrn Professor Dr. Thomas Bein von der Fakultät für Chemie und Pharmazie betreut.

EIDESSTATTLICHE VERSICHERUNG

Diese Dissertation wurde selbständig, ohne unerlaubte Hilfe erarbeitet.

München, den……

....

(Unterschrift des Autors)

Dissertation eingereicht am 7. Februar 2012

1. Gutachter: Prof. Dr. Thomas Bein

2. Gutachter: Prof. Dr. Christina Scheu

Mündliche Prüfung am 5. März 2012

Acknowledgements

At the end of the thesis writing, I would like to express my deep gratitude to all the people who have helped me with last three years' research work and last several months' intensive writing. Without their support and encouragements, there won't be the realization of this thesis.

First of all, I would like to say many thanks to the DAAD/Siemens post-graduate program. Without the financial support, I would not have had the chance to come here and finish my PhD study. Then, I would like to express my gratitude to Professor Thomas Bein, thank you to give me the opportunity to work in such a dynamic research group and thank you for the suggestions you gave during the subgroup-meetings. I must also extend my gratitude to my thesis mentor Dr. Dina Fattakhova-Rohlfing, for her great patience, efficient guidance and lots of help. I also want to thank Professor Christina Scheu for her kindness to be the second reviewer on my thesis.

I am grateful to all my fellow colleagues in AK Bein, thanks for their friendly greetings when I came into the group, for their assistance in using the experimental instruments, for their delicious cakes from time to time. They are Karin, Andreas, Camilla, Monica, Markus, Andrea, Shaofeng, Kun, Axel, Jörg, Mirjam, Fabian, Christian, Bastian, Stefan (Wuttke), Stefan (Niedermayer), Alex, Maria, Xinyi, Dana, Florian (Hinterholzinger) and all the others in the group. Additionally, sincere gratitude to the members in the PV subgroup, Johann, Vesna, Hans, Benni, Mihaela, Norma, Florian (Auras), Alesja, Ashkat, Halina and Professor Laurie Peter, for lots of discussions and suggestions. Thanks to my Praktikum-students, Julia, Diandian and Ben for their nice work. I also would like to give my thanks to Regina and Tina, I am very impressed by your organization and efficient work, thank you very much! Specially, I must say great thanks to Yan, thank you so much for all the sharing of happy and difficult moments in our PhD life.

Besides, I would like to say many thanks to Steffen (Schmidt), for TEM measurements and for the support as an office mate in my thesis writing! Many thanks to Bastian, Benni and Florian

(Auras) for SEM measurements. Many thanks to the Wintterlin group for the XPS measurements, specially, to Professor Guenther and Patrick!

Great thanks must also go to our collaboration partners: Haiyan Sun from Department of Physics in LMU (group of Professor Lukas Schmidt-Mende); Dr. Jiri Rathousky from J. Heyrovský Institute of Physical Chemistry, Academy of Sciences of the Czech Republic; Dr. Goran Stefanic from Division of Materials Chemistry, Ruđer Bošković Institute, Zagreb, Croatia; Dr. Hynek Němec from Institute of Physics, Academy of Sciences of the Czech Republic, Prague; and the organic photodiode group in Siemens, Erlangen, Dr. Oliver Hayden, Dr. Maria Sramek, Dr. Sandro F. Tedde, Francesco Arca, Regina Pflaum and Moses Richter. It's the effective collaboration that made this thesis successful, thank you all very much!

Last but not least, I am greatly indebted to my family members and all my friends. Their love, support and encouragement give me the energy and strength to go through all the challenging moments in my life abroad. Thanks!

Abstract

Transparent conducting oxides (TCOs), combining high electrical conductivity and high optical transparency in the visible spectrum, are widely applied as planar electrodes in optoelectronic and electrochemical devices. Development of nanostructured TCO materials with a 3D periodic architecture featuring a large interface area and interconnected conductive framework can substantially increase the applicability of TCO materials, paving ways for new efficient devices. The objective of this thesis is the elaboration of nanostructured TCO electrodes with defined 3D porous morphologies and further tests of their structural advantages in related devices.

Templated self-assembly of preformed crystalline TCO nanoparticles is the major strategy employed in this work to fabricate nanostructured TCO electrodes. Compared with the conventional template synthesis utilizing molecular precursors, this approach offers a number of advantages such as a good control over the formation of crystalline porous frameworks at mild temperatures and the use of commercially available templates. The successful application of this method is however restricted by the availability of suitable nanoparticles. The nanoparticles should be just a few nanometers in size with a narrow size distribution, well dispersible in various solvents to form stable colloidal solutions, and compatible with template species such as block copolymers or polymer colloids. Thus, development of procedures for the formation of suitable TCO nanoparticles and their templated self-assembly are two significant parts of this thesis.

One of the TCO systems investigated in this thesis is niobium doped titanium oxide (NTO), which was recently reported as a promising conducting oxide. We have developed a novel nonaqueous sol-gel approach for the synthesis of Nb-doped titania nanoparticles using tert-butanol as the reaction medium and oxygen source. This reaction enables the generation of non-agglomerated NTO nanoparticles with a size of about 4-5 nm. We have tested the applicability of the as-synthesized nanoparticles for the assembly of mesoporous films using the commercial

Pluronic F127 polymer as a structure-directing agent. Besides, we have also employed Hall Effect measurements and time-domain terahertz spectroscopy to investigate the electrical conductivity and conduction mechanism in the niobium doped titania nanoparticles (chapter 4, collaboration with Dr. Hynek Nemec and Prof. Petr Kuzel from the Institute of Physics of Academy of Sciences of the Czech Republic, Prague).

Another TCO system studied in this project was tin doped indium oxide (ITO). Although ITO is a very well established TCO system, the development of new ITO morphologies is still in progress. Crystalline ITO nanoparticles can be synthesized by different protocols, but the available nanoparticles are not small enough for their use as building blocks for the nanostructure assembly, and their dispersibility in different solvents is too low. We have developed an alternative strategy to form crystalline mesoporous ITO materials based on the initial formation of indium tin hydroxide nanoparticles, their assembly into periodic mesostructures directed by an amphiphilic polymer, and the subsequent transformation to mesoporous indium tin oxide, as described in chapter 5. A new type of crystalline hexagonal indium tin hydroxides nanoparticles has been developed in our work using solvothermal reactions in ethylene glycol. The obtained particles are only a few nanometers in size, nearly spherical, well dispersible in water and crystallize into the cubic ITO phase at a mild temperature of 300 ^{o}C. The facile transformation of the assembled nano-hydroxides into crystalline ITO with similar morphology makes the hydroxide/oxide approach a very promising tool for the fabrication of various ITO nanostructures. The obtained indium tin hydroxides can be assembled into regular mesoporous ITO architectures featuring the large pore size directed by a commercially available Pluronic polymer. The resulting ITO layers can accommodate large amounts of redox-active molecules and serve as efficient conducting electrodes with a very high surface area.

The perfect dispersibility and solubility of indium tin nanohydroxides in water further extends the choices of templates aimed at formation of porous TCO materials with a larger pore size. In chapter 6, 3D porous conducting ITO films with large pores of about 70 nm and 250 nm were fabricated in a simple one-step co-assembly procedure. Implementation of the resulting nanostructured ITO film in organic solar cells provides a very promising strategy to enhance their current collection efficiency. As described in chapter 7, the nanostructured ITO films can efficiently act as 3D current collecting electrodes in photovoltaic devices shortening the charge transport distance and thus ultimately reducing the recombination of photogenerated charges.

We have demonstrated that templated self-assembly of preformed crystalline TCO nanoparticles is a very versatile approach towards the fabrication of 3D nanostructured TCO electrodes. The developed approach should be also applicable to other functional metal oxides and other morphologies. We envision the application of this strategy for the elaboration of hierarchical and multi-composite nanostructured materials by assembly of different types of nanoparticles, which can be used in various functional nanodevices.

List of Abbreviations

TCO	Transparent conducting oxide
3D	Three dimensional
ITO	Indium tin oxide or tin doped indium oxide
NTO	Niobium doped titanium oxide
ATO	Antimony doped tin oxide
FTO	Fluorine doped tin oxide
SDA	Structure directing agent
CCT	Colloidal crystal templating
EISA	Evaporation-induced self assembly
KLE	Poly(ethylene-co-butylene)-b-poly(ethylene oxide)
PIB-PEO	Poly(isobutylene)-b-poly(ethyleneoxide)
Pluronic F127	Poly((ethylene oxide)$_{106}$-(propylene oxide)$_{70}$-(ethylene oxide)$_{106}$)
PMMA	Poly (methyl methacrylate)
PS	Polystyrene
SEM	Scanning electron microscopy
TEM	Transmission electron microscopy
HRTEM	High resolution transmission electron microscopy
XRD	X-ray diffraction
FWHM	Full width at half maximum
XPS	X-ray photoelectron spectroscopy
E_B	Binding energy
E_K	Kinetic energy

TGA	Thermo-gravimetric analysis
DSC	Differential scanning calorimetry
DLS	Dynamic light scattering
BET	Brunauer-Emmett-Teller
THz	Terahertz
CVA	Cyclic voltammetry
Eg	Band gap energy
THF	Tetrahydrofuran
EtOH	Ethanol
TEOS	Tetra-ethoxy silane
Tert-BuOH	Tert-butanol
PDDA	Poly(diallyldimethylammoniumchloride)
APTES	3-Aminopropyltriethoxysilane
P3HT	Poly(3-hexylthiophene)
PCBM	Fullerene derivative [6-6]-phenyl-C61-butyric acid methyl ester
BHJ	Bulk-heterojunction
IV	Photocurrent-voltage
FF	Fill factor
AAO	Anodic aluminum oxide
DSSC	Dye-sensitized solar cell
OPV	Organic photovoltaic

Table of figures

Figure 1.1 Commonly used transparent conducting oxide systems (left) and their multiple combinations (right) 2

Figure 1.2 Schematic descriptions of the n-type doping: with the increase of doping density; n_c is the critical concentration (Mott carrier density)..3

Figure1.3 Band-gap changes based on electron-impurity scattering and Burstein-Moss effect. E_0 is the intrinsic band-gap, E_1 is the varied band-gap due to electron-impurity scattering, E_2 is the varied band-gap due to Burstein-Moss effect. After Gupta 4

Figure 1.4 Some examples of the nanostructured TCO morphologies: (a) nanoleaves of Ga-doped In_2O_3 obtained by carbon-thermal evaporation; (b) nanobranches of ITO prepared by electron beam evaporation; (c) hierarchical nanostructure of In-doped ZnO prepared by thermal vapor evaporation; (d) columnar channel-like SnO_2 obtained by electrochemical anodization; (e) vertical nanopost ITO prepared by vacuum-based glancing angle deposition; (f) ITO nanowires prepared by laser ablation. 11

Figure 1.5 Examples of the porous ITO morphologies obtained by spin coating of ITO nanoparticle suspension...12

Figure 1.6 Formation of mesostructured materials through the co-assembly of inorganic precursors and surfactant molecules. 14

Figure 1.7 Examples of the mesoporous ITO films prepared by EISA approach from molecular precursors and different amphiphilic block co-polymer templates: (a) KLE, pore size and wall thickness of the resulting mesostructure about 16 nm × 8 nm and 7-9 nm, respectively; (b) PIB-PEO-3000, pore size and wall thickness of the resulting mesostructure about 20-25 nm and 12-18 nm, respectively; (c) PIB-PEO-20000, pore size and wall thickness of the resulting mesostructure about 35-45 nm and 8-10 nm, respectively. 16

Figure 1.8 Molecular precursor of indium tin tris-tert-butoxide. 17

Figure 1.9 SEM images of preformed opal template and inverse-opal structure. 18

Figure 1.10 Two basic approaches to fabrication of macroporous films using colloidal crystal templating: infiltration (left) and co-assembly (right). 20

Figure 2.1 Schematic illustration of X-ray scattering. 30

Figure 2.2 Secondary effects from interaction between incident electrons and materials. After Boothroyd 33

Figure 2.3 Generation of photoelectrons under the irradiation of X-rays 36

Figure 2.4 Type IV sorption isotherm 42

Figure 2.5 The recommended position of Ohmic contacts in Van der Pauw method 45

Figure 2.6 Resistance measurements on adjacent nodes 46

Figure 2.7 Hall voltage measurements on opposite nodes 48

Figure 2.8 Typical cyclic voltammogram curve for single electron transfer reaction 52

Figure 2.9 A characteristic I-V curve for organic solar cells 54

Figure 3.1 XRD patterns of as-produced NP20 TiO_2 particles prepared by solvothermal reaction in tert-BuOH at different reaction temperatures (reaction time 12 hours). 63

Figure 3.2 (a) XRD patterns of as prepared 0 %, 10 % and 20 % Nb-doped TiO_2 nanoparticles synthesized by a solvothermal reaction in tert-butanol at 100 ℃ for 1.5, 3 and 4 hours, respectively. The inset shows the position of the (101) peak. (b) Variation of the size of NP20 nanoparticles during synthesis in tert-BuOH at 100 ℃ with the reaction time. The particle size was derived from the peak broadening in the XRD patterns according to the Scherrer equation. 64

Figure 3.3 HR-TEM images of as-made NP0 (a) and NP20 (b) nanoparticles synthesized at 100 ℃ (scale bar corresponds to 5 nm), and the particle size distribution determined by DLS in tetrahydrofuran (c)...65

Figure 3.4 SEM images (top view) of MS0 (a), MS10 (b), and MS20 (c) films calcined in air at 300 ℃...67

Figure 3.5 TEM (a,c) and HR-TEM (b, d) images of MS10 (first row) and MS20 (second row) samples calcined at 300 ℃. The insets in (a, c) show the Fourier transforms of the images. 68

Figure 3.6 Small angle XRD pattern of mesostructured films MS0, MS10 and MS20 assembled from the corresponding nanoparticles after calcination at 300 ℃. 69

Figure 3.7 Wide angle XRD patterns of mesostructured films MS0 and MS20 after calcination at 300 ℃ ((101) reflection). 70

Figure 3.8 Kr adsorption isotherms at 77 K of templated mesoporous films assembled from nanoparticles with different Nb content: MS0 (black, circles), MS10 (red, squares) and MS20 (blue, triangles). All the films were calcined at 300 ℃. 71

Figure 3.9 XPS spectra of as-prepared NP20 nanoparticles synthesized in tert-BuOH at 100 ℃. The peaks were assigned according to refs. 72

Figure 3.10 Specific conductivity (black, circles) and charge carrier concentration (red, triangles) of the pellets pressed from Nb-doped nanoparticles and heated at 600 ℃ in N_2, as a function of Nb content. The axes are shown in logarithmic scale. 74

Figure 3.11 XPS of NTO particles prepared in tert-BuOH at 60 ℃ and heated in N_2 at 600 ℃ after Ar^+ polishing for 5 min (first row) and for 30 min (second row). Polishing rate is 1500 eVs^{-1}. 75

Figure 4.1 Measured real (red circles) and imaginary part (blue squares) of the permittivity of selected samples. The GHz spectra were measured by the microwave impedance analyzer whereas the THz spectra were measured by time-domain THz spectroscopy. 95

Figure 4.2 Permittivity in the THz spectral range. Symbols: measurement by time-domain THz spectroscopy, lines: fit by Equation 4.2. The red circles correspond to the real part and the blue squares represent the imaginary part of the permittivity. 96

Figure 4.3 Sketch of the real part of hopping conductivity defined by Equation 4.1 [τ_{min} = 20 fs, τ_{max} = 100 ns]. Note that both scales are logarithmic. 98

Figure 4.4 Scheme of the structure proposed to account for the depolarization fields. 100

Figure 4.5 Results of the fits of the THz permittivity for the pellets pressed from nanoparticles with varying doping level synthesized at 100 ℃ (left column), and nanoparticles with the doping level of 20 % synthesized at several temperatures (right column). Squares: as-prepared samples, circles: annealed samples. 102

Figure 4.6 Calculated contribution of conduction-band electrons to the relative permittivity. Parameters: nanoparticle diameter 4.5 nm, electron effective mass 6me, carrier density 3×10^{18} cm^{-3}. (a) Nanoparticle boundaries randomly scatter the carriers. (b) Nanoparticle boundaries reflect the carriers, i.e., the carriers are localized within the nanoparticle. 105

Figure 5.1 Morphology and crystallinity of as-produced indium tin hydroxide nanoparticles: TEM image of the dried particles (a), high resolution TEM image of a single nanoparticle (b), SAED pattern (c) and its corresponding intensity profile (d). 115

Figure 5.2 Dynamic light scattering (DLS) measurements of colloidal solutions of indium tin hydroxide nanoparticles in water: as-produced (black triangles, a) and after the addition of a few drops of acetic acid (red circles, b). The inset shows the corresponding images of the colloidal solutions in water with a concentration of 8 wt% of nanoparticles. 115

Figure 5.3 Monitoring the phase transformations of indium tin hydroxide nanoparticles at different temperatures: (a) XRD patterns and (b) thermogravimetric analysis (TG) (black curve) and differential scanning calorimetry (DSC) (green curve) of indium tin hydroxide nanoparticles. The XRD measurements were performed ex situ. For that, the as prepared indium tin hydroxide nanoparticles were heated at selected temperatures for 2 h (the red labels in Fig. 2b indicate the temperatures at which the samples were heated) and then characterized by XRD. 117

Figure 5.4 XRD pattern of indium tin hydroxide nanoparticles after calcination at 400 ℃ in air. 119

Figure 5.5 XPS (a) and Raman (b) spectra of the ITO films assembled from nano-hydroxides after calcination at 300 ℃ in air and heating at 300 ℃ in forming gas. The inset in (a) zooms in the energy region corresponding to carbon, indicating that no carbon residuals are present on the surface, and the inset in (b) zooms in the region between 1800 and 3500 cm^{-1} showing the absence of stretching vibrations of the aliphatic groups characteristic for Pluronic polymer. 120

Figure 5.6 SEM images (top view) (a, b) of mesoporous ITO films assembled from nano-hydroxides (a) and from molecular precursors (In(III) and Sn(IV) chlorides in EtOH) (b) treated at 300 °C in air followed by a treatment at 300 °C in N_2/H_2. 121

Figure 5.7 XRD patterns of mesoporous ITO films assembled from nano-hydroxides (A) and from molecular precursors (In(III) and Sn(IV) chlorides in EtOH) (B) treated at 300 °C in air followed by a treatment at 300 °C in N_2/H_2. 121

Figure 5.8 Mesoporosity and crystallinity of the ITO films assembled from nano-hydroxides: (a) STEM-HAAD image, (b) HR-TEM image, (c) SAED pattern and (d) small angle XRD pattern of mesoporous ITO films after heat treatment at 300 °C in air followed by heating at 300 °C in 5% H_2/N_2. 123

Figure 5.9 Kr sorption isotherms (measured at 77 K) on mesoporous ITO films assembled from nano-hydroxides treated in forming gas (5% H_2/N_2) at different temperatures. 124

Figure 5.10 Specific conductivity of mesoporous ITO films produced from nano-hydroxides, calcined in air at 300 °C and treated in nitrogen or forming gas at 300 °C to 500 °C. 126

Figure 5.11 Cyclic voltammograms of (a) hexacyanoferrate $K_3Fe(CN)_6$ immobilized on the mesoporous ITO electrode, subsequently heated at 300 °C in air and forming gas, respectively (red) and flat ITO film (black and inset) via electrostatic interactions with polycationic electrolyte, and (b) ferrocene carboxylic acid covalently immobilized in the pores of mesoporous ITO (blue) and flat ITO (grey) by amide bonds. The inset shows a cyclic voltammogram of $K_3Fe(CN)_6$ immobilized on the flat ITO film via electrostatic interactions with polycationic electrolyte. Scan rate 200 mV/s. 128

Figure 6.1 Schematic description of the fabrication process by co-assembly of ITO precursors and PMMA latex beads 143

Figure 6.2 Wide angle XRD patterns of as-prepared crystalline ITO nanoparticles and indium tin nanohydroxides 144

Figure 6.3 Top view SEM images of co-assembly fabricated macroporous ITO films with different ITO precursors (a) crystalline ITO nanoparticles (b) indium tin nanohydroxides (c) and (d) molecular precursors indium trichloride and tin tetrachloride. The films were treated at 400 ℃ in air. 145

Figure 6.4 Top view SEM images of macroporous ITO with pore sizes (a) 70 nm and (b) 250 nm. The films were treated at 400 ℃ in air and at 400 ℃ in N_2. 146

Figure 6.5 Wide-angle XRD of macroporous ITO powders with pore size of ca. 70 nm and 250 nm. The cast powders were treated at 400 ℃ in air..147

Figure 6.6 UV-vis transmittance of a commercial ITO substrate (black), and the same substrate after coating with macroporous ITO films with the pore size of 70 nm (red) and 250 nm (blue). Films are after the treatment at 400 ℃ in air and 400 ℃ in N_2...148

Figure 7.1 Schematic representations of the charge diffusion pathways (white arrows) to the current collector (blue) for a flat electrode (left) and 3D nanostructured electrode (right). The red part denotes the bulk heterojunction materials..155

Figure 7.2 Layout of an inverted organic BHJ solar cell (a) and energy levels of materials involved in the device (b). Light is illuminated from the anode ITO side. 157

Figure 7.3 Layout of the inverted organic solar cell with the integration of nanostructured ITO electrodes. 158

Figure 7.4 Influence of the titania electron selection layer on the photovoltaic performance of the inverted organic solar cells with different nanostructured ITO electrodes. Photocurrent–voltage curves of the cells with (left) electrode-ref: commercial flat ITO substrate and (right) electrode C: macroporous ITO layer with the pore size of 250 nm. 159

Figure 7.5 I-V curves of solar cells on electrode-ref. The titania layers were made by using different coating approaches: immersion (blue) and spin-coating (red). TEOT concentration 86 mM. The films were annealed at 300 ^{o}C for 30 min. 160

Figure 7.6 I-V curves of solar cells on electrode-ref. The titania layers were annealed at different temperatures: 300 ℃ (blue) and 450 ℃ (red). TEOT solution concentration 86 mM. The films were spin coated at 3000 rpm for 30 s. 161

Figure 7.7 I-V curves of solar cells on electrode-ref. The titania layers were made from TEOT solutions with different concentrations: 30 mM (blue), 60 mM (red) and 86 mM (green). The layers were spin coated at 3000 rpm for 30 s and annealed at 450 ℃ for 30 min. 161

Figure 7.8 Macroporous ITO electrodes before (a, c) and after (b, d) deposition of the titania layer: macroporous ITO film with pore size 70 nm before (a) and after (b) titania coating, macroporous ITO film with pore size 250 nm before (c) and after (d) titania coating. (e) the wall thickness comparison with (red curve) and without (black curve) TiO_2 coating on the pore size ca. 250 nm macroporous film. (f) High resolution SEM image of TiO_2 coated ITO framework (macroporous ITO film with pore size 250 nm, after TiO_2 layer coating). 163

Figure 7.9 I-V curves of inverted organic BHJ solar cells with nanostructured ITO electrodes. Curve in black denotes the solar cell performance on electrode-ref (flat ITO substrate); Curve in red denotes the solar cell performance on electrode-A (non-templated ITO film); Curve in blue denotes the solar cell performance on electrode-B (macroporous ITO film with pore size 70 nm); Curve in green denotes the solar cell performance on electrode-ref (macroporous ITO film with pore size 250 nm). 164

Contents

ACKNOWLEDGEMENTS III

ABSTRACT V

LIST OF ABBREVIATIONS VIII

TABLE OF FIGURES X

CHAPTER 1 1

INTRODUCTION 1

- 1.1. TRANSPARENT CONDUCTING OXIDES 1
  - 1.1.1. Theoretical background of TCO materials 2
  - 1.1.2. Electrical and optical properties of TCO materials 6
- 1.2. NANOSTRUCTURED TCO FILMS 9
- 1.3. CHAPTER REFERENCES 21

CHAPTER 2 29

CHARACTERIZATION METHODS 29

- 2.1. X-RAY DIFFRACTION (XRD) 29
- 2.2. ELECTRON MICROSCOPY 33
- 2.3. X-RAY PHOTOELECTRON SPECTROSCOPY (XPS) 36
- 2.4. THERMAL ANALYSIS (DSC AND TGA) 38
- 2.5. DYNAMIC LIGHT SCATTERING (DLS) 39
- 2.6. SORPTION 41
- 2.7. CHARACTERIZATION OF ELECTRICAL PROPERTIES 44
  - 2.7.1. Hall measurement with Van der Pauw method 44
  - 2.7.2. Time-domain terahertz spectroscopy 49
- 2.8. ELECTROCHEMICAL CYCLIC VOLTAMMOGRAM 50
- 2.9. FABRICATION AND CHARACTERIZATION OF ORGANIC PHOTOVOLTAICS 53
- 2.10. CHAPTER REFERENCE 55

CHAPTER 3 59

NIOBIUM DOPED TITANIA NANOPARTICLES: SYNTHESIS, ASSEMBLY INTO MESOPOROUS FILMS AND ELECTRICAL CONDUCTIVITY 59

- 3.1. INTRODUCTION 59
- 3.2. RESULTS 62

- 3.2.1. Synthesis of Nb-doped TiO_2 nanoparticles and their assembly into mesoporous films 62
- 3.2.2. Electrical conductivity of Nb-doped TiO_2 nanoparticles 71
- 3.3. DISCUSSION 76
- 3.4. CONCLUSIONS 79
- 3.5. EXPERIMENTAL PART 79
- 3.6. CHAPTER REFERENCES 82

CHAPTER 4 89

TUNING THE CONDUCTION MECHANISM IN NB-DOPED TITANIA NANOPARTICLE NETWORKS 89

- 4.1. INTRODUCTION 89
- 4.2. EXPERIMENTAL RESULTS 92
- 4.3. MODEL OF THE DIELECTRIC FUNCTION 97
- 4.4. DISCUSSION 100
- 4.5. CONCLUSION 106
- 4.6. CHAPTER REFERENCES 107

CHAPTER 5 111

NANO-HYDROXIDES AS VERSATILE PRIMARY UNITS FOR THE ASSEMBLY OF MESOPOROUS INDIUM TIN OXIDE ELECTRODES 111

- 5.1. INTRODUCTION 111
- 5.2. RESULTS AND DISCUSSION 114
  - 5.2.1. Synthesis of indium tin hydroxide nanoparticles 114
  - 5.2.2. Self-assembly of pre-formed nano-hydroxides into mesoporous conducting ITO films… 119
  - 5.2.3. Electrical conductivity and application as electrodes 125
- 5.3. CONCLUSIONS 128
- 5.4. EXPERIMENTAL PART 130
  - 5.4.1. Synthesis of nanoparticles and mesoporous films 130
  - 5.4.2. Characterization of nanoparticles and mesoporous films 132
- 5.5. CHAPTER REFERENCES 135

CHAPTER 6 141

MACROPOROUS ITO FILMS ASSEMBLED FROM INDIUM TIN HYDROXIDE NANOPARTICLES 141

- 6.1. INTRODUCTION 141
- 6.2. RESULTS AND DISCUSSION 142
- 6.3. SUMMARY 149
- 6.4. EXPERIMENTAL PART 149

6.5. CHAPTER REFERENCES....151

CHAPTER 7 ....**153**

BULK HETEROJUNTION SOLAR CELLS WITH NANOSTRUCTURED ITO ELECTRODES....**153**

7.1. INTRODUCTION....153
7.2. RESULTS AND DISCUSSION....156
7.2.1. Optimization of the titania electron selection layer 158
7.2.2. Solar cells with the integration of nanostructured ITO electrodes....162
7.3. SUMMARY AND OUTLOOK 167
7.4. EXPERIMENTAL PART 167
7.5. CHAPTER REFERENCES 169

CHAPTER 8 ....**173**

CONCLUSIONS AND OUTLOOK **173**

APPENDIX I....**177**

APPENDIX II **181**

PUBLICATIONS AND PRESENTATIONS....**183**

CURRICULUM VITAE....**185**

Chapter 1

Introduction

1.1. Transparent conducting oxides

Transparent conducting oxides (TCOs) are materials combining high electrical conductivity (10^3~10^4 S/cm) and high optical transparency (above 80%) in the visible spectrum [1-4]. They are different from the well-known conductors such as metals, semimetals or carbon materials, or transparent materials such as oxide glasses. The metals are excellent electric conductors due to a large concentration of delocalized mobile electrons, but they strongly absorb visible light and hence are not transparent. On the other hand, the oxide glasses are highly transparent owing to their large band-gap energy (over 3 eV), but the absence of enough free charge carriers generally determines their low electrical conduction behavior. The combination of the seemingly contradictory properties, namely high electrical conductivity and the high optical transparency, is however featured by the TCO materials [5-7].

The first TCO was reported about one hundred years ago, when Badeker noticed that the oxidation of metallic Cd makes the material optically transparent while remaining highly conducting [3]. Half a century later, the materials combining both optical transparency and high electrical conductivity have expanded to a lot of systems, such as the non-stoichiometric and doped oxides of indium, tin and zinc, as well as related binary, ternary and even quaternary systems [1, 8-10] (Figure 1.1). On the other side, the growing interest in TCO materials has also stimulated the development of various approaches to their deposition on planar substrates [3].

Nowadays, the TCO films can be deposited by a series of different techniques such as magnetron sputtering, ion beam sputtering, reactive ion plating, pulsed laser deposition, chemical vapor deposition, spray pyrolysis and wet-chemical solution approaches.

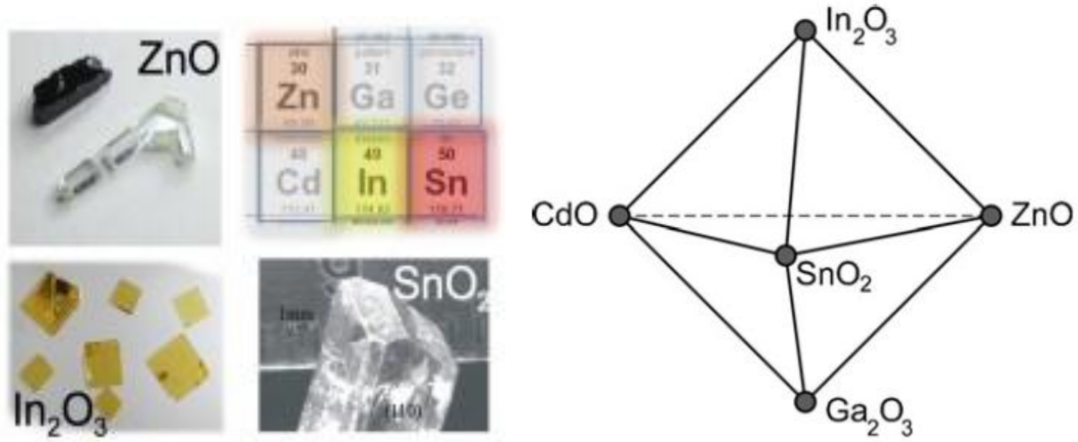

Figure 1.1 Commonly used transparent conducting oxide systems [11] (left) and their multiple combinations [4] (right)

TCO films have a wide variety of applications [4-5, 12-14]. Highly conducting TCOs are used as front electrodes for electronic and optoelectronic devices such as flat panel displays, touch panel controls, solar cells or organic light emitting diodes (OLEDs). For these devices, the requirements of electrical contact and optical access can be fulfilled by TCO films. Besides, due to the TCOs' ability to reflect infrared radiation, they can also be used as energy-conserving windows in aircrafts, automobiles and buildings.

1.1.1. Theoretical background of TCO materials

Theoretical modeling and empirical analysis suggest that the special combination of high electrical conductivity and optical transparency can be realized by selecting a wide band-gap metal oxide which could be rendered degenerate (metal-like electronic behavior) through suitable incorporation of native donors or substitutional dopants into the host lattice [3].

For the n-type doped metal oxides [2, 15], native donor- or extrinsic dopant-induced charges (electrons) form a level just below the bottom of the conduction band which is empty in the intrinsic semiconductors. With the increase of doping density, these impurity levels eventually merge and form a continuous band, as is illustrated in Figure 1.2 (middle). Beyond a certain critical concentration n_c (called Mott carrier density), the donor band overlaps with the conduction band and electrons behave like free charge carriers. The oxides are degenerate in nature. For p-type doped metal oxides, impurity dopants result in the formation of acceptor levels located above the top of the valence band. As the doping density increases, a continuous acceptor band forms and overlaps with the valence band at a critical concentration n_c, resulting in the degeneration of the oxides.

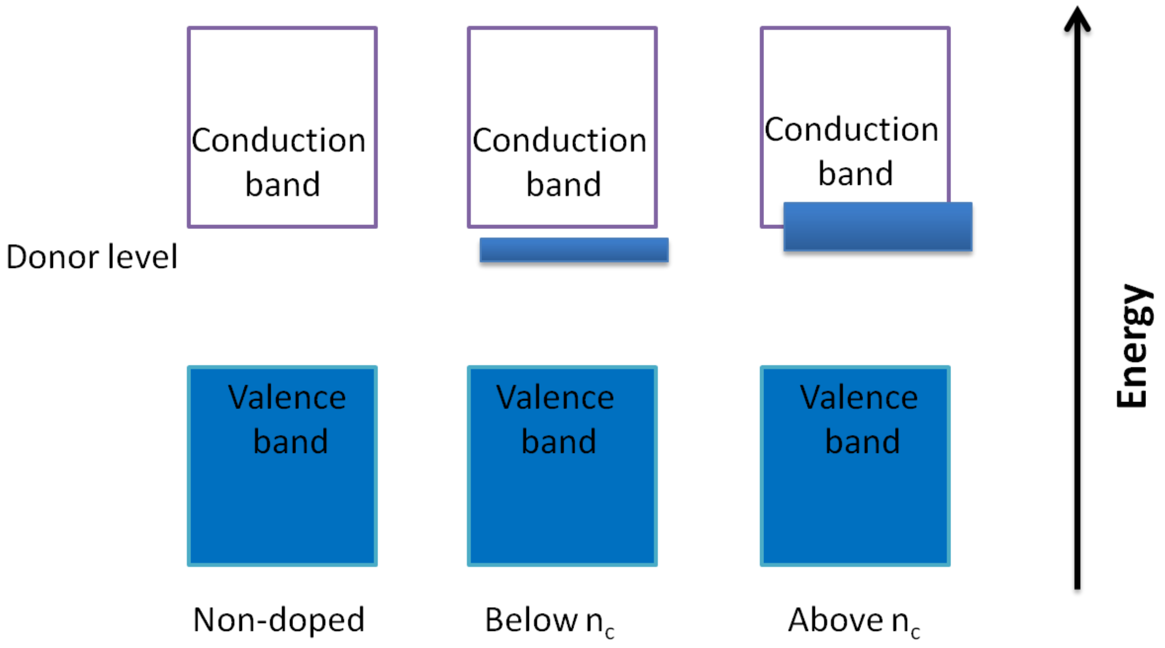
Conduction band
Conduction band
Conduction band
Donor level
Energy
Valence band
Valence band
Valence band
Non-doped
Below n_c
Above n_c

Figure 1.2 Schematic descriptions of the n-type doping: with the increase of doping density; n_c is the critical concentration (Mott carrier density).

Figure 1.2 presents a simplified illustration of the doping process, without taking into account the possible change of the band-gap. Actually, above the critical concentration n_c, the mutual exchange and Coulombic interactions between the added free electrons in the conduction band and the electron-impurity scattering lead to an upward shift of valence band and downward shift of conduction band, hence, the band gap is reduced [16]. However, the fundamental optical transition in degenerated oxides requires higher energies, since the highest occupied level becomes higher due to the added free electrons which will result in the larger optical band gap [17] (so called Burstein-Moss effect). Figure 1.3 depicts the band gap change based on these two effects, where E_0 is the intrinsic band-gap, E_1 is the varied band-gap due to electron-impurity scattering, E_2 is the varied band-gap due to Burstein-Moss effect. The actual band-gap change includes the above two effects.

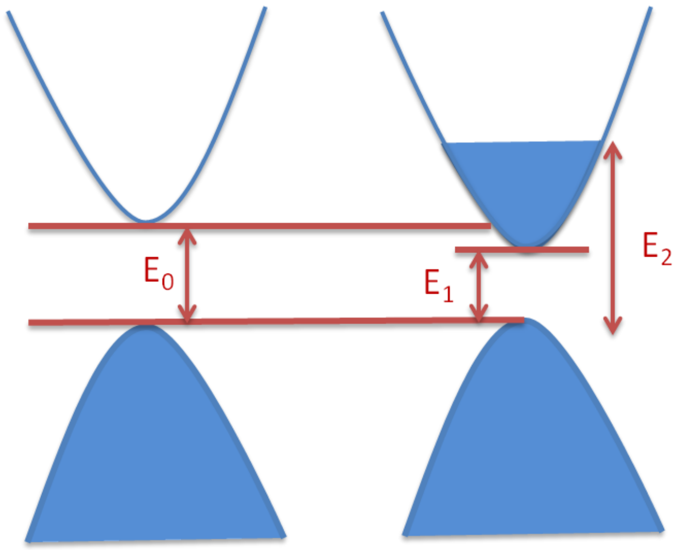

Figure 1.3 Band-gap changes based on electron-impurity scattering and Burstein-Moss effect. E_0 is the intrinsic band-gap, E_1 is the varied band-gap due to electron-impurity scattering, E_2 is the varied band-gap due to Burstein-Moss effect. After Gupta [18].

Besides the degeneracy, a second feature of TCO materials is their free-electron-like conduction band minimum, formed from the s states of metal ions [10]. This is a condition for small effective mass of the free charge carriers, and thus high charge mobility. This feature is shared by practically all the commonly used TCO systems such as indium oxide, tin oxide, zinc oxide, and it also gives the direction for the development of new TCO materials.

Empirically, there are several general requirements for the doped metal oxides to obtain a combination of high electrical conductivity and high optical transparency.

(1) Band-gap energy of the metal oxide

The fundamental requirement for the band-gap energy of a metal oxide concerns the photon absorption-induced transmittance loss in the visible spectrum. Generally, a small band gap is advantageous for the electron excitation from valence band to conduction band, resulting in high conductivity. However, this decreases the optical transparency, since photons with energy corresponding to the visible light spectrum (wavelength from 350 nm to 750 nm) can be absorbed. When the band gap energy is above 3 eV, the photons lying in the visible range are not absorbed and thus the optical transparency remains high.

(2) Properties of host metal oxide

Realization of high conductivity in wide band-gap metal oxide is largely dependent on the electron affinity or work function of the materials [3]. For the n-type doped metal oxides, high electron affinity of the host metal oxide is suggested to be beneficial to achieve high electron concentration and degeneracy. For the p-type metal oxides, this rule suggests that a low work function of the host metal oxide is required. However, low work function is not easy to be satisfied for most of the wide band-gap metal oxides, owning to the nature of the metal-oxygen bond. This might be one of the reasons that not so many p-type TCO materials have been reported so far (except the Cu^+ containing oxides $CuAlO_2$, $CuGaO_2$). Metal chalcogenides have somewhat lower work function than metal oxides, making them better candidates for the p-type TCO materials.

(3) Choice of the dopants

In order to accomplish efficient doping, the lattice stability of the host metal oxide should be considered [3, 10]. It is generally affected by the disparities between dopant atoms and the corresponding host atoms. According to the Hume-Rothery rule, the atomic radii differences between the dopant and host atoms/ions should be less than 15%. Otherwise, the distortion of the host metal oxide lattice will result in generating unfavorable ‘killer defects’, which will compensate the extra electrons or holes induced by the dopants. For example, for the n-type doped metal oxides, cation vacancies will start to form when the lattice stability is decreased. For the p-type doped metal oxides, the presence of anion vacancies will act as a response towards the lattice distortion, both of which will pin the free charge carriers and thus weaken the doping effect. Besides, dopants should be able to form shallow donor levels as a result of the doping process.

1.1.2. Electrical and optical properties of TCO materials

There are two practical parameters that are generally accepted to determine the quality of TCO materials, namely electrical conductivity and the average visible transmittance. These two parameters are strongly interrelated with each other [1].

Electrical conductivity is a product of charge carrier density and charge transport mobility in the presence of elemental charge:

$$\sigma = n \cdot e \cdot \mu \qquad \text{Equation 1.1}$$

Where: σ denotes the dc conductivity (S/cm), n is the charge carrier density, μ is the charge mobility ($m^2V^{-1}s^{-1}$), e is the elementary charge (1.6×10^{-19} C).

In the doped wide band-gap metal oxides, n and μ cannot be increased simultaneously. High charge carrier concentration can be achieved from intrinsic or extrinsic doping, however, the presence of native donors and impurity ions induces scattering [1] (electron-electron scattering, electron-impurity scattering, doping modified lattice scattering) for the movement of charge carriers, hence, the charge mobility decreases. At a certain doping concentration, the conductivity reaches a limit and does not increase anymore. On the other hand, the continually growing doping concentration decreases the optical transmission and makes the optical window narrower, according to the Drude model. For example, for indium tin oxide, electron concentration should be less than 2.6×10^{21} cm^{-3} in order to achieve efficient transmission in the whole visible range. Therefore, we can see that the charge carrier concentration and transport mobility are the fundamental factors influencing the properties of TCO materials.

In the next part, we will outline two specific TCO systems, namely tin doped indium oxide (ITO) and niobium doped titanium oxide, concerning doping involved charge carrier generation and electron mobility.

Tin doped indium oxide (ITO)

Tin doped indium oxide, which is usually abbreviated as ITO (indium tin oxide), is one of the most broadly used TCOs since the 1960s. The high quality ITO films possess a conductivity of 10^4 to 10^5 S/cm and high optical transmittance of over 85% in the visible range [6, 19].

Indium oxide has the cubic bixbyite structure, where the In ions are six-coordinated by oxygen. It has a single free-electron-like conduction minimum, formed from In s states, which represents low scattering probability for the mobile charges. ITO exhibits higher electrical conductivity than pure In_2O_3 due to the substitution of In atom (3 valence electrons) with dopant Sn atoms (4 valence electrons). This process generates one extra electron, which contributes to the formation of a shallow donor level beneath the conduction band. According to Gupta‘s calculation, the critical charge concentration (Mott carrier density) to realize degeneracy is 2.3 $\times 10^{-19}$ cm^{-3} [18].

The small atomic radius difference between In (atomic radius 1.55 Å) and Sn (atomic radius 1.41 Å) allows for the incorporation of high amounts of Sn atoms into the lattice of indium oxide without significant distortion of its crystalline lattice. The doping with Sn greatly increases the electrical conductivity of indium oxide. The change in conductivity is however not linearly dependent on the content of Sn atoms [20], which can be explained by the decrease in electron mobility due to the enhanced scattering effect from impurity ions. The specific microstructure of ITO films also strongly affects the electrical properties. Dense films with low porosity can reach a high conductivity of 10^5 S/cm, while the conductivity of the films fabricated by the sol-gel approach [20] or from ITO nanoparticle suspensions [21-22] (high porosity) is much lower, about 10^3 and 10^2 S/cm, respectively. Besides, crystallinity also affects the charge mobility, since the structural disorder will localize the mobile electrons.

Niobium doped titanium oxide (NTO)

Recently, the group of Furubayashi reported for the first time the high electrical conductivity (10^4 S/cm) and high optical transparency (97% for 40 nm thickness) for niobium doped anatase titania (NTO). The films were generally grown epicaxially by pulsed laser deposition (PLD), magnetron sputtering and rf magnetron sputtering [23-28].

Undoped anatase titania has a band gap energy of 3.2 eV and has been intensively studied regarding its photocatalytic properties [29-31], but the titania had not been considered as a transparent conductor. Furubayashi’s work has demonstrated that the controlled doping with Nb is able to drastically improve the electrical conductivity of titania via substitution of Ti atoms (4 valence electrons) with Nb (5 valence electrons). Studies show that, different from ITO and other TCO systems which possess a free-electron-like conduction band minimum formed from metal atom's s states, the bottom of NTO's conduction band consists of Ti 3d_{xy} and Nb 4d_{xy} orbitals [32]. The minimum of its conduction band shows more dispersion than the s states-based parabolic band structure, which might be the reason that the NTO systems show a lower electron mobility than other TCO systems.

Due to the small difference in the atomic radii between Ti (2.0 Å) and Nb (2.08 Å), the incorporation level of Nb into the anatase lattice can reach up to 20% by chemical sol-gel synthesis [33] and up to 40% by physical deposition methods [25]. The lattice constants linearly increase with the Nb dopant concentration, as expected from Vegard's law. The electron concentration increases with the increase in the Nb dopant concentration. However, the mobility starts to decrease after a certain doping level leading to the decrease in conductivity. The optimal conductivity for the NTO system prepared by pulsed laser deposition was obtained for a Nb concentration of 3%.

1.2. Nanostructured TCO films

A majority of the known TCO materials is prepared in the form of planar thin films, which is a prevailing morphology in the existing applications. The fabrication of nanostructured TCO materials is in comparison much less investigated, although the nanostructuring and elaboration of novel TCO morphologies can substantially extend their application potential. The nanostructures have the capacity to dramatically increase their interface area and provide accessible inner space. Besides, the nanostructure framework composed of a TCO phase keeps its high conduction and light transmittance in the visible range. The resulting structural features together with a functional interconnected framework can substantially increase the applicability of TCO materials, paving ways for new efficient devices. Therefore, in the past few years, the development of various synthetic approaches towards the fabrication of nanostructured TCO films has aroused a lot of interest in the academic and industrial communities.

Nanostructured TCO layers are very attractive as conducting hosts for accommodation of redox species. They provide a very large conducting interface enabling a direct heterogeneous electron transfer to each incorporated molecule, and a high surface area leading to a greatly enhanced loading with reactive species. Additionally, the controlled porosity enables one to tune the chemical surrounding of incorporated molecules by a chemical modification of the pore interior. Another application of porous TCO layers that was pursued by several authors is their use as nanostructured electrodes in photovoltaic devices aimed at the shortening of the charge transport distance and reduction of recombination rates between electrons and holes [34-38]. The 3D porous TCO films can also be used for bioelectronics, sensors, energy storage devices and so on, leading to more efficient device performance.

The growing interest in the nanostructured TCOs has activated the research in this area in the last few years, and different TCO morphologies obtained by different approaches were reported by several groups. The known morphologies involve nanoleaves which were prepared by a one-step carbon-thermal evaporation method [39], nanobranches prepared by electron beam evaporation [40], hierarchical structures consisting of nanowires and nanorods prepared by thermal vapor evaporation [41], columnar channel-like nanostructures made by electrochemical anodization processes [42], vertical nanopost films obtained by vacuum-based glancing-angle deposition [43] and nanowires prepared by laser ablation [34]. Some of the examples of those morphologies are presented in Figure 1.4.

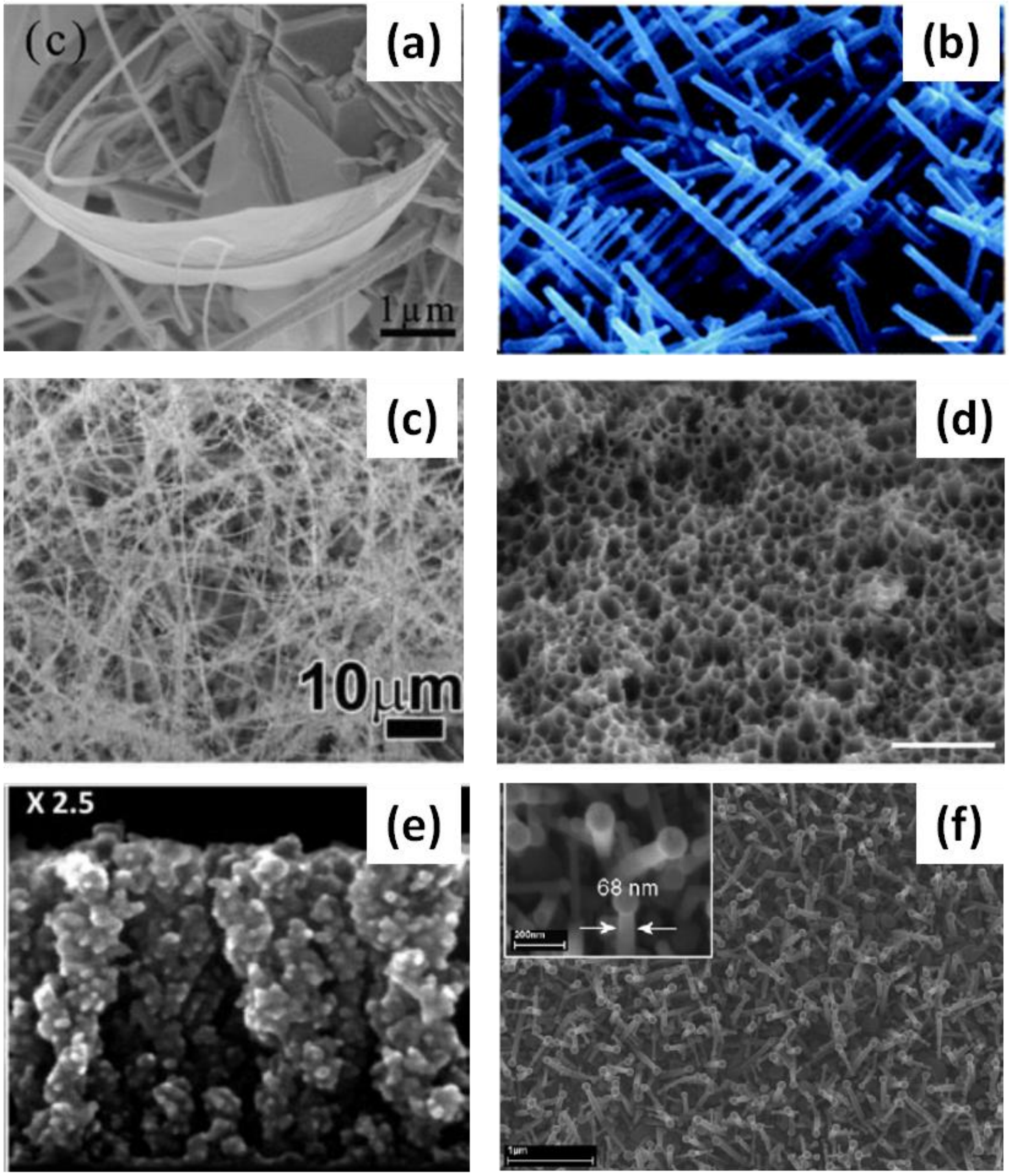

Figure 1.4 Some examples of the nanostructured TCO morphologies: (a) nanoleaves of Ga-doped In_2O_3 obtained by carbon-thermal evaporation [39]; (b) nanobranches of ITO prepared by electron beam evaporation [40]; (c) hierarchical nanostructure of In-doped ZnO prepared by thermal vapor evaporation [41]; (d) columnar channel-like SnO_2 obtained by electrochemical anodization [42]; (e) vertical nanopost ITO prepared by vacuum-based glancing-angle deposition [43]; (f) ITO nanowires prepared by laser ablation [34].

Another important nanostructure of TCO materials is the 3D porous morphology. In addition to the large interface area and conductive framework, this nanostructure provides accessible pores with defined pore size and open porosity, which could be used to host functional species for different applications. Some of the porous TCO materials have been already developed; the fabrication of such morphologies is generally performed by two basic strategies.

The first method is based on an assembly of crystalline TCO nanoparticles. For fabrication of the films, one can either cast pastes prepared from the nanoparticles (for example using doctor blading), or coat the films using solution deposition techniques (e.g. dip- or spin-coating) with the nanoparticle suspensions in different solvents. The fabrication of such films is rather simple. However, the porosity of the films obtained in such way is mostly textural porosity resulting from the voids between the nanoparticles and as a result, the pores are not periodically organized and the pore size distribution is not homogeneous (Figure 1.5). Although the nanoparticles feature a high crystallinity, the prepared films still require a further higher temperature annealing (at above 500 ^{o}C) to sinter the nanoparticles and to improve the mechanical stability and electrical conductivity of the films.

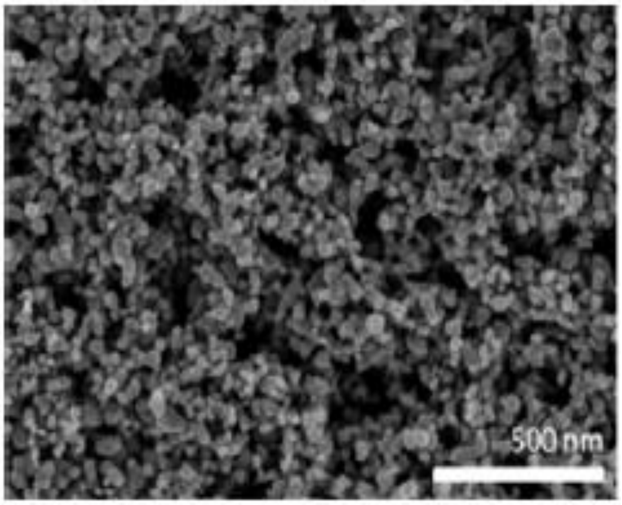

Figure 1.5 Example of the porous ITO morphology obtained by spin coating of an ITO nanoparticle suspension [44].

The second established approach is a so called templated sol-gel synthesis. It involves the self-assembly of inorganic molecular precursors and some structure-determining units called templates. Since the geometry of the template (size, shape, etc.) defines the final structure of the inorganic framework, a good control over materials' pore size and pore arrangement could be reached by selecting different templates [45-49].

Micelle-forming amphiphilic organic molecules, such as ionic surfactants and block co-polymers, are often employed as the structure directing agents (SDAs) in the evaporation-induced self-assembly process (EISA) to fabricate 3D porous films. By a variation of the size of the surfactant and thus the size of the micelles, pore sizes ranging from a few nanometers to about 50 nanometers can be obtained. Figure 1.6 illustrates the assembly process and formation of a mesoporous framework [45]. In a solution mixture of inorganic molecular precursors and SDA molecules, the hydrolyzed inorganic species strongly interact with the hydrophilic parts of charged surfactants or block-co-polymers; evaporation of the volatile solvent concentrates the inorganic precursors and surfactant molecules, driving the mesophase formation through their co-assembly; the following aging and thermal treatment will condense the framework and remove the organic templates, thus, porous films with accessible pores are generated.

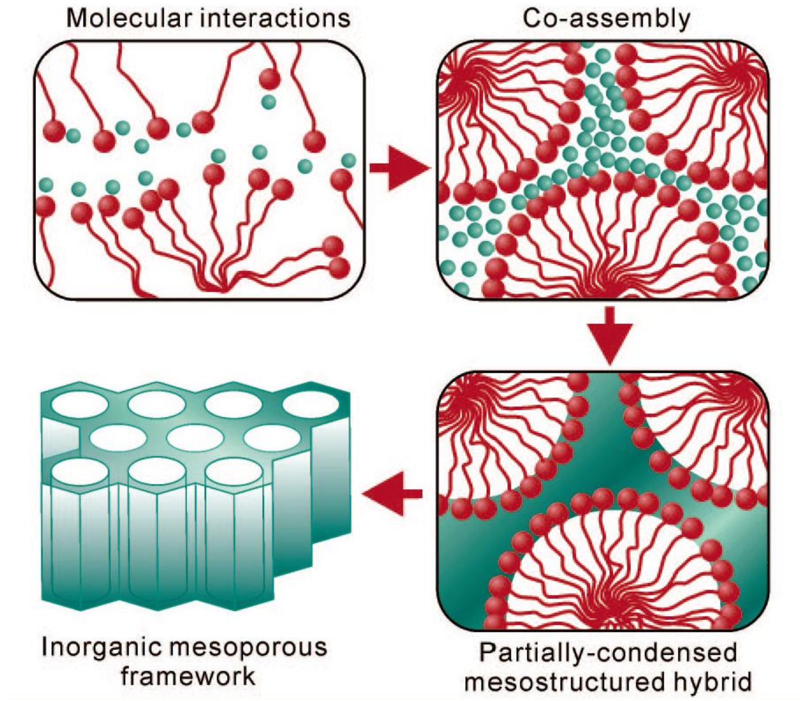
Molecular interactions
Co-assembly
Inorganic mesoporous framework
Partially-condensed mesostructured hybrid

Figure 1.6 Formation of mesostructured materials through the co-assembly of inorganic precursors and surfactant molecules [45].

The EISA approach has been utilized to synthesize a large variety of mesoporous metal oxide films (such as TiO_2, Nb_2O_5, ZrO_2 or $BaTiO_3$ [50-52], just to name a few) with different structure and periodicity of mesoporous morphology (e.g. cubic, hexagonal, lamellar and wormlike mesophases) and different crystallinity of the mesoporous scaffold. The application of this approach to the fabrication of mesoporous TCO films is however aggravated by the rather poor ability of TCO precursor compounds to form stable sols and the hardly controllable crystal growth in the final structure, causing the mesostructure to partially or completely collapse. These hurdles were overcame only recently by the groups of Smarsly, Ozin, Thomas and our group, and several TCO systems have been fabricated with a defined 3D porous morphology.

Several groups obtained crystalline mesoporous films of different TCOs by the EISA approach from molecular TCO precursors and amphiphilic block-copolymers acting as templates. The self-assembly of these precursor species leads to the formation of mesoscopic composite materials with an amorphous TCO scaffold, which usually needs to be heated at elevated temperature for crystallization. A possible mesostructure collapse at this step due to the uncontrollable crystal growth, which is the major problem in the fabrication of mesoporous crystalline films by the EISA process, was addressed by the use of special block-co-polymers acting as templates. The used polymers poly(ethylene-co-butylene)-b-poly(ethylene oxide) (KLE) and poly(isobutylene)-b-poly(ethyleneoxide) (PIB-PEO) possess a high thermal decomposition temperature, high hydrophilic-hydrophobic contrast and large micellar size. Using these templates, 3D mesoporous crystalline TCO films of tin doped indium oxide (ITO) [53-54], antimony doped tin oxide (ATO) [55], Nb doped tin oxide and Ta doped tin oxide [55] have been prepared. These mesostructured TCO films feature high specific interface area, periodically organized pores and highly (electrically) conducting frameworks. Additionally, the pore size and the wall thickness of the obtained mesoporous TCO films can be adjusted by selecting amphiphilic organic molecules with different hydrophobic components (Figure 1.7).

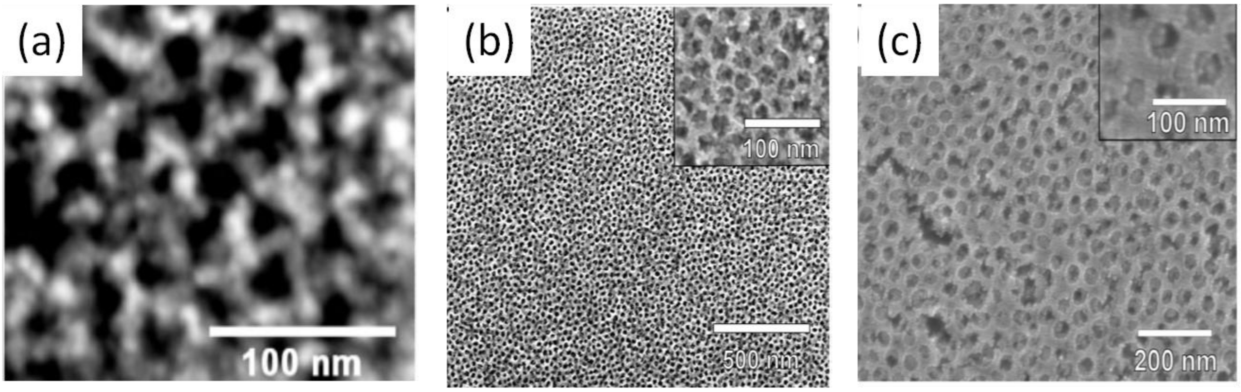

Figure 1.7 Examples of the mesoporous ITO films prepared by the EISA approach from molecular precursors and different amphiphilic block co-polymer templates: (a) KLE, pore size and wall thickness of the resulting mesostructure about 16 nm × 8 nm and 7-9 nm, respectively [53]; (b) PIB-PEO-3000, pore size and wall thickness of the resulting mesostructure about 20-25 nm and 12-18 nm, respectively [54]; (c) PIB-PEO-20000, pore size and wall thickness of the resulting mesostructure about 35-45 nm and 8-10 nm, respectively [54].

Another strategy to avoid the collapse of the amorphous mesoporous TCO scaffold during the thermal treatment and crystallization involves a prolonged aging of the template-containing mesoscopic films at elevated temperatures (60 – 150 ℃) and controlled humidity, so called delayed humidity treatment (DHT). Using this approach, periodically organized mesoporous crystalline tin oxide films and antimony doped tin oxide (ATO) films have been reported by Pan [56], Koehn [57-58] and Ozin [59]. This method enables the use of commercially available block copolymers of the Pluronic family as the templates, but it is rather time consuming.

Very recently, Thomas et al. developed a novel approach to prepare mesoporous tin-rich indium oxide films from a newly developed molecular precursor, indium tin tris-tert-butoxide (Figure 1.8) [60]. This molecular precursor is very air sensitive and requires careful operation; however, its versatile assembling ability enabled the fabrication of mesoporous tin-rich indium oxide films using different block copolymers such as KLE, Pluronic F127 and Brij 700. The resulting pore size varies from 12 nm (KLE), 6.5 nm (Pluronic F127), to 4.8 nm (Brij 700). In contrast to the known TCO materials, the formed tin-rich indium oxide framework shows the highest conductivity in the amorphous state, the conductivity decreasing upon crystallization.

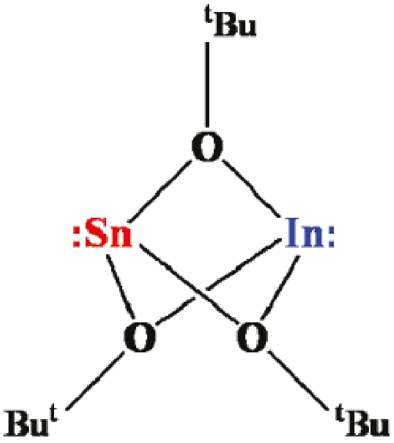

Figure 1.8 Molecular precursor of indium tin tris-tert-butoxide [60].

We have developed an alternative approach towards fabrication of TCO films with 3D nanostructured morphologies and crystalline walls based on preformed crystalline TCO nanoparticles as the inorganic building blocks. Using the templated assembly of nanoparticles, films of different TCO systems such as antimony doped tin oxide [61], niobium doped titanium oxide (chapter 3 of this thesis) and ITO (chapters 5 of this thesis) with defined porosity, large interface area and conducting crystalline TCO framework have been obtained. This approach enables us to use commercially available block copolymers and available inorganic precursors for the fabrication of periodic porous TCO films.

The use of micelles as the templates enables the fabrication of mesoporous materials with a maximum pore size of about 50 nm. When larger pore sizes are required, some other type of templating agents has to be used. Nanoparticles of different materials such as polymer nanoparticle colloids (latex) of polystyrene (PS) or poly (methyl methacrylate) (PMMA) beads or silica spheres are often employed as the suitable templates. This method is known as colloidal crystal templating (CCT) [48, 62-66]. It involves self-assembly (typically cubic close packing) of spherical particles with the formation of periodic opal structures (Figure 1.9). The voids in the opal templates are then filled with the precursor for the required porous phase using different strategies, the most common being infiltration and electrodeposition. After condensation of the precursor and the removal of the opal template, a porous negative replica (inverse opal structure) composed of the material of interest is formed (Figure 1.9). Typically, a uniform pore size between ca. 50 nm and ca. 1000 nm can be achieved through this method.

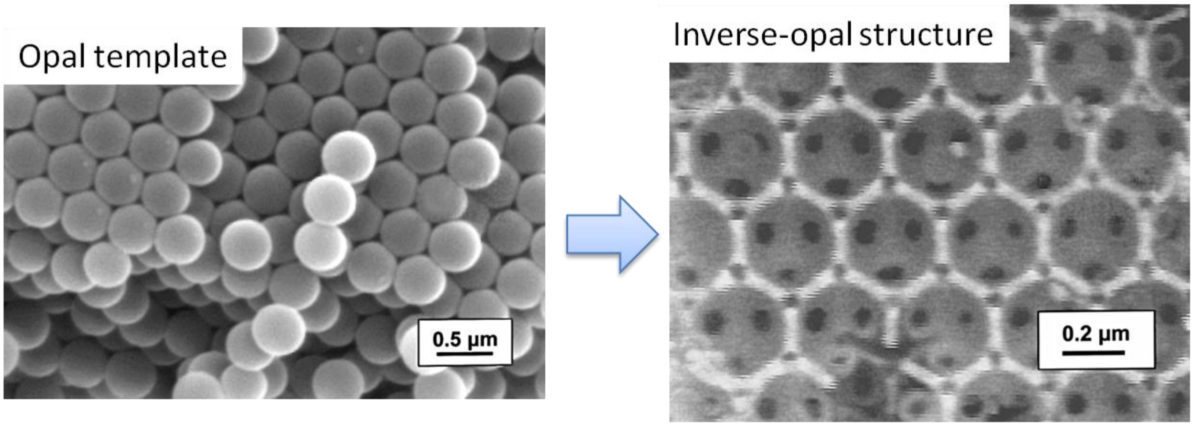

Figure 1.9 SEM images of preformed opal template and inverse-opal structure [48].

Using the CCT approach, two different macroporous TCO systems have been recently prepared, namely antimony doped tin oxide (ATO) [36] and fluorine doped tin oxide (FTO) [37].

Although the infiltration of opal templates is by far the most commonly used strategy for the fabrication of periodic macroporous materials, the fabrication of large-area crack-free macroporous films by this way is far from straightforward. Especially, the second step of liquid infiltration is rather critical in achieving open accessible macropores (this is discussed in more detail in chapter 6 of this thesis). An alternative procedure which has been introduced only recently by Hatton et al. involves co-assembly of colloidal nanoparticles and precursor species for the desired material [67] (Figure 1.10 right). This approach avoids the critical step of liquid infiltration, has fewer fabrication steps and enables the growth of crack-free ordered macroporous films. We have used this concept to fabricate macroporous ITO films using preformed indium tin nanohydroxides as the inorganic precursors (chapter 6 of this thesis).

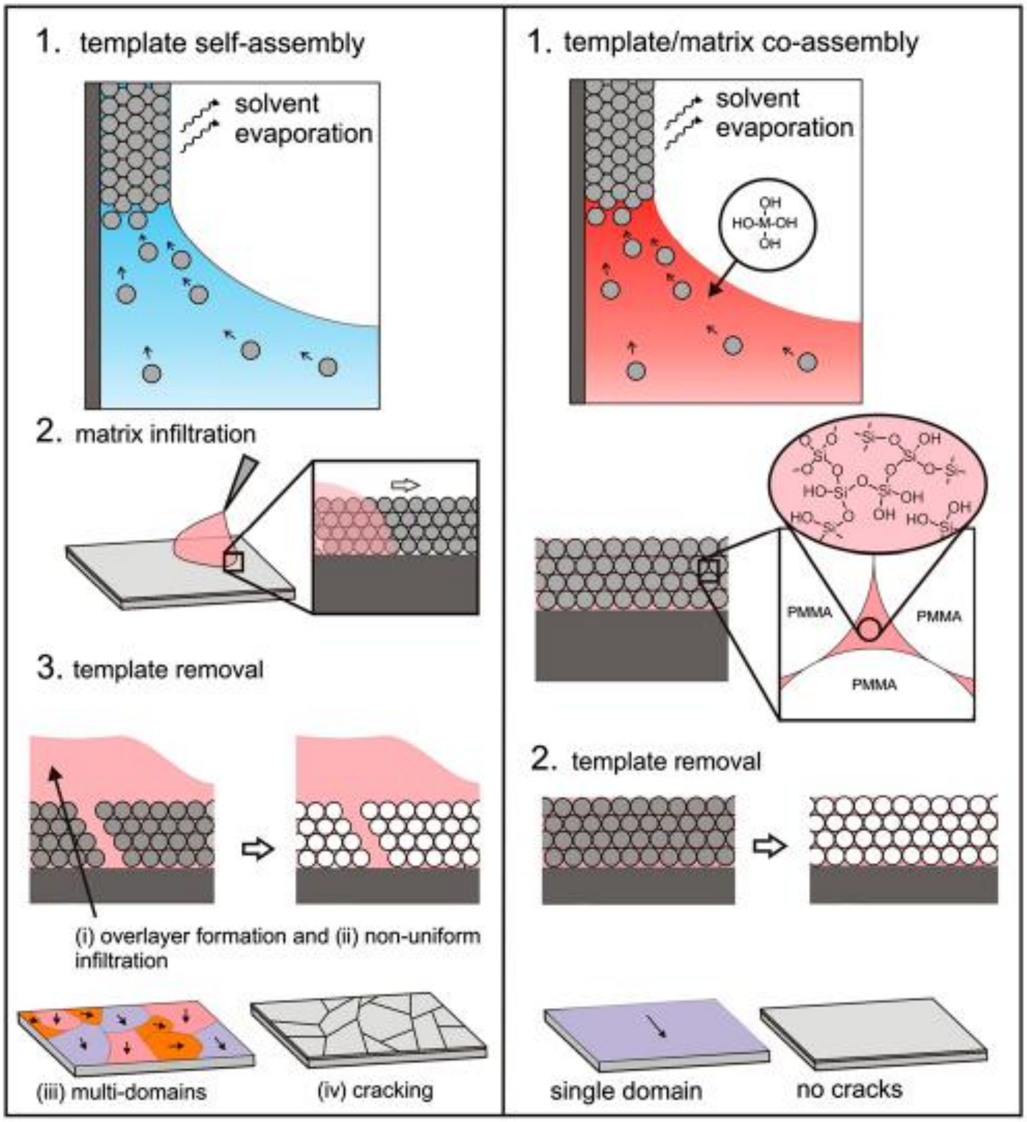
1. template self-assembly
solvent evaporation
2. matrix infiltration
3. template removal
(i) overlayer formation and (ii) non-uniform infiltration
(iii) multi-domains
(iv) cracking
1. template/matrix co-assembly
solvent evaporation
OH
HO-M-OH
OH
HO-Si
OH
PMMA
PMMA
PMMA
2. template removal
single domain
no cracks

Figure 1.10 Two basic approaches towards the fabrication of periodic macroporous films using colloidal crystal templating: infiltration (left) and co-assembly (right) [67].

1.3. Chapter references

1. Chopra, K.L., S. Major, and D.K. Pandya, Transparent conductors-a status review. Thin Solid Films, 1983. **102**(1): p. 1-46.

2. Edwards, P.P., et al., Basic materials physics of transparent conducting oxides. Dalton Transactions, 2004(19): p. 2995-3002.

3. Exarhos, G.J. and X.-D. Zhou, Discovery-based design of transparent conducting oxide films. Thin Solid Films, 2007. **515**(18): p. 7025-7052.

4. Ginley, D.S. and J.D. Perkins, Handbook of Transparent Conductors. 2010. Chapter 1: Transparent conductors. Springer science, New York.

5. Ginley, D.S. and C. Bright, Transparent conducting oxides. Mrs Bulletin, 2000. **25**(8): p. 15-18.

6. Granqvist, C.G. and A. Hultaker, Transparent and conducting ITO films: new developments and applications. Thin Solid Films, 2002. **411**(1): p. 1-5.

7. Gordon, R.G., Criteria for choosing transparent conductors. Mrs Bulletin, 2000. **25**(8): p. 52-57.

8. Minami, T., New n-type transparent conducting oxides. Mrs Bulletin, 2000. **25**(8): p. 38-44.

9. Beyer, W., J. Huepkes, and H. Stiebig, Transparent conducting oxide films for thin film silicon photovoltaics. Thin Solid Films, 2007. **516**(2-4): p. 147-154.

10. Robertson,J. and B. Falabretti, Handbook of Transparent Conductors, 2010. Chapter 2: Electronic structure of transparent conducting oxides. Springer science, New York.

11. http://www.iap.tuwien.ac.at/www/surface/research/transparent_conducting_oxides.

12. Lewis, B.G. and D.C. Paine, Applications and processing of transparent conducting oxides. Mrs Bulletin, 2000. **25**(8): p. 22-27.

13. http://nanomarkets.net/articles/article/thoughts_on_transparent_electronics/P4.

14. Klein, A., et al., Transparent Conducting Oxides for Photovoltaics: Manipulation of Fermi Level, Work Function and Energy Band Alignment. Materials, 2010. **3**(11): p. 4892-4914.

15. Medvedeva, J.E. and A.J. Freeman, Combining high conductivity with complete optical transparency: A band structure approach. Europhysics Letters, 2005. **69**(4): p. 583-587.

16. Walsh, A., J.L.F. Da Silva, and S.-H. Wei, Origins of band-gap renormalization in degenerately doped semiconductors. Physical Review B, 2008. **78**(7).

17. Burstein, E., Anomalous Optical Absorption Limit in InSb. Physical Review, 1954. **93**(3): p. 632-633.

18. Gupta, L., A. Mansingh, and P.K. Srivastava, Band-gap narrowing and the band-structure of tin-doped indium oxide-films. Thin Solid Films, 1989. **176**(1): p. 33-44.

19. Adurodija, F.O., et al., Effect of Sn doping on the electronic transport mechanism of indium-tin-oxide films grown by pulsed laser deposition coupled with substrate irradiation. Journal of Applied Physics, 2000. **88**(7): p. 4175-4180.

20. Alam, M.J. and D.C. Cameron, Optical and electrical properties of transparent conductive ITO thin films deposited by sol-gel process. Thin Solid Films, 2000. **377**: p. 455-459.

21. Al-Dahoudi, N. and M.A. Aegerter, Comparative study of transparent conductive In2O3 : Sn (ITO) coatings made using a sol and a nanoparticle suspension. Thin Solid Films, 2006. **502**(1-2): p. 193-197.

22. Ederth, J., et al., Thin porous indium tin oxide nanoparticle films: effects of annealing in vacuum and air. Applied Physics a-Materials Science & Processing, 2005. **81**(7): p. 1363-1368.

23. Furubayashi, Y., et al., A transparent metal: Nb-doped anatase TiO_2. Applied Physics Letters, 2005. **86**(25).

24. Furubayashi, Y., T. Hitosugi, and T. Hasegawa, Response to "Comment on 'A transparent metal: Nb-doped anatase TiO_2' Appl. Phys. Lett. 86, 252101 (2005) ". Applied Physics Letters, 2006. **88**(22).

25. Furubayashi, Y., et al., Transport properties of d-electron-based transparent conducting oxide: Anatase $Ti_{1-x}Nb_xO_2$. Journal of Applied Physics, 2007. **101**(9).

26. Hosono, H., Recent progress in transparent oxide semiconductors: Materials and device application. Thin Solid Films, 2007. **515**(15): p. 6000-6014.

27. Zhang, S.X., et al., Niobium doped TiO_2: Intrinsic transparent metallic anatase versus highly resistive rutile phase. Journal of Applied Physics, 2007. **102**(1).

28. Liu, X.D., et al., Electronic structure and optical properties of Nb-doped anatase TiO_2. Applied Physics Letters, 2008. **92**(25).

29. Mattsson, A., et al., Adsorption and solar light decomposition of acetone on anatase TiO_2 and niobium doped TiO_2 thin films. Journal of Physical Chemistry B, 2006. **110**(3): p. 1210-1220.

30. Emeline, A.V., et al., Photoelectrochemical behavior of Nb-doped TiO_2 electrodes. Journal of Physical Chemistry B, 2005. **109**(51): p. 24441-24444.

31. Hirano, M. and K. Matsushima, Photoactive and adsorptive niobium-doped anatase (TiO_2) nanoparticles: Influence of hydrothermal conditions on their morphology, structure, and properties. Journal of the American Ceramic Society, 2006. **89**(1): p. 110-117.

32. Hitosugi, T., et al., Electronic Band Structure of Transparent Conductor: Nb-Doped Anatase TiO_2. Applied Physics Express, 2008. **1**(11).

33. Ruiz, A.M., et al., Insights into the structural and chemical modifications of Nb additive on TiO_2 nanoparticles. Chemistry of Materials, 2004. **16**(5): p. 862-871.

34. Joanni, E., et al., Dye-sensitized solar cell architecture based on indium-tin oxide nanowires coated with titanium dioxide. Scripta Materialia, 2007. **57**(3): p. 277-280.

35. Martinson, A.B.F., et al., Radial electron collection in dye-sensitized solar cells. Nano Letters, 2008. **8**(9): p. 2862-2866.

36. Arsenault, E., N. Soheilnia, and G.A. Ozin, Periodic Macroporous Nanocrystalline Antimony-Doped Tin Oxide Electrode. Acs Nano, 2011. **5**(4): p. 2984-2988.

37. Yang, Z., et al., Three-Dimensional Photonic Crystal Fluorinated Tin Oxide (FTO) Electrodes: Synthesis and Optical and Electrical Properties. Acs Applied Materials & Interfaces, 2011. **3**(4): p. 1101-1108.

38. Grinis, L., A. Ofir, and A. Zaban, Extending the current collector into the nanoporous matrix of dye sensitized electrodes. Journal of Physical Chemistry B, 2005. **109**(5): p. 1643-1647.

39. Liu, L., et al., Gallium-doped indium oxide nanoleaves: Structural characterization, growth mechanism and optical properties. Applied Surface Science, 2011. **258**(2): p. 923-927.

40. Yu, H.K., et al., Three-Dimensional Nanobranched Indium-Tin-Oxide Anode for Organic Solar Cells. Acs Nano, 2011. **5**(10): p. 8026-8032.

41. Lao, J.Y., et al., Hierarchical oxide nanostructures. Journal of Materials Chemistry, 2004. **14**(4): p. 770-773.

42. Yamaguchi, A., et al., Transparent nanoporous tin-oxide film electrode fabricated by anodization. Thin Solid Films, 2011. **519**(8): p. 2415-2420.

43. Renault, C., et al., Time-resolved UV-visible spectroelectrochemistry using transparent 3D-mesoporous nanocrystalline ITO electrodes. Chemical Communications, 2011. **47**(6): p. 1863-1865.

44. Hoertz, P.G., et al., Application of High Surface Area Tin-Doped Indium Oxide Nanoparticle Films as Transparent Conducting Electrodes. Inorganic Chemistry, 2010. **49**(18): p. 8179-8181.

45. Boettcher, S.W., et al., Harnessing the sol-gel process for the assembly of non-silicate mesostructured oxide materials. Accounts of Chemical Research, 2007. **40**(9): p. 784-792.

46. Yamauchi, Y., et al., Breakthrough and Future: Nanoscale Controls of Compositions, Morphologies, and Mesochannel Orientations toward Advanced Mesoporous Materials. Chemical Record, 2009. **9**(6): p. 321-339.

47. Sanchez, C., et al., Design, synthesis, and properties of inorganic and hybrid thin films having periodically organized nanoporosity. Chemistry of Materials, 2008. **20**(3): p. 682-737.

48. Carreon, M.A. and V.V. Guliants, Ordered meso- and macroporous binary and mixed metal oxides. European Journal of Inorganic Chemistry, 2005(1): p. 27-43.

49. Melde, B.J. and B.J. Johnson, Mesoporous materials in sensing: morphology and functionality at the meso-interface. Analytical and Bioanalytical Chemistry, 2010. **398**(4): p. 1565-1573.

50. Yang, P.D., et al., Block copolymer templating syntheses of mesoporous metal oxides with large ordering lengths and semicrystalline framework. Chemistry of Materials, 1999. **11**(10): p. 2813-2826.

51. Yang, P.D., et al., Generalized syntheses of large-pore mesoporous metal oxides with semicrystalline frameworks. Nature, 1998. **396**(6707): p. 152-155.

52. Hou, R.Z., P. Ferreira, and P.M. Vilarinho, A facile route for synthesis of mesoporous barium titanate crystallites. Microporous and Mesoporous Materials, 2008. **110**(2-3): p. 392-396.

53. Fattakhova-Rohfing, D., et al., Transparent conducting films of indium tin oxide with 3D mesopore architecture. Advanced Materials, 2006. **18**(22): p. 2980-+.

54. von Graberg, T., et al., Mesoporous tin-doped indium oxide thin films: effect of mesostructure on electrical conductivity. Science and Technology of Advanced Materials, 2011. **12**(2).

55. Wang, Y., et al., Ordered Mesoporous Sb-, Nb-, and Ta-Doped SnO_2 Thin Films with Adjustable Doping Levels and High Electrical Conductivity. ACS Nano, 2009. **3**(6): p. 1373-1378.

56. Pan, J.H., et al., Controlled formation of highly crystallized cubic and hexagonal mesoporous SnO2 thin films. Journal of Physical Chemistry C, 2007. **111**(15): p. 5582-5587.

57. Shao, S., et al., Synthesis and characterization of highly organized mesoporous palladium-doped tin dioxide thin films for gas sensing. Journal of Materials Chemistry, 2009. **19**(44): p. 8411-8417.

58. Shao, S., et al., Crystalline nanoporous metal oxide thin films by post-synthetic hydrothermal transformation: SnO(2) and TiO(2). Nanoscale, 2010. **2**(10): p. 2054-2057.

59. Hou, K., et al., Dye-Anchored Mesoporous Antimony-Doped Tin Oxide Electrochemiluminescence Cell. Advanced Materials, 2009. **21**(24): p. 2492-+.

60. Aksu, Y., et al., A Molecular Precursor Approach to Tunable Porous Tin-Rich Indium Tin Oxide with Durable High Electrical Conductivity for Bioelectronic Devices. Chemistry of Materials, 2011. **23**(7): p. 1798-1804.

61. Mueller, V., et al., Transparent Conducting Films of Antimony-Doped Tin Oxide with Uniform Mesostructure Assembled from Preformed Nanocrystals. Small, 2010. **6**(5): p. 633-637.

62. Turner, M.E., T.J. Trentler, and V.L. Colvin, Thin films of macroporous metal oxides. Advanced Materials, 2001. **13**(3): p. 180-183.

63. Shchukin, D.G. and R.A. Caruso, Inorganic macroporous films from preformed nanoparticles and membrane templates: Synthesis and investigation of photocatalytic and photoelectrochemical properties. Advanced Functional Materials, 2003. **13**(10): p. 789-794.

64. Chen, X., et al., Forced Impregnation Approach to Fabrication of Large-Area, Three-Dimensionally Ordered Macroporous Metal Oxides. Chemistry of Materials, 2010. **22**(12): p. 3583-3585.

65. Orilall, M.C., et al., Highly crystalline inverse opal transition metal oxides via a combined assembly of soft and hard chemistries. Journal of the American Chemical Society, 2008. **130**(28): p. 8882-+.

66. Velev, O.D., et al., Porous silica via colloidal crystallization. Nature, 1997. **389**(6650): p. 447-448.

67. Hatton, B., et al., Assembly of large-area, highly ordered, crack-free inverse opal films. Proceedings of the National Academy of Sciences of the United States of America, 2010. **107**(23): p. 10354-10359.

Chapter 2

Characterization methods

In this thesis, we employed various methods to characterize the properties of prepared TCO nanoparticles, the microstructure of nanoparticle-assembled porous TCO films as well as the device performance involving the application of porous TCO films. The main focus of this chapter is the description of these different characterization methods.

2.1. X-ray diffraction (XRD)

X-ray diffraction (XRD) studies the materials phase composition and crystal structure by utilization of electromagnetic radiation with the wavelength of only a few angstroms. It is one of the most important techniques in the research area of materials science.

In the general XRD setups, the X-rays are created inside a high vacuum tube, where the highly accelerated electrons from the anode collide with the cathode metal (such as Cu, Al, Mo, Mg) under a high voltage. The emitted X-ray spectrum is composed of two parts, the so-called ‘Bremsstrahlung’ and characteristic X-rays. The latter part results from the atomic relaxation by filling the lost inner shell electrons with upper shell electrons, which contains characteristic information of atomic species. The process of ‘Bremsstrahlung’ does not involve losing inner shell electrons, thus is no longer characteristic of a particular atom. Through the application of blocking filters, the characteristic X-rays with single wavelength can be obtained and then utilized for the experiments.

The interaction between X-rays and matter will result in different secondary effects, for example, scattering, absorption and reflection. The process of XRD is based on the scattering [1]. When the solid is illuminated with X-rays, the electrons circling around the atoms will become new radiation sources with the same phase, making the new scattering seem to emanate from the atomic centers. These simultaneous scattering waves from the atoms will interfere, both in phase and out of phase. The out of phase scattering waves (called destructive interference) cancel each other, while the in phase scattering waves (constructive interference) form enhanced waves and the process is called diffraction.

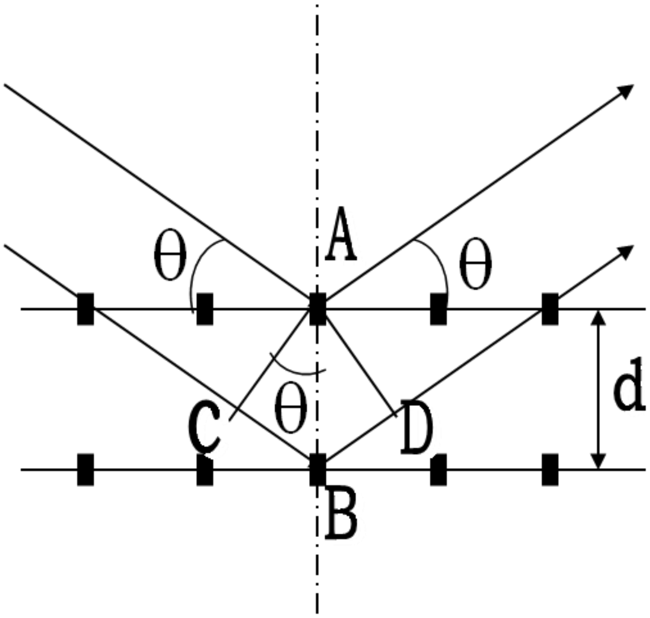

Figure 2.1 Schematic illustration of X-ray scattering.

Figure 2.1 depicts the optical paths of incident X-rays scattered by atom A and B. The diffraction can only happen when the paths of two X-rays differ by a whole number of X-ray wavelengths. That is,

$$\mathrm{BC} + \mathrm{BD} = \mathrm{n}\,\lambda$$

$$\text{since } \mathrm{BC} = \mathrm{BD} = \mathrm{AB}\sin\theta$$

$$\text{thus, } \mathrm{n}\,\lambda = 2\,\mathrm{AB}\sin\theta = 2\,\mathrm{d}\sin\theta$$

$$\mathrm{n}\,\lambda = 2\,\mathrm{d}\sin\theta \qquad \text{Equation 2.1}$$

The above equation 2.1 is the Bragg condition for diffraction. The value n gives the order of the diffraction, θ is the angle of incidence, λ is the X-ray wavelength, d is the plane-to-plane distance.

Bragg's equation describes the relationship between diffraction and plane-to-plane distance d. It means that, on the one hand, the diffraction happens only in solids which consist of periodic arrangement of atoms; on the other hand, the diffraction position corresponds to the characteristic information of the related crystal structure. Furthermore, the relative intensity of diffraction peaks depends on the type and arrangement of the atoms in the crystals. Thus, by analyzing the diffraction pattern (for example, comparing with the JCPDS cards in the database), one can have insights into the phase composition and crystal structure of the studied materials.

Besides, the information of crystallite size can be obtained from XRD measurements as well, as the peak broadening of the diffraction peaks depends on the domain size of the crystalline phase. The well-known Scherrer equation relates the crystal size with the diffraction peak width, by the form of full width at half maximum (FWHM):

$$\mathrm{D} = \frac{\mathrm{k}\,\lambda}{\beta\,\cos\theta} \qquad \text{Equation 2.2}$$

Where: D is crystallite size, k is the Scherrer constant (depending on the crystal shape) and generally set as 0.9, λ is the X-rays wavelength, β is full width at half maximum in radians, θ is incidence angle. The calculated value D denotes the average size of the studied crystalline phase. However, because the diffraction is volume based, a small number of larger crystals can dominate the scattering intensity, thus leading to wrong conclusions about the average size.

For the samples containing very small nanocrystals, the peak broadening effect leads to serious overlap between adjacent diffraction peaks. Therefore, various models to refine the diffraction peaks can be required in order to analyze the nano-crystalline phase. In our work, the XRD pattern refinement on the sample of indium tin hydroxide nanoparticles was done with our collaboration partner Goran Stefanic, at Ruđer Bošković Institute of Zagreb, Crotia.

Ordinarily, the atomic arrangement-induced diffraction happens at relatively high 2θ angle when employing Cu K_α as X-rays source, which is referred to as wide angle XRD. For the materials with a larger periodic distance, like a few nanometers for the pore to pore distance in the ordered mesoporous metal oxides, the diffraction occurs at much lower 2θ angle (below 10^o), which is called small angle XRD or small angle X-ray scattering (SAXS). In our work, small angle XRD was measured by the machine Scintag XDS 2000 (Scintag Inc.), while the wide angle XRD was performed with a Bruker D8 Discover with Ni filtered Cu K_α and a position-sensitive detector; both of the instruments have Cu K_α as the X-ray source.

2.2. Electron Microscopy

Electron microscopy is a versatile tool to reveal the nanostructure of the studied materials. This technique has the possibility to show the internal microstructure of the solids, the external surface morphology or the chemical composition of the sample by using transmission electron microscopy (TEM), scanning electron microscopy (SEM), or dispersive X-ray spectroscopy (EDS).

In electron microscopy, signals are investigated based on the interactions between the primary electrons and the electrons of the sample atoms [2]. Using the electron bombardment of the sample, the incident electrons can be absorbed, scattered and emitted by the sample. In figure 2.2, the different interacting processes are summarized.

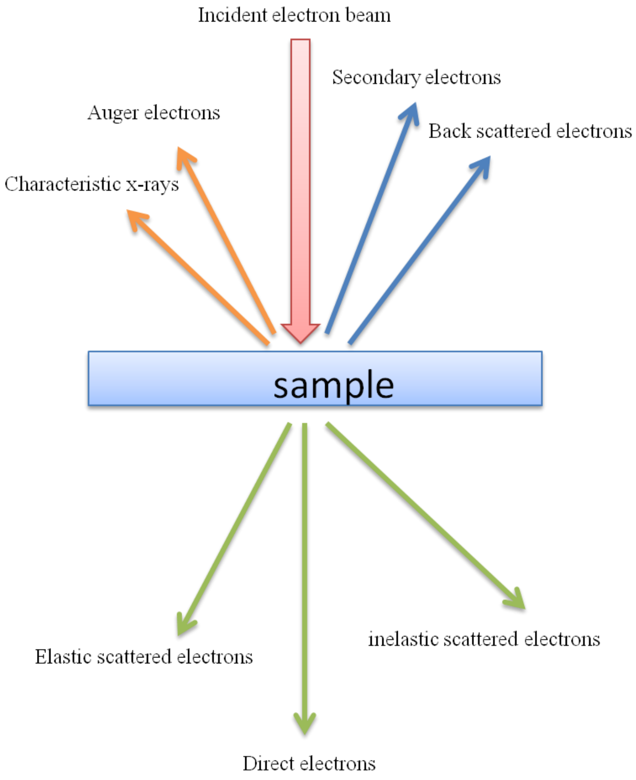
Incident electron beam
Secondary electrons
Auger electrons
Back scattered electrons
Characteristic x-rays
sample
Elastic scattered electrons
inelastic scattered electrons
Direct electrons

Figure 2.2 Secondary effects from interaction between incident electrons and materials. After Boothroyd [3].

Transmission electron microscopy (TEM)

The part of primary electrons being transmitted is responsible for transmission electron microscopy technique. Among them, the elastically scattered electrons (without losing energy) are mainly used to image the internal morphology of the sample; the inelastically scattered electrons (with energy loss) can be used to investigate the chemical composition, with methods such as EELS.

For TEM measurements, the electrons are accelerated at rather high voltages (usually about 80~400 keV). On the one hand, the high accelerating voltage induces the reduction in the electron wavelength and thus improves the image resolution; on the other hand, the penetration depth of electrons in the sample will be increased to allow the examination of thicker specimens. However, in order to have enough electrons to pass through and provide a sufficient signal intensity, the samples for TEM are normally required to be rather thin (less than 100 nm).

Scanning electron microscopy (SEM)

The secondary electrons originate from the effect of primary electrons striking the atoms in the near surface region of the sample. They normally have low energy (10-50 eV). In SEM, the secondary electrons detected through an Everhart-Thornley detector are used for surface imaging. The morphology can be visualized using the back-scattered electrons detected by a semiconductor device; these data are sensitive to atomic mass. In comparison to optical microscopy the achievable resolution is up to 100 times higher.

The SEM image is created by scanning the incident electron beam across the sample surface in a raster pattern, using accelerating voltages between 0.5 and 30 KeV. The beam position-synchronized brightness variation on the computer monitor generates the secondary electron image reflecting the surface morphology of the scanned area.

Electron diffraction technique

Analysis of the scattered electrons will give us information about the arrangement of the atoms in the sample, which is known as electron diffraction. The analysis follows the well known X-ray diffraction technique whereas they mainly differ in the applied wavelength. Considering the small electron wavelength and the geometrical electron-beam diagram for diffraction, the plane distance of the crystalline materials can be calculated by applying the equation 2.3.

$$r\,d = L\,\lambda \qquad \text{Equation 2.3}$$

Where: L corresponds to the camera length, λ is the electron wavelength, d is the plane distance and r is the distance between the undiffracted center and the diffracted spot.

The electron diffraction patterns of single crystals are composed of diffracted spots, corresponding to the crystal planes and comparable to a Laue pattern. In the case of polycrystalline samples, the random orientation of the crystal planes merges the scattered beams into bright rings on the diffraction pattern whereas the plane distance can be obtained by measuring the ring radius.

Energy dispersive X-ray spectroscopy

When the inner shell electrons are removed by the primary electrons, outer shell electrons fill the inner shell vacancies, accompanied by the release of characteristics X-rays. These signals contain the characteristic information of atomic species, which are usually utilized for chemical composition analysis.

In this work, TEM samples of the nanoparticles were prepared by evaporating a droplet of diluted solution containing the nanoparticles onto a continuous carbon grid. TEM samples of mesoporous TCO films were prepared by scratching off a tiny amount of material using a steel blade onto a honeycomb carbon grid. The morphologies of the nanoparticles were investigated by TEM and high resolution TEM. Electron diffraction patterns were analyzed to obtain crystallographic information. TEM and SEM methods were applied to illustrate the morphologies of mesoporous TCO films.

2.3. X-ray photoelectron spectroscopy (XPS)

X-ray photoelectron spectroscopy (XPS) utilizes the photo-ionization and energy-dispersive analysis of the emitted photoelectrons to investigate the elemental and chemical composition of surfaces. So far, it has been established as one of the most important techniques for studying the surface properties of solids and thin films.

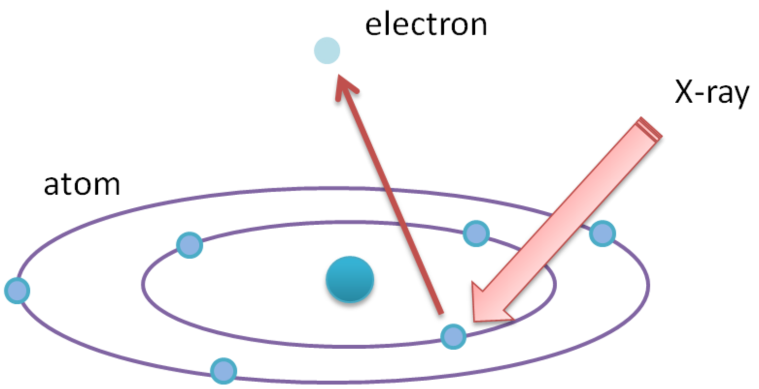

Figure 2.3 Generation of photoelectrons under the irradiation of X-rays

The process of photoelectron generation can be described by referring to figure 2.3. Under the irradiation of characteristic X-rays (such as Mg Kα, Al Kα), the core level electron bound to the atomic nucleus with energy E_B will absorb the photon energy hν, where h is Planck's constant and ν is the frequency of the incident photons. With the absorbed energy hν, a core level electron with sufficient energy can escape from the inner shell of the atom into the vacuum level. Thus, the photoelectron with kinetic energy E_k is created. The relationship among incident X-ray photon energy hν, E_B and E_K can be written as in equation 2.4 [4].

$$E_K = h\nu - E_B - \phi \qquad \text{Equation 2.4}$$

Here, ϕ is the work function of the spectrometer. As hν is known from the applied characteristic X-ray source, the binding energy E_B can be obtained from measuring the kinetic energy E_k. Considering that the binding energy is a unique property for each atom, the presence of peaks at different binding energies can be used to identify the elemental composition in the sample. However, for species with different valence states, the peak positions show slight shifts relative to their neutral counterparts, according to their local chemical environment and formal oxidation state in the atom. These effects are called chemical shifts. They are useful in distinguishing the oxidation states of metal cations.

The XPS measurement needs to be conducted in an ultrahigh vacuum environment (below 10^{-7} Pa) to provide an un-obstructed path for emission and detection of photoelectrons. Besides, the sample surface should be cleaned to minimize the contamination, since the energies of emitted photoelectrons are much less than 1 keV and have very low mean free paths in the material. Both Mg Kα (photon energy of 1253.6 eV) and Al Kα (photon energy of 1486.6 eV) are the commonly employed characteristic X-ray sources [5]. Depth profile analysis can tell chemical composition change as a function of depth. In our work, we did depth profile analysis on niobium doped titania nanoparticles by removing the surface atomic layers with Ar ions.

In this work, we used the software 'XPS peak fit' to carry out the fitting work. By comparison of the obtained peak position value with reference or database files, the chemical composition as well as the valence states of the atoms could be identified. Additionally, the fitting process also gives the integrated area under each peak. By referring to the element sensitivity factor S, the relative concentration between two different species that are co-present in the sample could be calculated from the equation 2.5 [6].

$$\frac{X_A}{X_B} = \frac{I_A / S_A}{I_B / S_B} \qquad \text{Equation 2.5}$$

Where: $\frac{X_A}{X_B}$ is the relative concentration between species A and B, I_A and I_B are the integrated areas under XPS peaks corresponding to species A and B, S_A and S_B are their sensitivity factors. It should be noted that A and B could be the same element but with different valence states.

For the doped metal oxides, valence states of the dopant atoms as well as the distribution of dopant atoms in the sample contain important information on the doping effect and the electrical properties. We employed XPS to obtain that information.

2.4. Thermal analysis (DSC and TGA)

Differential scanning calorimetry (DSC) and thermogravimetric analysis (TGA) are two commonly employed techniques to study materials' thermal properties, such as phase change, decomposition, liquid content as well as other temperature-dependent physical and chemical transitions.

Thermo gravimetric analysis (TGA) measures the weight change of a sample as a function of temperature and time. The weight change of the material at a certain temperature could be assigned to component volatilization, decomposition, oxidation/reduction reactions or other phase changes. Differential scanning calorimetry (DSC) measures the heat flow into or out of the sample with the change of temperature and time. The calorimetric measurement is performed by keeping the temperature of the sample and the reference constant while measuring the required energy difference (in order to keep the same temperature) between the sample and the reference. The amount of energy absorbed or evolved by the sample is recorded as a function of the temperature change and gives information about the thermodynamic nature of the weight loss process.

In this work, thermogravimetric analyses and digital scanning calorimetry measurements were performed using a Netzsch STA 440 C TG/DSC in synthetic air or nitrogen with heating ramps of 1 ^{o}C/min or 10 ^{o}C/min.

2.5. Dynamic light scattering (DLS)

Dynamic light scattering (DLS) is a very convenient method to study the hydrodynamic size and dispersion behavior of nanoparticles in colloidal solutions [7-8].

Basically, the nanoparticle colloidal solution is illuminated by a laser beam. Because of the Brownian motion of the nanoparticles, the laser light will be scattered, resulting in interferences both constructively and destructively. Thus, the scattering intensity, which is traced by the detector, shows time-dependent fluctuation. The fluctuation rate of the scattering intensity is related to the mobility of particles in the colloidal solution, and thus also particle size. In other words, small particles diffuse very fast and result in fast changing fluctuation, while larger particles move slowly in the solution and the fluctuation changes slowly as well. Therefore, by analyzing the fluctuation rate as a function of time, we are able to have insights into the particle size as well as its size distribution.

In the DLS instrument, through tracing the scattering intensity change, the information about the particle movement can be obtained through a second order auto-correlation function,

$$g^2(q;\tau) = \frac{\langle I(t)I(t+\tau)\rangle}{\langle I(\tau)\rangle^2} \qquad \text{Equation 2.6}$$

Where: q is the wave vector, I is the intensity and τ is the delay time. In the case of short time delays, the particles are not able to move too far from the initial states, while for long time delays, the particles' movements have no relation with their initial states any more. This delay can be explained by the diffusion coefficients in the solvent and if we assume that the particles are mono-dispersed with a single size distribution, it can be evaluated with Stokes-Einstein's equation:

$$D = \frac{kT}{3\pi\eta d} \qquad \text{Equation 2.7}$$

Where D is the diffusion coefficient, k is the Boltzmann constant, T is Kelvin temperature, η is the solvent viscosity, d is the hydrodynamic size of the particles.

For nanoparticles with a broad size distribution, laser light scattering from larger particles can be analyzed according to Mie theory, while scattering from small ones can be described by using Rayleigh scattering. The correlation between intensity fluctuation and particle size is summarized in the equation,

$$I = I_0 \frac{1 + \cos^2 \theta}{2R^2} (\frac{2\pi}{\lambda})^4 (\frac{n^2 - 1}{n^2 + 2})^2 (\frac{d}{2})^6 \qquad \text{Equation 2.8}$$

Where: I is the intensity of scattered light, I_0 is the intensity of incoming light, θ is the scattering angle, λ is the wavelength of the laser light, n is the refractive index of the nanoparticles, R is the distance to the nanoparticle, d is the hydrodynamic diameter.

As scattering intensity is proportional to d^6, the distribution of the particle size is actually dominated by larger nanoparticles, whereas the contributions from smaller ones are much weaker. Further mathematical treatments lead to volume based (d^3) and number based (d) distribution, which will be helpful for analyzing nanoparticles with large size variations.

2.6. Sorption

Sorption is the most widely used method to characterize the textural characteristics of porous materials. Surface area, pore volume, pore size, as well as the pore size distribution can be extracted from this measurement [9-10].

The general presence of weak energy sites on the solid surface is the physical origin for the sorption process, since the gas or vapor molecules get easily bonded (adsorbed) to these sites. The adsorbable substance in the fluid phase is called adsorptive, while the substance in the adsorbed state is called adsorbate. The solid material on which adsorption occurs is called adsorbent. Depending on the interaction between the adsorptive and adsorbent, sorption can be categorized into two different types, chemisorption and physisorption. Chemisorption involves the formation of chemical bonds between adsorptive molecules and the adsorbent, thus the adsorption process can proceed only when the adsorptive has a direct contact with the adsorbent.

Therefore, chemisorption generally results in the formation of a monolayer and the process is practically irreversible (desorption requires much higher energy). The physisorption is due to relatively weak Van der Waals' interactions. The process is normally reversible and can lead to the multilayer adsorption. For characterization of textural properties of porous materials, the physisorption is more suitable.

The amount of adsorptive molecules taken up by the adsorbent depends on the temperature, pressure, surface energy distribution, and surface area of the adsorbent. A plot of the adsorbate amount versus the pressure at a constant temperature is called sorption isotherm. According to the definition of IUPAC, there are six different types of sorption isotherms [10]. Among them, the type IV isotherm (depicted in Figure 2.4) corresponds to mesoporous materials.

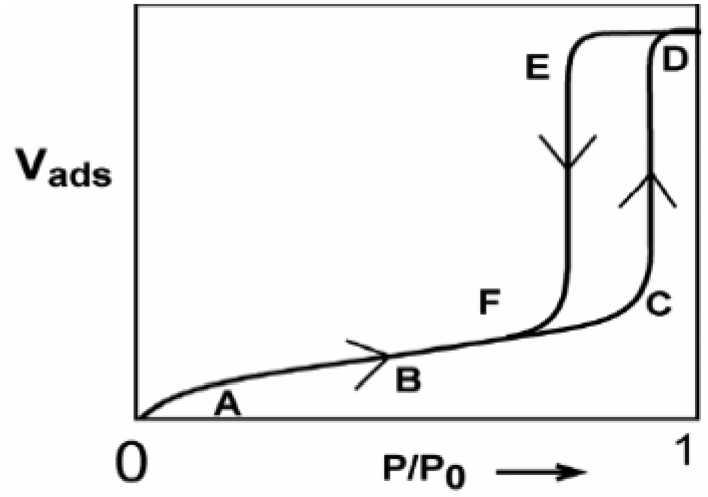

Figure 2.4 Type IV sorption isotherm

The whole adsorption branch is composed of initial part OA, rather linear part AB, BC, steep curve CD and the plateau, corresponding to monolayer adsorption, multilayer adsorption, capillary condensation and the complete filling of pores, respectively. Analysis on these specific parts provides the surface area, pore volume and pore size.

For example, based on the monolayer adsorption (AB), the interface area can be calculated from the theory of Brunauer-Emmett-Teller (BET), according to the equations 2.09 and 2.10:

$$\frac{\mathrm{p}/\mathrm{p}_0}{\mathrm{n}(\mathrm{p}_0 - \mathrm{p})} = \frac{1}{\mathrm{n}_\mathrm{m}\mathrm{C}} + \frac{\mathrm{C}-1}{\mathrm{n}_\mathrm{m}\mathrm{C}}\,\frac{\mathrm{p}}{\mathrm{p}_0} \qquad \text{Equation 2.09}$$

$$\mathrm{A}_\mathrm{S}(\mathrm{BET}) = \mathrm{n}_\mathrm{m}\mathrm{N}_\mathrm{A}\mathrm{a}_\mathrm{m} \qquad \text{Equation 2.10}$$

Here, p is the measured pressure, p_0 is the saturation pressure of the adsorptive, C is the BET constant, n_m is the monolayer capacity, n is the amount of the adsorbent, A_s is the BET surface area, N_A is the Avogadro constant, a_m is the cross-sectional area of the adsorptive molecules.

Furthermore, a type IV isotherm can also contain a hysteresis loop, FCDE in the figure 2.4. The hysteresis loop is usually associated with the filling and emptying of the mesopores by the capillary condensation. Generally, a steep hysteresis loop marks a narrow pore size distribution. Besides, the onset of the steep increase of the adsorption branch depends on the pore size; a higher relative pressure denotes a larger pore size. The characteristic features of some types of hysteresis loops are associated with certain well-defined pore structures.

In order to determine the texture parameters of thin porous films deposited on supports, whose total surface area is as small as several tens of cm^2 only, a highly-sensitive Kr adsorption technique has to be used. The most frequently used adsorptives, namely, nitrogen and argon at ca. 77 and 87 K, respectively, cannot be applied with materials such as thin porous films with very small surface areas. The reason is that the saturation pressures of nitrogen and argon at 77 and 87 K, respectively, are very high, reaching ca. 760 Torr, which leads to an extremely large number of molecules being trapped within the void volume of the sample cell. Because of a very small total pore volume and surface area of such thin porous films, the pressure changes due to the adsorption cannot be measured with a sufficient precision. As an alternative, an adsorptive with a substantially lower saturation vapour pressure should be used, such as krypton at the boiling point of liquid nitrogen, whose saturation pressure equals 1.63 and 2.63 Torr as a solid and a supercooled liquid, respectively.

The surface area can be calculated from an adsorption isotherm of Kr using the BET equation, the cross-sectional area of Kr equaling 0.21 nm^2. The information on the pore size and pore volume can be obtained from Kr isotherms by analyzing the shape of their hysteresis loop and the limiting adsorption at saturation pressure.

2.7. Characterization of Electrical Properties

2.7.1. Hall measurement with Van der Pauw method

Electrical properties such as dc conductivity, sheet resistance, charge carrier density and charge mobility are very important characteristics of transparent conducting oxides.

Conductance of the material reflects its ability to conduct an electrical current. It depends on the inherent conductance of the sample (called conductivity, or specific conductance) and its shape (geometrical parameters of the sample such as its length and the cross-sectional area) (equation 2.11).

$$\sigma = \frac{1}{\rho} = \frac{1}{R} \times \frac{l}{A}$$ Equation 2.11

Where: σ is the dc conductivity (S/cm), ρ is the resistivity (Ω cm), R is the resistance (Ω), l is the length or thickness of the sample (cm), A is the cross-sectional area (cm^2).

$$R = \frac{V}{I}$$ Equation 2.12

According to Ohm's law (equation 2.12), the resistance R can be known by applying a voltage (V, in the unit of volt) and measuring the current flowing (I, in the unit of amperes) through the sample, or vice versa. This is the basis of various approaches to measure the material's conductivity, such as two probe method, four-point method, or Van der Pauw technique.

The Van der Pauw method is a common method to measure the resistance of two-dimensional samples (usually the Van der Pauw measurement requires four Ohmic contacts placed on the boundary of the sample). The quality of Ohmic contacts, their small sizes, and the sample uniformity are important factors to ensure good measurements. The preferable contact configurations are shown in the figure 2.5 [11].

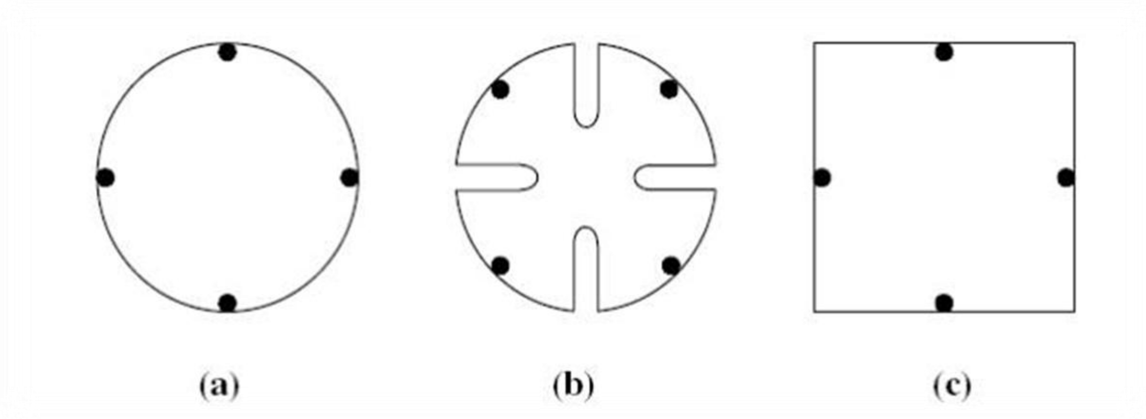

Figure 2.5 The recommended position of Ohmic contacts in Van der Pauw method [11]

In the Van der Pauw method, the bulk resistivity of the sample is calculated from its sheet resistance. To determine the sheet resistance R_s, two characteristic resistances R_A and R_B are required, which are calculated from a series of resistances measured among the four Ohmic contacts. Figure 2.6 describes the different combinations to perform resistance measurements on adjacent contact nodes [12].

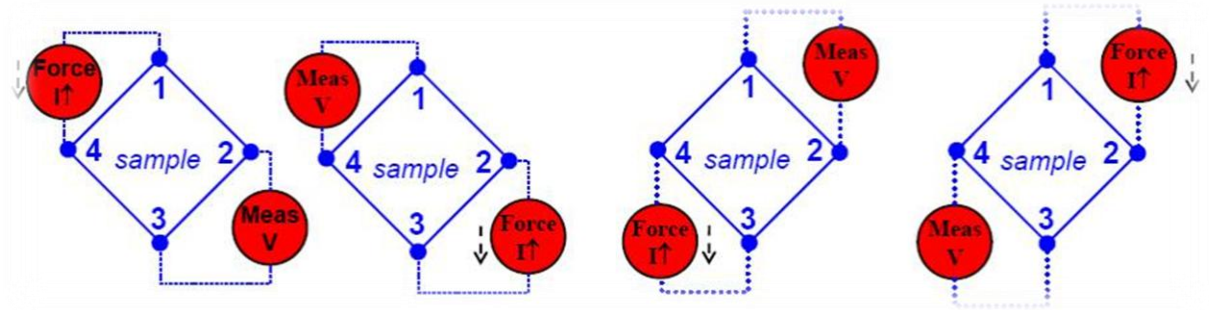
Force
I↑
1
4
sample
2
3
Meas
V
Meas
V
1
4
sample
2
3
Force
I↑
Meas
V
1
4
sample
2
3
Force
I↑
Force
I↑
1
4
sample
2
3
Meas
V

Figure 2.6 Resistance measurements on adjacent nodes [12]

We define:

$$R_{14,23} = \frac{V_{23}}{I_{14}}$$

Here, I_{14} is dc current injected from node 1 and taken out from node 4; V_{23} is dc voltage measured between node 2 and node 3, V_2-V_3.

Similarly, we have:

$$R_{23,14} = \frac{V_{14}}{I_{23}}$$

$$R_{41,32} = \frac{V_{32}}{I_{41}} \qquad R_{32,41} = \frac{V_{41}}{I_{32}}$$

$$R_{43,12} = \frac{V_{12}}{I_{43}} \qquad R_{12,43} = \frac{V_{43}}{I_{12}}$$

$$R_{34,21} = \frac{V_{21}}{I_{34}} \qquad R_{21,34} = \frac{V_{21}}{I_{34}}$$

The characteristic resistances R_A and R_B are calculated as:

$$R_A = \frac{R_{21,34} + R_{34,21} + R_{12,43} + R_{43,12}}{4} \qquad \text{Equation 2.13}$$

$$R_B = \frac{R_{32,41} + R_{41,32} + R_{14,23} + R_{23,14}}{4} \qquad \text{Equation 2.14}$$

Since R_A and R_B are related with sheet resistance R_s through the Van der Pauw equation, (equation 2.15) one can easily find the sheet resistance R_s:

$$\exp\left(-\pi\frac{R_A}{R_S}\right) + \exp\left(-\pi\frac{R_B}{R_S}\right) = 1 \qquad \text{Equation 2.15}$$

The product of the sheet resistance and sample thickness gives the bulk electrical resistivity **ρ** (equation 2.16), and its reciprocal value gives the dc conductivity **σ**.

$$\rho = R_S \cdot d \text{ (thickness)} \qquad \text{Equation 2.16}$$

The conductivity is a product of charge carrier concentration and charge mobility, thus, in order to extract the charge mobility, we need to know the charge carrier concentration n_c. The charge carrier concentration n_c can be obtained from the Hall voltage V_H (equation 2.19), from the Hall effect measurement. This measurement is based on the presence of a magnetic field which is perpendicular to the current flow in the sample. The magnetic field-induced Lorentz force will result in a Hall voltage V_H perpendicular to the applied electric field and magnetic field. V_H is measured through appliance of positive and negative magnetic field ($\vec{B}\perp$ or $\vec{B}\top$), while changing the injected current direction [12].

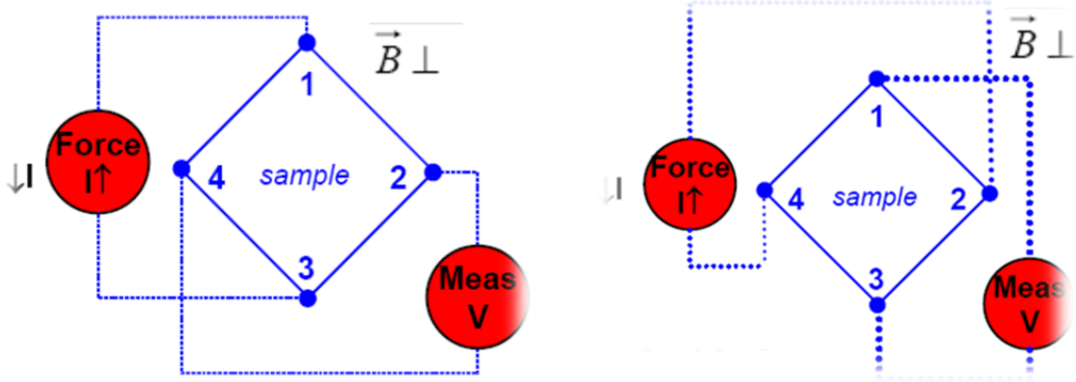

Figure 2.7 Hall voltage measurements on opposite nodes [12]

If we define:

$$V_C = V_{24P} - V_{24N}$$

Here, V_{24P} is the measured voltage between node 2 and 4 when applying positive magnetic field B; V_{24N} is the voltage when applying negative magnetic field B.

Similarly we have:

$$\mathrm{V_D = V_{42P} - V_{42N}}$$

$$\mathrm{V_E = V_{13P} - V_{13N}} \qquad \mathrm{V_F = V_{31P} - V_{31N}}$$

V_H is obtained by:

$$\mathrm{V_H = \frac{V_C + +V_D + V_E + V_F}{8}} \qquad \text{Equation 2.17}$$

Finally, charge carrier concentration n_c and charge mobility **μ** can be calculated from equation 2.18:

$$\mathrm{n_c = \frac{I \times B}{q \times V_H}}$$

$$\mu = \frac{\sigma}{\mathrm{q \times n_c}} \qquad \text{Equation 2.18}$$

Where: q is the elemental charge in C.

2.7.2. Time-domain terahertz spectroscopy

Terahertz spectroscopy (THz) involves the electromagnetic radiation with frequency of about 10^{12}Hz. Analysis based on the interaction between terahertz radiation and the matter (e.g., absorption, transmission) helps to understand the conduction properties, such as carrier transport behavior and conduction mechanisms [13-14].

The generation and coherent detection of ultra short terahertz pulses play fundamental roles for the THz technique. This can be realized by optical rectification in nonlinear crystals, such as zinc telluride. In the time domain terahertz spectroscopy, the generated terahertz pulses are first excited by the optical pump and then used to probe the sample. In this case, a large number of pump-probe delayed terahertz pulses can be measured after passing through the sample and these delayed pulses show stronger absorption comparing with non pump-excited terahertz pulses. The stronger absorption results from the generation of free charge carriers by the pumping process. Analysis of the evolution of the absorption spectrum against time can provide the life time, localization effects and transport behavior of free charge carriers. In this thesis, we obtained a THz analysis of niobium doped titania nanoparticles to elucidate the conduction mechanism in the terahertz range. The measurements were done by our collaboration partner Dr. Hynek Němec at the Physics Institute in Prague.

2.8. Cyclic voltammetry

Cyclic voltammetry (CVA) is an electrochemical technique used to study electrochemical reactivity of various species and the mechanisms of the electrochemical reactions [15]. In CVA, a linearly changing potential is applied on the working electrode being in contact with the electroactive species, and the resulting current during the potential scan is measured. The obtained current-potential curve is called cyclic voltammogram. In CVA, the potential of the working electrode is changed linearly with time between at least two potential values (called initial E_i or final E_f potential) with a constant scan rate (V/s). The potential direction can be reversed, so that the electrode reactions of the intermediates and the products formed during the forward scan can be detected. Single or multiple scans can be used.

The CVA experiments are usually performed in a three-electrode setup containing a working electrode at which the reaction of interest is investigated, a reference electrode (an electrode having a constant defined potential) and a counter electrode. They are immersed in an electrolyte (ionically conducting medium) which is not stirred in the typical CVA experiment, so that mass transport to the electrode takes place via non-stationary diffusion. The electroactive species can be either dissolved in the electrolyte and diffuse to the electrode surface, or be attached to the electrode surface using various techniques (deposition or immobilization).

The observed current is a superposition of all the currents flowing through the electrode interface, taking into account the opposite sign of the currents flowing in the opposite directions. Two basic contributions to the current are (i) non-Faradaic currents corresponding to the charging of the double layer formed at the electrode interface (approximated as a capacitor), and (ii) Faradaic current due to the transfer of electrons through the electrode interface (approximated as a resistance).

The current-potential dependence has typically a peak shape and is characterized by the peak values (peak current and peak potential). The exact shape of the voltammogram and the peak values depend on the character of the electrode reaction.

A cyclic voltammogram presented in figure 2.8 is typical of an electrode reaction in which the rate is governed by diffusion of the electroactive species to a planar electrode surface [16].

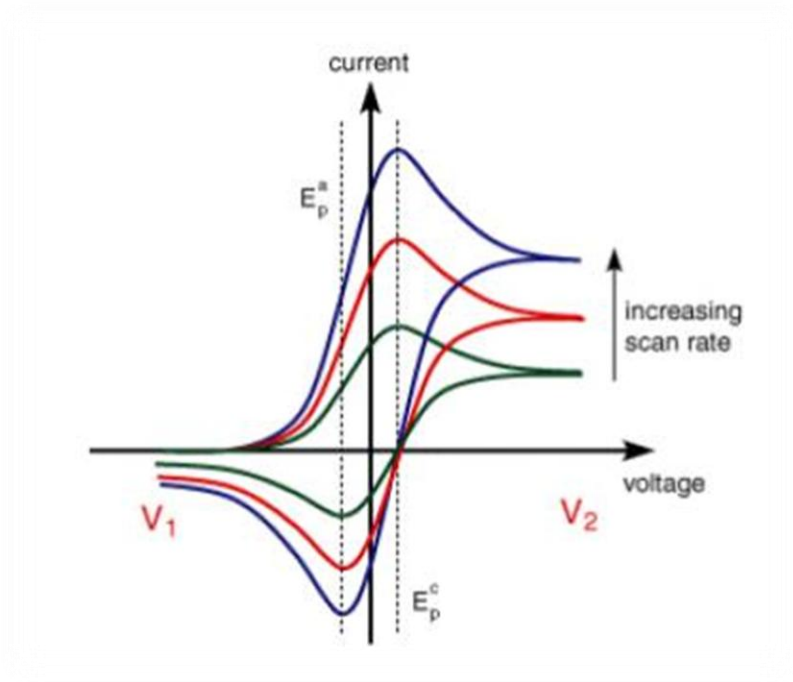

Figure 2.8 Typical cyclic voltammogram curve for single electron transfer reaction [16]

The obtained voltammogram is characterized by peak anodic potential E_{pa}, peak cathodic potential E_{pc}, as well as their corresponding peak current I_{pa} and I_{pc}. The difference between E_{pa} and E_{pc} defines the reversibility of the electron transfer reaction, according to the equation 2.19:

$$\Delta E = E_{pc} - E_{pa} \sim \frac{0.059}{n}(V) \qquad \text{Equation 2.19}$$

Where: n is the number of electrons transferred in the reaction, thus, for one electron process, ΔE should be about 0.059 V. A larger deviation from this value indicates a quasi-reversible reaction and slow charge transfer processes. Additionally, for ideal reversible reactions, the ratio between I_{pa} and I_{pc} should be equal to 1, while the values of E_{pa} and E_{pc} should be constant as a function of potential scanning rate.

The peak current is limited by the diffusion of the electroactive species to the electrode surface. The area under the peak is equal to the amount of electrons (charge) transferred between the electrode and the redox species. Therefore, it can be used to quantify the amount of the species anchored on the working electrode according to Faraday's law.

2.9. Fabrication and characterization of organic photovoltaics

The behavior and efficiency of the fabricated organic BHJ solar cells were characterized by current-voltage measurements (I-V measurement) [17]. In brief, the I-V curves were recorded by varying the applied external bias voltage and measuring the current response of the solar cell. The measurements can be done both in the darkness and under illumination with light. The characteristic I-V curve for organic solar cells is shown in Figure 2.9; it is specified by several important parameters [18]:

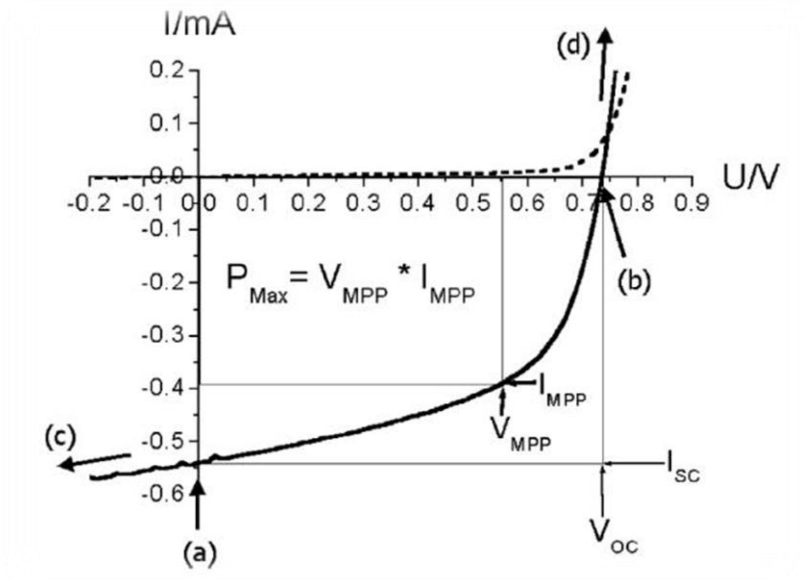

Figure 2.9 A characteristic I-V curve for organic solar cells [17]

Open voltage V_{oc}: it is limited by the energy difference between quasi-Fermi level splitting the free charge carriers, i.e., electrons and holes. The maximum charge separation point at zero current defines the value of V_{oc}.

Short circuit current I_{sc}: maximum current is crossing the solar cell at this point, but neither voltage nor power is generated.

Fill factor FF: FF is related to the quality of a solar cell, given by the ratio between the maximum power (arrived at point (V_{MPP}, I_{MPP})) and the product of V_{OC} and I_{SC}. This is shown in equation 2.20:

$$\mathrm{FF} = \frac{P_{Max}}{V_{OC} I_{SC}} = \frac{V_{MPP} I_{MPP}}{V_{OC} I_{SC}} \qquad \text{Equation 2.20}$$

Power conversion efficiency η: it denotes the overall energy conversion efficiency from the power of the incident light to electricity. Given by equation 2.21:

$$\eta = \frac{P_{Max}}{P_{In}} = \frac{V_{OC} I_{SC} FF}{P_{In}} \qquad \text{Equation 2.21}$$

Here, P_{in} is the incident power.

2.10. Chapter references

1. Connolly, J.R., Introduction to x-ray powder diffraction. 2009.
2. Goodhew, P.J., J. Humphreys, and R. Beanland, Electron microscopy and analysis. Third Edition. 2000: p. Taylor & Francis Publication, London and New York.
3. Boothroyd, C.B., Microanalysis in the electron microscope. Graduate lecture course in the University of Cambridge.
4. Raaen,S., Electronspectroscopy.http://www.phys.ntnu.no/~sraaen/dif4903/elspec.pdf.
5. http://www.uksaf.org/tech/xps.html.
6. Dacca, A., et al., XPS analysis of the surface composition of niobium for superconducting RF cavities. Applied Surface Science, 1998. **126**: p. 219-230.
7. Murphy, R.J., et al., Dynamic light scattering investigations of nanoparticle aggregation following a light-induced pH jump. Journal of Chemical Physics, 2010. **132**(19).

8. Pecora, R., Dynamic Light Scattering Measurement of Nanometer Particles in Liquids. Journal of Nanoparticle Research, 2000. **2**(2): p. 123-131.

9. Rouquerol, J., et al., Recommendations for the characterization of porous solids. Pure and Applied Chemistry, 1994. **66**(8): p. 1739-1758.

10. Sing, K.S.W., et al., Reporting physisorption data for gas solid systems with special reference to the determination of surface-area and porosity (recommendations 1984). Pure and Applied Chemistry, 1985. **57**(4): p. 603-619.

11. Schroder, D.K., Semiconductor Material and Device Characterization. 1998: p. Wiley Interscience Publication, New York.

12. Green, R., Hall Effect Measurements for Semiconductor and Other Material Characterization. 2011: p. Keithley Instruments, Inc.

13. Liu, Y., et al., Niobium-Doped Titania Nanoparticles: Synthesis and Assembly into Mesoporous Films and Electrical Conductivity. Acs Nano, 2010. **4**(9): p. 5373-5381.

14. Nemec, H., P. Kuzel, and V. Sundstrom, Charge transport in nanostructured materials for solar energy conversion studied by time-resolved terahertz spectroscopy. Journal of Photochemistry and Photobiology a-Chemistry, 2010. **215**(2-3): p. 123-139.

15. Bard, A.J. and L.R. Faulkner, ELECTROCHEMICAL METHODS. Fundamentals and Applications. 2001: p. John Wiley & Sons, Inc.

16. http://www.cheng.cam.ac.uk/research/groups/electrochem/JAVA/electrochemistry /ELEC/l4html/cv.html.

17. Szeifert, J.M., Mesoporous Titania Materials -Tuning and Optimizing Nanostructures and Porous Morphologies. 2011: PhD thesis submitted to LMU.

18. Hoppe, H. and N.S. Sariciftci, Polymer Solar Cells, in Photoresponsive Polymers II, Marder, S.R. and K.S. Lee, Marder, Editor. 2008. p. 1-86.

Chapter 3

Niobium doped titania nanoparticles: synthesis, assembly into mesoporous films and electrical conductivity

This chapter is based on the following publication:

Yujing Liu, Johann M. Szeifert, Johann M. Feckl, Benjamin Mandlmeier, Jiri Rathousky, Oliver Hayden, Dina Fattakhova-Rohlfing and Thomas Bein. ACS Nano, 2010, 4, 5373-5381.

3.1. Introduction

Transparent conducting oxides (TCO) with a regular mesoporous architecture have recently attracted attention owing to their ability to accommodate functional guest molecules in photovoltaic, electrochromic and chemical sensing applications, where the access of both photons and charge carriers to a high-surface area interface is of key importance [1-3]. However, the range of compounds that simultaneously feature electrical conductivity and optical transparency in the visible spectrum is limited [4]. TCOs usually consist of doped indium, tin, zinc or cadmium oxides; of these only tin-doped indium oxide (ITO) and antimony-doped tin oxide (ATO) have been prepared with a periodic porous morphology [1-3,5]. The synthesis of mesoporous electrodes from other classes of TCOs is of great interest, as it could substantially extend the library of available transparent conducting nanoarchitectures meeting the requirements of different optoelectronic applications.

In 2005, Furubayashi et al. [6,7] reported a metallic type conductivity of Nb doped anatase titania (NTO) films. Thin films, epitaxially grown by pulsed laser deposition, exhibit a conductivity of 10^3 - 10^4 S cm^{-1} and high optical transmittance in visible light, which makes them comparable with the much more expensive ITO. The conductivity mechanism was explained by the formation of an impurity band overlapping with the conduction band of anatase, and corroborated by first-principles band calculations showing that Nb doping does not change band dispersions except for filling the conduction band, implying that Nb atoms do not generate in-gap states [8].

The idea to synthesize mesoporous transparent titania-based electrodes is appealing, as titania films with controlled mesoporous structure can be easily prepared. An increase in electrical conductivity of the existing mesostructures due to doping with Nb atoms could open a way to inexpensive nanostructured TCO materials with controlled porosity. Moreover, the already known applications of titania, such as in photovoltaics, photocatalysis and charge storage, could greatly benefit from an increased electrical conductivity of the titania framework. This has recently been demonstrated by Huang *et al.*, who reported that higher conductivity of a TiO_2 electrode by Nb doping leads to enhanced photovoltaic performance [9].

Fabrication of periodic mesoporous Nb-doped titania films has been reported by Sanchez et al [10] and Wu et al [14], however, the electrical conductivity of those materials was not investigated. Disordered porous NTO powders [11, 13, 15] and films [12] have also been reported, but these materials were studied regarding their photocatalytic and electrocatalytic behavior. Additional studies dealing with the preparation of conducting titania materials usually involve physical processes or high temperature solid state reactions, which are not conducive for the fabrication of periodic porous nanostructures [16-29].

Periodic mesoporous titania films with controlled porous structure can be prepared by the self-assembly of amorphous titania sols, crystalline nanoparticles or a combination of both in the presence of surfactants acting as structure-directing agents [9, 30-32]. It was recently demonstrated for mesoporous thin films of antimony-doped tin oxide (ATO) that TCO nanocrystals can also serve as building blocks for the assembly of nanostructured transparent electrodes [33]. The doping level and thus the electrical conductivity can be precisely adjusted, because composition can be controlled in the particle synthesis. Due to the intrinsic crystallinity of the building blocks, crystalline mesostructures can be obtained already at moderate temperatures. However, the use of nanoparticles as the primary units for the assembly of mesoporous conducting films implies certain requirements to their properties. The particles should be just a few nanometer in size with a narrow particle size distribution, feature crystallinity and electrical conductivity, and should be dispersible in various solvents to form stable colloidal solutions. Synthesis of Nb-doped titania nanoparticles meeting those criteria has not been reported so far. Recently, we have reported that *tert*-butanol can be used as a novel reaction medium for the solvothermal synthesis of ultrasmall and highly dispersible nanoparticles [34]. The use of *tert*-butanol in microwave-assisted synthesis provides monodispersed nanosized particles of titania, whose size and crystallinity could be easily controlled by the variation of reaction temperature and time.

Here we describe the solvothermal synthesis of crystalline monodispersed niobium doped titania nanoparticles using *tert*-butanol as a reaction medium and an oxide source. Furthermore, the ability of the obtained nanocrystals to self-assemble into complex 3D mesoporous nanostructures, and the electrical conductivity of the nanoparticles and mesoporous films are investigated.

3.2. Results

3.2.1. Synthesis of Nb-doped TiO_2 nanoparticles and their assembly into mesoporous films

For the preparation of niobium doped titania nanoparticles, titanium tetrachloride and niobium(V) ethoxide were dissolved in *tert*-butanol. The particles with different Nb content are designated as NPX, where X is the Nb/(Nb+Ti) molar ratio in per cent. The clear solution was kept at different temperatures and different times in a laboratory oven in a Teflon-sealed autoclave. The solution turned turbid when the nanoparticles were formed. The particle size and crystallinity strongly depend on the reaction temperature. At 60 ^{o}C the particles are still completely amorphous, and an increase in the reaction temperature to 100 ^{o}C is necessary to obtain a crystalline phase (Figure 3.1). A further increase in the reaction temperature leads to larger crystalline particles. Thus, the size of the NP0 particles obtained after 12 hours of reaction at 100 ^{o}C and 150 ^{o}C is 10 nm and 14 nm, respectively.

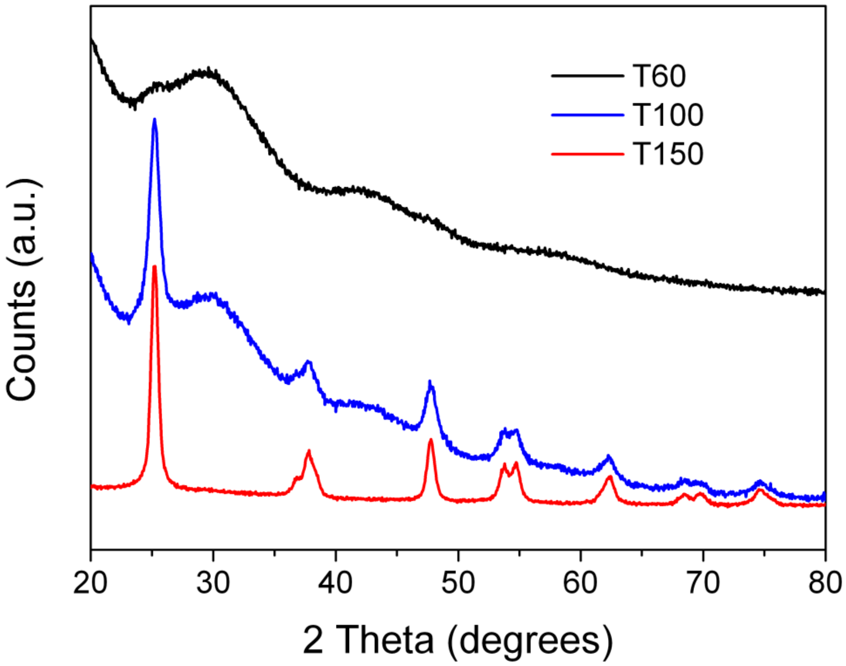

Figure 3.1 XRD patterns of as-produced NP20 TiO2 particles prepared by solvothermal reaction in tert-BuOH at different reaction temperatures (reaction time 12 hours).

An increase in the concentration of Nb leads to a delayed formation of particles. For the particles prepared at 100 ^{o}C the onset of crystallization was observed (by XRD) after 1.5, 3 and 4 hours for NP0, NP10 and NP20, respectively. This effect – also reported for other synthesis procedures [35, 13, 15] - is attributed to the suppression of particle crystallization due to Nb doping. Furthermore, the particle size at the same reaction temperature can be varied by changing the reaction time. While NP20 particles synthesized at 100 ^{o}C for 4 hours are only 4 nm in size, prolonging the reaction time to 20 hours increases the particle size to 13 nm (Figure 3.2b).

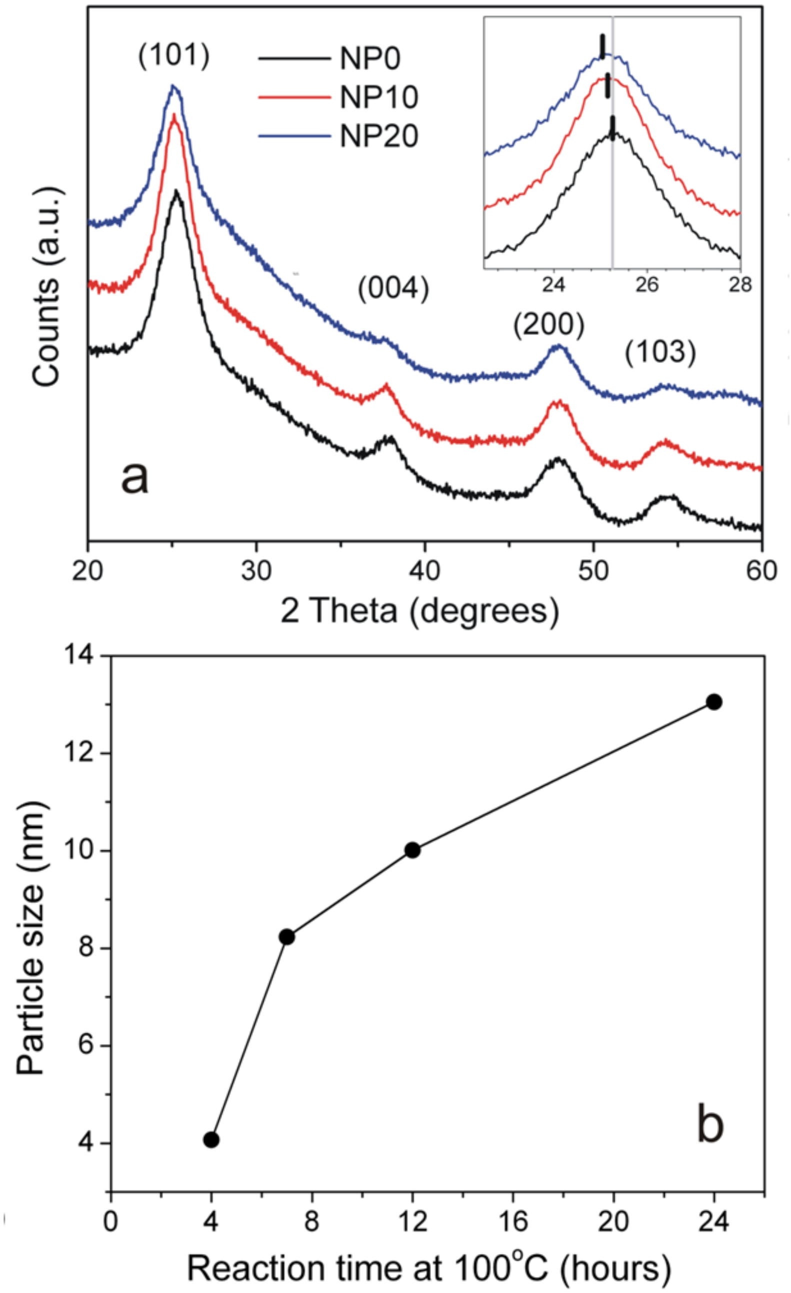

Figure 3.2 (a) XRD patterns of as prepared 0 %, 10 % and 20 % Nb-doped TiO2 nanoparticles synthesized by a solvothermal reaction in tert-butanol at 100oC for 1.5, 3 and 4 hours, respectively. The inset shows the position of the (101) peak. (b) Variation of the size of NP20 nanoparticles during synthesis in tert-BuOH at 100 oC with the reaction time. The particle size was derived from the peak broadening in the XRD patterns according to the Scherrer equation.

As we aimed at the preparation of crystalline nanoparticles as small as possible, the reaction at 100 °C was stopped just after the onset of crystallization. The NTO nanoparticles with different Nb content prepared this way are crystalline and average 4-5 nm in size (Table 3.1), as shown by HRTEM images (Figure 3.3) and XRD patterns (Figure 3.2 (a)). The XRD patterns of both pure and doped nanoparticles with up to 20 mol% titania show only one crystalline phase, either anatase or a phase structurally closely related to anatase (Figure 3.2 (a)). An increase in the Nb content leads to a shift of the (101) and (200) reflections to lower angles corresponding to the unit cell expansion of by about 5% due to the replacement of Ti^{4+} ions (radius 60.5 pm) by slightly larger Nb^{5+} ions (radius 64 pm) according to Vegard's law. The same changes in d-spacing with increasing Nb content were observed in the HR-TEM images of doped particles.

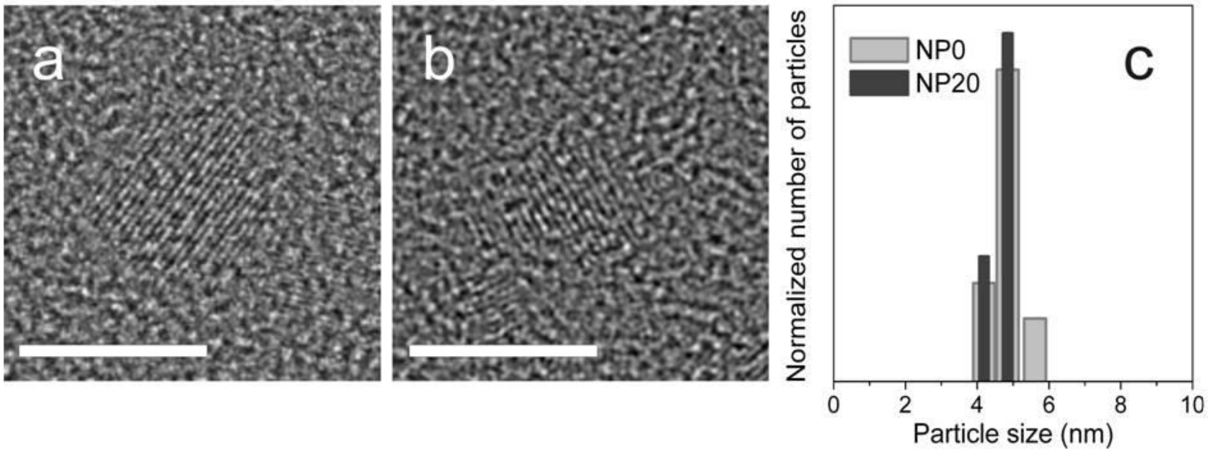

Figure 3.3 HR-TEM images of as-made NP0 (a) and NP20 (b) nanoparticles synthesized at 100 oC (scale bar corresponds to 5 nm), and the particle size distribution determined by DLS in tetrahydrofurane (c).

Table 3.1 Size of NTO nanoparticles prepared by a solvothermal reaction in *tert*-butanol at 100 ^{o}C determined by TEM (statistical evaluation of about 100 particles), XRD (by the Debye-Scherrer equation) and DLS.

Particle size	DLS	XRD	TEM
NP0	4.6 nm	4 nm	4.1nm
NP10	4.6 nm	4.1nm	-------
NP20	4.4 nm	4 nm	4 nm

All the nanoparticles can be dispersed easily in tetrahydrofurane (THF) at concentrations of more than 5 wt % of NTO in the presence of small amounts of hydrochloric acid, forming stable transparent colloidal dispersions. The particle size distributions obtained by DLS (Figure 3.3 (c)) are in a good agreement with those obtained from X-ray diffractograms.

To sum up, the undoped as well as Nb-doped titania nanoparticles prepared by the solvothermal synthesis in *tert*-butanol are crystalline, nanosized and dispersible, which makes them suitable building blocks for nanostructured materials assembly. We have examined the applicability of the as-synthesized nanoparticles for the assembly of mesoporous films using the commercial Pluronic F127 polymer as a structure-directing agent. Thin films designated as MS0, MS10 and MS20 were prepared from NP0, NP10 and NP20 nanoparticles, respectively. The synthesis times for the different samples were chosen such that the particle size of all samples was about 4 nm, in order to make the particles compatible with the surfactant-assisted self-assembly. In order to remove the template and to sinter the nanoparticles, the films were heated in air at 300 ^{o}C for 2 hours, because this is the lowest temperature sufficient for the removal of the Pluronic copolymer and the complete removal of organic residues from the interior of the pores in the thin films [32, 34].

The SEM images (Figure 3.4) show the surface of the mesoporous structures assembled from nanoparticles with varying Nb content. Depending on the composition of the nanoparticles used, the character of the mesostructure of the films differs significantly. The assembly of the undoped NP0 nanoparticles gives a worm-like open mesostructure with a homogeneous pore distribution. The films assembled from NP10 nanoparticles feature a channel-type mesostructure similar to that assembled from antimony doped tin oxide nanoparticles [33]. Finally, the NP20 particles provide films with a higher degree of pore ordering, resembling a cubic mesostructure with a d-spacing of about 17 nm. The thickness of the films assembled from particles with different doping levels is around 200 nm.

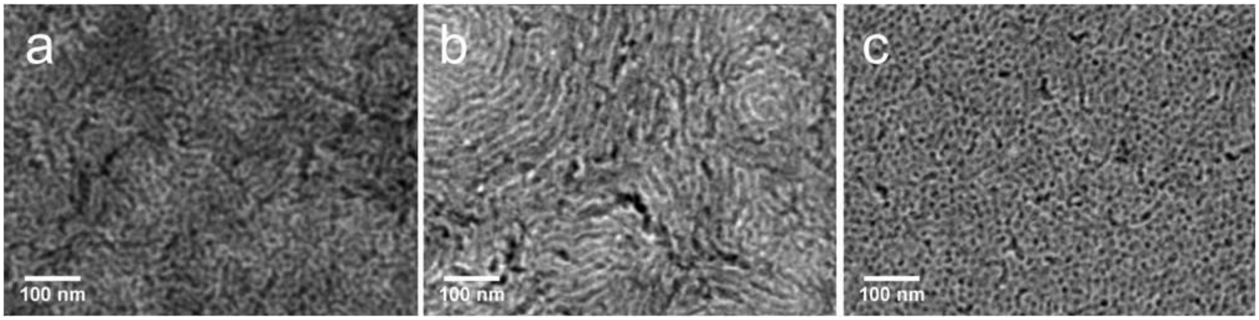

Figure 3.4 SEM images (top view) of MS0 (a), MS10 (b), and MS20 (c) films calcined in air at 300 oC.

The highly porous morphology of the films assembled from nanoparticles is also apparent in TEM images (Figures 3.5). The Fourier transforms of the TEM images show a ring corresponding to a mesostructure periodicity of 16±1 nm. Similar information about the mesostructure ordering is provided by the small angle XRD patterns (Figure 3.6), which exhibit a clearly distinguishable reflection for the MS10 and MS20 samples and a broad shoulder for a less ordered MS0 film.

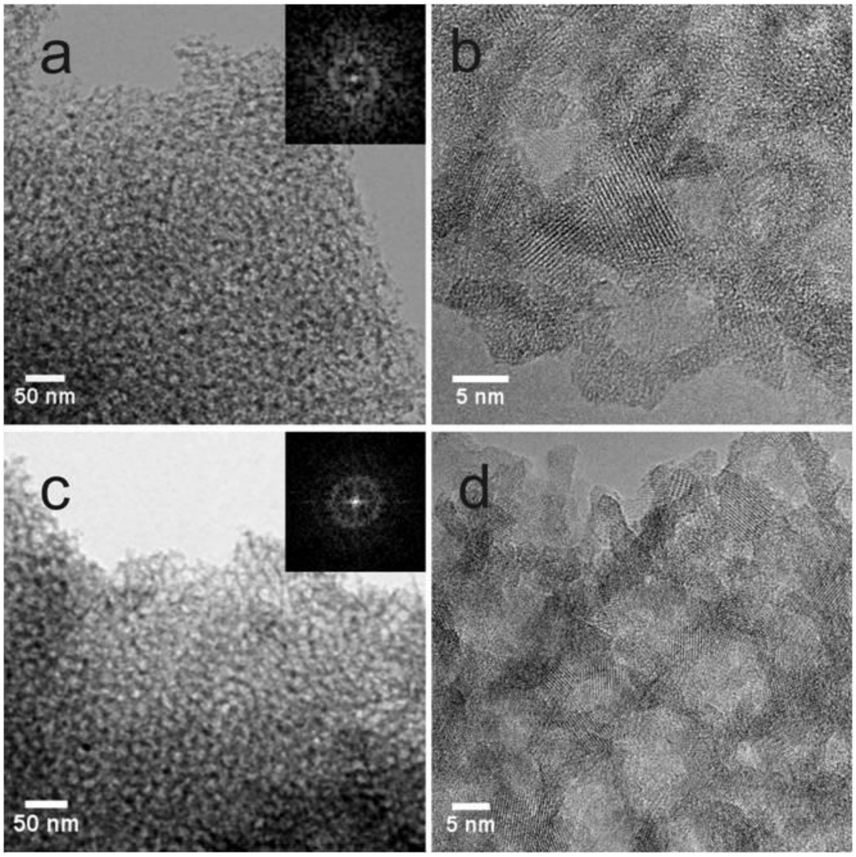

Figure 3.5 TEM (a,c) and HR-TEM (b, d) images of MS10 (first row) and MS20 (second row) samples calcined at 300oC. The insets in (a, c) show the Fourier transforms of the images.

The HR-TEM images show that the pore walls are composed of crystalline nanoparticles (Figure 3.5 (b), (d)). The high crystallinity of the films calcined at 300 ^{o}C was also proven by wide angle X-ray diffraction (Figure 3.7). The crystalline domain size calculated from the (101) reflection of the corresponding XRD patterns is about 7.5 nm and 6.5 nm for MS0 and MS20 films, respectively. This illustrates that the crystal size increases after calcination at 300 ^{o}C compared to the size of nanoparticles used for the films assembly.

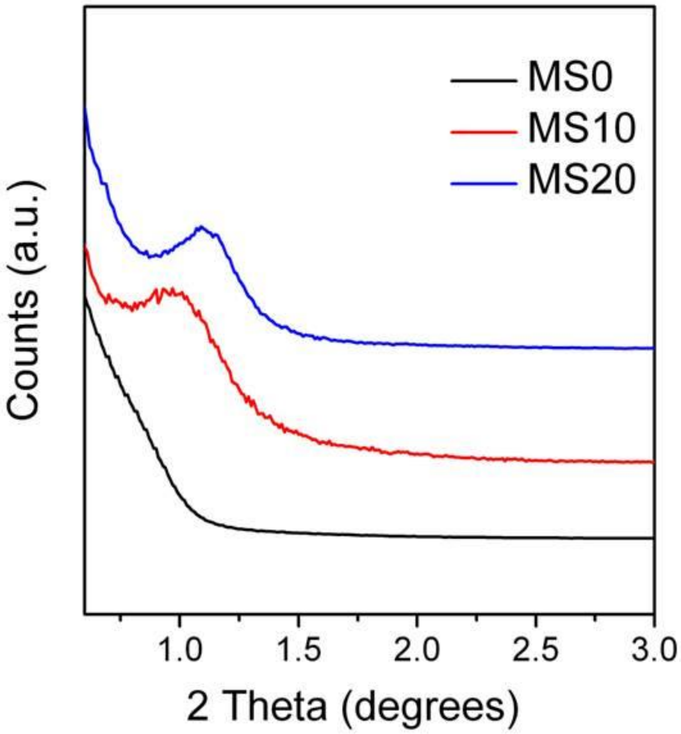

Figure 3.6 Small angle XRD pattern of mesostructured films MS0, MS10 and MS20 assembled from the corresponding nanoparticles after calcination at 300oC.

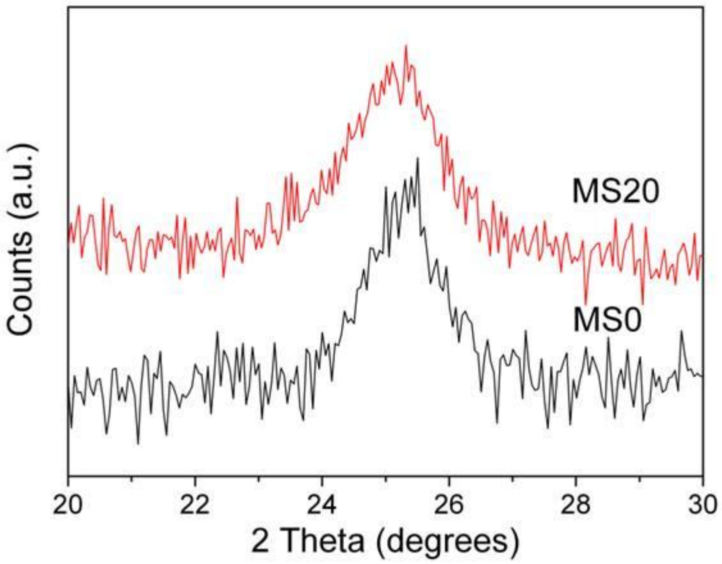

Figure 3.7 Wide angle XRD patterns of mesostructured films MS0 and MS20 after calcination at 300 oC ((101) reflection).

The textural properties and the accessibility of the internal surface of the thin films were studied by krypton adsorption at 77 K (Figure 3.8). The samples assembled from nanoparticles are characterized by an open porous structure without pore blocking. The use of particles with a higher Nb content provides films exhibiting a larger pore volume and surface area, in combination with a higher degree of periodicity of the mesostructure as could be seen in electron microscopy. The MS20 films feature the largest pore volume and a porosity of 43 %, with a surface area of 190 m^2/cm^3. The pore size determined from the Kr isotherm is 9-10 nm with narrow pore size distribution, as evidenced by the very steep adsorption and desorption branches. The isotherms of samples MS10 and MS0 are flatter, their pore size distribution is broader and the surface area is smaller (163 and 90 m^2/cm^3, respectively).

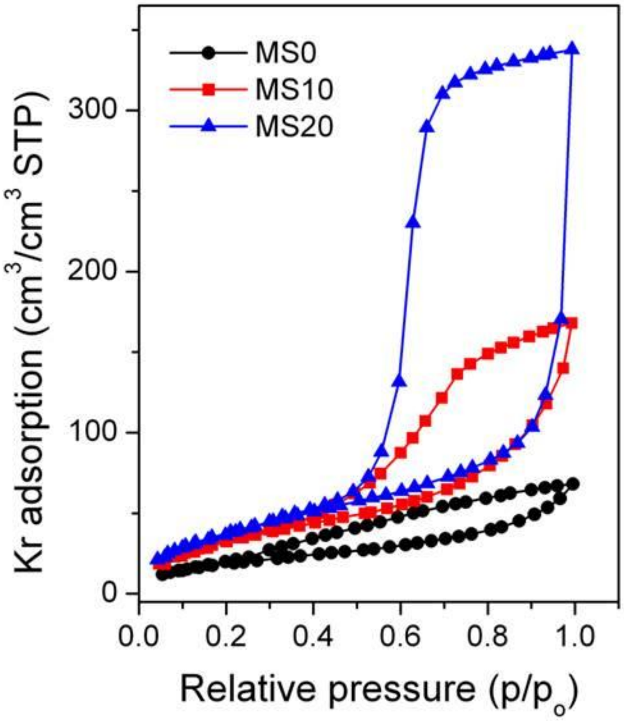

Figure 3.8 Kr adsorption isotherms at 77 K of templated mesoporous films assembled from nanoparticles with different Nb content: MS0 (black, circles), MS10 (red, squares) and MS20 (blue, triangles). All the films were calcined at 300 oC.

3.2.2. Electrical conductivity of Nb-doped TiO_2 nanoparticles

The valence state of the metal atoms in the Nb-doped titania lattice is an important indication of successful doping with regard to the electric conductivity, which is directly related to the specific defects formed in the doping process [36]. The valence state of the Ti and Nb in the nanoparticles containing 20% of Nb prepared in *tert*-BuOH at 100 °C was investigated using X-ray photoelectron spectroscopy (XPS) (Figure 3.9), which shows the peaks corresponding to oxygen, titanium and niobium. About 20 mol % of both titanium and niobium is found in their reduced states, Ti^{3+} and Nb^{4+} or lower [15], respectively, which is consistent with the Nb doping level of

20%. As each added Nb atom causes one extra electron that can reside in the form of reduced valence states of Ti or Nb, we assume that the extra electrons are not compensated by other easily formed defects such as Ti vacancies or oxygen interstitials. Therefore, the introduction of Nb^{5+} ions into the titania lattice leads to the donation of electrons into the conduction band and thus an increase in the charge carrier concentration. The presence of the reduced species due to the Nb doping is also reflected in the particle color. The as-prepared Nb-doped nanoparticles are bluish-green after pressing them into a pellet, the color being more intensive for the larger particles, while the undoped TiO_2 particles remain white.

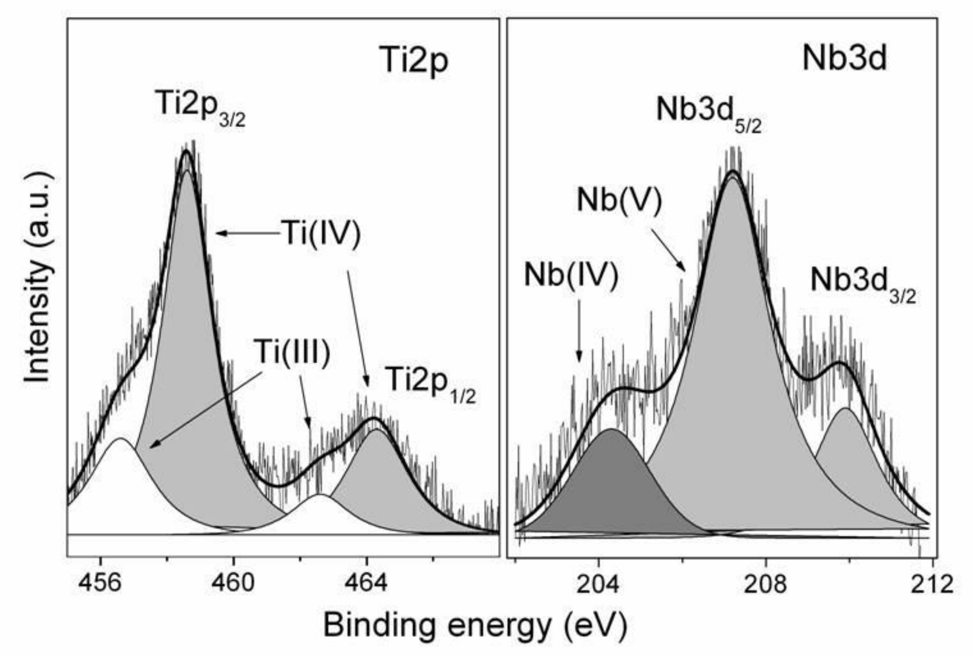

Figure 3.9 XPS spectra of as-prepared NP20 nanoparticles synthesized in tert-BuOH at 100 oC. The peaks were assigned according to refs [26, 37, 38, 39].

In spite of the presence of Ti in the reduced state, the room temperature electrical *dc*-conductivity of the crystalline nanoparticles prepared at 100 ^{o}C is still quite low, *ca.* $1\cdot10^{-6}$ S cm^{-1} for undoped and $2\cdot10^{-5}$ S cm^{-1} for the 20% doped nanoparticles, which is comparable with the data reported by Huang et al. [9] for the pressed NTO nanoparticles prepared by hydrothermal synthesis. This could be due to a strong localization of the free electrons and their low mobility. To further improve the electrical conductivity, the as-produced NTO nanoparticles have to be heated in non-oxidizing atmosphere such as nitrogen at 400 - 600 ^{o}C (Figure 3.10). Heating in air leads to an irreversible loss of conductivity, which also indicated by the change in the particle color to deep-blue or white after heating in N_2 or air, respectively. The change in the conductivity with the Nb content was found to be nonlinear. The introduction of Nb in the anatase lattice drastically increases the conductivity by several orders of magnitude, the highest conductivity being found for the 20 % Nb sample, for which the conductivity and the carrier concentration obtained from Hall effect measurements were 0.25 S cm^{-1} and 10^{20} cm^{-3}, respectively. A further increase in the Nb content does not lead to further improvement. The maximum conductivity was obtained for a much higher Nb concentration than for materials prepared by physical methods, for which the highest conductivity is observed already at 3 % of Nb [40].

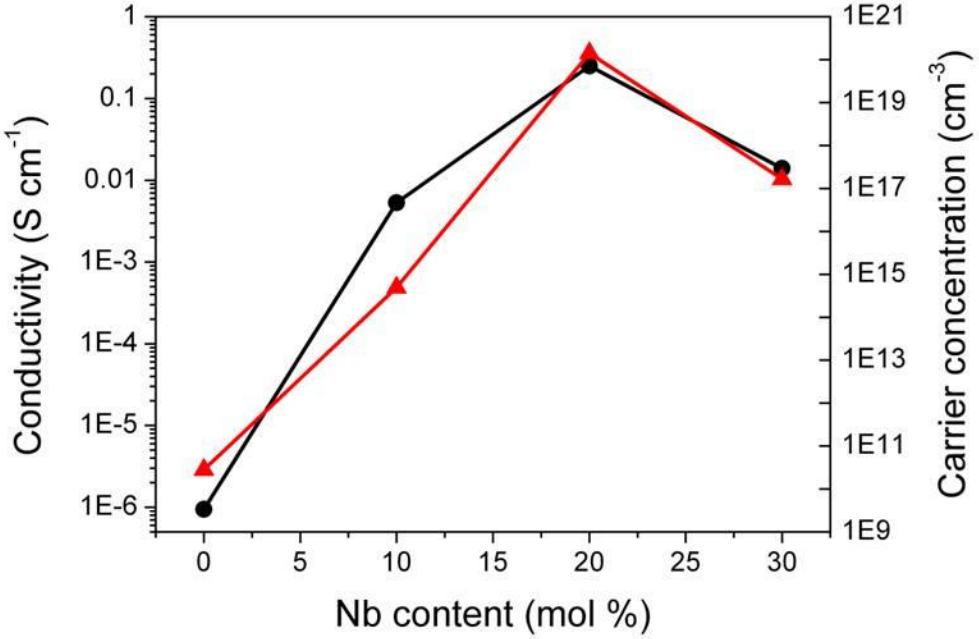

Figure 3.10 Specific conductivity (black, circles) and charge carrier concentration (red, triangles) of the pellets pressed from Nb-doped nanoparticles and heated at 600 oC in N2, as a function of Nb content. The axes are shown in logarithmic scale.

XPS measurements at different depths from the particle surface performed after polishing the particles with argon ions reveal that the surface composition of the particles after heating in N_2 at 600 ^{o}C differs from that of the bulk. As the niobium content reaches 30.0 % at the surface and 19.8 % in the bulk, respectively, the particle surface is enriched with niobium. At the surface, both titanium and niobium are in their highest oxidization states (Figure 3.11). On the contrary, in the particle core a part of the titanium atoms is also present as Ti^{3+} cations, their fraction (16 %) being similar to the amount of Nb^{5+} cations introduced in the synthesis (about 20 %). This indicates that most of the extra electrons generated by Nb doping are released into the conduction band of TiO_2, leading to the formation of Ti^{3+} and resulting in the high conductivity [8].

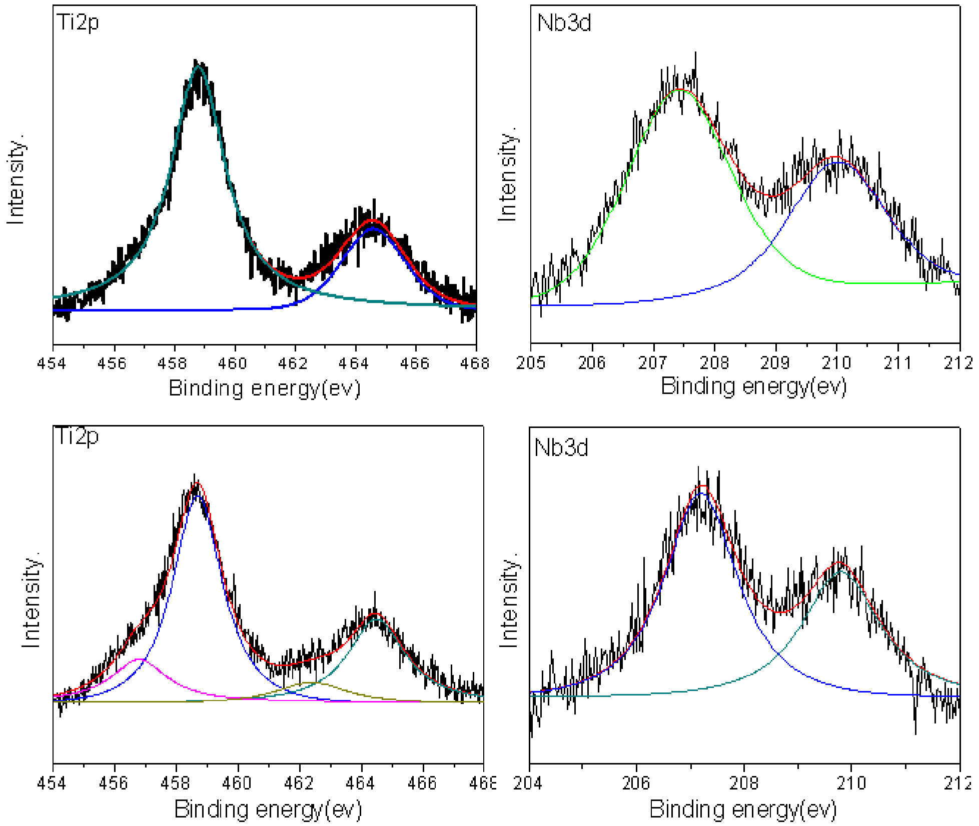

Figure 3.11 XPS of NTO particles prepared in tert-BuOH at 60 oC and heated in N2 at 600 oC after Ar+ polishing for 5 min (first row) and for 30 min (second row). Polishing rate is 1500 eV s-1.

The electrical conductivity of mesoporous thin films assembled from different types of nanoparticles is much lower than that of the heated particles and shows much smaller variation with the Nb content. Thus, the conductivity of the doped MS20 films (10^{-4} S cm^{-1}) is only about two times larger than that of the pure titania film.

3.3. Discussion

The results above show that *tert*-butanol is a suitable reaction medium for the fabrication of crystalline monodispersed nanoparticles. The reaction in *tert*-butanol can be carried out both using microwave heating, as described in our previous publication [34], and solvothermally at mild temperatures, leading to highly dispersible nanoparticles. The size of the particles and their degree of crystallinity can be controlled by reaction temperature and reaction time, thus enabling the preparation of particles 4 nm to 15 nm in size. Besides the pristine oxides, the solvothermal reaction in *tert*-butanol is suitable for the preparation of doped nanoparticles with homogeneously distributed dopant within the host lattice (before heat treatment, as the latter can lead to surface enrichment as was shown above by the XPS data) Following this synthesis route, the anatase lattice can incorporate more than 20% of Nb ions. The incorporation of the guest impurities slows down the crystallization rate and leads to some expansion of the anatase lattice.

In contrast to the titania particles prepared by the well-established solvothermal synthesis in benzyl alcohol [41], the particles of similar size and crystallinity synthesized in *tert*-butanol can be easily dispersed up to high concentrations in THF to form stable colloidal dispersions. This can be attributed to their different surface chemistry. The different surface properties of nanoparticles synthesized either in aromatic or aliphatic alcohols are the reason for their different ability to self-organize into periodic mesoscopic structures directed by the block copolymers of the poly-alkylene oxide type. The particles prepared using *tert*-butanol assemble into regular mesostructures directed by the Pluronic templates, while those obtained using benzyl alcohol provide only disordered structures with these templates [32]. The films assembled from doped titania nanoparticles exhibit a higher degree of mesostructure ordering than those prepared from undoped ones, which may be due to the different surface properties of nanoparticles with varying Nb content. A similar behavior was observed for the ATO nanoparticle system [2, 33]. Generally, the assembly of mesoporous films from particles has a beneficial effect on the porosity in comparison with sol-gel films, especially regarding the open nature of the porous system and as a result the better accessibility of the inner surface [32]. Doping with niobium leads to an enhancement of the mesostructure periodicity, the surface area and the pore volume.

The incorporation of Nb drastically increases the electrical conductivity of the nanoparticles. The maximum conductivity at room temperature of the 20 % Nb-doped sample, reaching 0.25 S cm^{-1}, is remarkably high for the wide band gap semiconductor titania. It supports the assumption that a considerable increase in the electrical conductivity of the anatase lattice is possible due to extrinsic doping with niobium ions. The only other study published to date on the chemical preparation of conducting Nb-doped titania nanoparticles by Huang et al [9] gives similar values of conductivity of as-produced nanoparticles and thus an additional support to the suitability of chemical routes for the preparation of conducting titania particles. Their conductivity is, however, still much lower than the range of 10^3–10^4 S cm^{-1} reported by Furubayashi et al [6,17,8] for epitaxially grown NTO films. It appears to be a general feature of the polycrystalline TCO systems prepared by chemical methods [1,33] that their DC conductivity is lower than the conductivity of analogous materials prepared by physical deposition techniques such as evaporation or magnetron sputtering. This difference is attributed primarily to grain boundary scattering in the polycrystalline material and the larger amount of defects and imperfections in the nanosized crystals. Moreover, for the Nb-doped titania the situation is even more complicated due to the specific properties of this system. In contrast to the conventionally used indium or tin oxides, which can form solid solutions with various dopants causing only limited distortion of the host crystalline lattice [4], incorporation of Nb into the anatase lattice can cause a noticeable lattice expansion or lattice deformation reported also by other authors [39], which generally leads to the decreased electron mobility [4]. Moreover, donated electrons are susceptible to compensation by easily formed defects, such as Ti vacancies or oxygen interstitials [26, 42].

Further improvement of the electrical conductivity requires an optimization of the reaction conditions. It appears that at least two factors are important for obtaining a niobium doped titania degenerate semiconductor. First, doped Nb atoms must be homogeneously distributed within the anatase lattice. Second, the formation of other defects except for the replacement of tetravalent Ti with pentavalent Nb should be avoided, as the extra electrons caused by Nb doping and existing in the form of Ti^{3+} and/or Nb^{4+} are easily compensated by titanium vacancies or oxygen interstitials. The conductivity of the as-prepared nanoparticles is rather low and can be substantially increased by a treatment at elevated temperatures in non-oxidizing atmosphere. The reasons that can contribute to the greatly enhanced conductivity of the pressed particle pellets after thermal treatment are particle growth, particle sintering and combustion of the organic residues acting as an insulator. However, such a treatment can lead to the undesired partial surface segregation of Nb due to a “self-purification” process described for NTO as well as for other doped oxides due to the size mismatch of the metal cations [26, 43, 44].

The mesoporous layers assembled from the Nb-doped titania nanoparticles show very good structural properties such as the periodicity of the porous system, a uniform pore size, a high pore volume, a large surface area and crystallinity of the walls. However, the increase in conductivity due to Nb doping is much less pronounced for the mesoporous films than for the similarly treated particles. We tentatively attribute this (i) to the much smaller size of the crystals in the walls of the mesoporous films compared to that of the pressed pellets after heating (7 nm and 22 nm, respectively) due to the confining effect of the template, and (ii) the oxidation of a surface layer by adsorbed oxygen molecules upon exposure to air due to the high surface area of the films.

Now that the concept has been proven to be successful for making periodic porous conducting architectures on the basis of Nb-doped titania, future efforts should be aimed at the improvement of the conductivity of the mesoporous films. One of the ways to increase the conductivity can be the use of the bigger crystals for the mesostructure assembly, which would require larger amphiphilic polymers [45]. Further optimization of non-oxidizing processing methods for particle sintering is also necessary. In this respect, a “brick and mortar” approach which has been used successfully for the preparation of highly crystalline mesoporous titania films [32] could be one of the possibilities to sinter the crystals at lower temperatures and thus to minimize the surface segregation.

3.4. Conclusions

The solvothermal procedure developed in this study enables the preparation of crystalline doped and undoped non-agglomerated dispersible titania nanoparticles with a narrow particle size distribution and homogeneous incorporation of doping atoms within the host lattice. The particle size and crystallinity can be controlled by the reaction temperature and time. Substitutional doping with niobium ions drastically increases the electrical conductivity of the titania particles. In contrast to the titania particles prepared by a solvothermal synthesis in benzyl alcohol, those of similar size and crystallinity synthesized in *tert*-butanol can be easily dispersed at high concentrations in THF to form stable colloidal dispersions, which can be attributed to different surface chemistry. The Nb-doped titania nanoparticles can be assembled into regular three-dimensional mesoporous structures with a narrow pore size distribution and high surface area.

3.5. Experimental part

All chemicals were purchased from Sigma-Aldrich and used as received. *tert*-Butanol and benzyl alcohol were dried over 4 Å molecular sieve at 28 °C and filtered prior to use. Pluronic F127 ($EO_{106}PO_{70}EO_{106}$, where EO is ethylene oxide, PO is propylene oxide) was purchased from Sigma-Aldrich.

For the synthesis of niobium-doped titania nanoparticles with different Nb contents, $TiCl_4$ and $Nb(OEt)_5$ were added to *tert*-butanol (12 mL, 1.8 mmol) under continuous stirring. The particles with different Nb content are designated as NPX, where X is the Nb/(Nb+Ti) molar ratio in per cent. As an example for the preparation of NP20 nanoparticles, 0.16 ml (1.44 mmol) of $TiCl_4$ and 0.09 ml (0.36 mol) of $Nb(OEt)_5$ were used. The clear solution was kept at 100 ^{o}C in a laboratory oven in a Teflon-sealed autoclave. The reaction time was 1.5 h, 3 h and 4 h for NP0, NP10 and NP20 nanoparticles, respectively. The resulting nanoparticles were separated by centrifugation at 50.000 rcf for 15 minutes. The particles separated this way contain 25 – 50 % of organic residues as determined by thermogravimetric analysis (Netzsch STA 440 C TG/DSC).

For the fabrication of mesostructure films, a solution of Pluronic F127 (0.07 g, 0.006 mmol) in THF (2 mL) was added to 0.2 g of non-washed particles previously separated by centrifugation (metal oxide content was 1.75 mmol as determined by TGA analysis), and stirred until the particles were homogeneously redispersed. Concentrated HCl (0.2 ml) was added to obtain a clear transparent solution. The mesoporous films were fabricated by dip coating of prepared solutions on various substrates (Si wafer, glass) at a relative humidity of 50 % - 60 % and 25 ^{o}C. The films were heated in air at 300 ^{o}C for 2 hours and/or in N_2 at 500 ^{o}C for 2 hours, with a ramp speed of 0.5 ^{o}C min^{-1} for each heating step. The average thickness of the films after heating is around 200 nm.

Wide angle X-ray diffraction analysis was carried out in reflection mode using a Bruker D8 Discover diffractometer with Ni-filtered CuK$_{\alpha}$-radiation (λ = 1.5406 Å), and equipped with a Vantec-1 position-sensitive detector. The crystal lattice d spacing and particle size calculation were based on the Bragg equation and Scherrer's equation. The dispersion behavior of nanoparticles was studied by dynamic light scattering using a Malvern Zetasizer-Nano equipped with a 4 mW He-Ne laser (633 nm) and an avalanche photodiode detector.

High Resolution Transmission Electron Microscopy (HRTEM) was performed using a FEI Titan 80-300 instrument equipped with a field emission gun operated at 300 kV. The particulate samples were prepared by evaporating a drop of a diluted suspension of particles in THF on a Plano holey carbon coated copper grid. HRTEM of films was carried out by removing the thin-film samples from the substrate and transferring them onto a holey carbon coated copper grid. Scanning electron microscopy (SEM) was performed on a JEOL JSM-6500F scanning electron microscope equipped with a field emission gun, at 4 kV.

Small angle X-ray diffraction was carried out using a Scintag XDS 2000 diffractometer (Scintag Inc.), with a Ni-filtered Cu K_α-radiation (λ = 1.5406 Å) with theta/theta geometry and a scintillation detector operated at 40 kV and 30 mA. The textural properties of mesostructured films were analysized with Kr adsorption/desorption measurements at 77 K using an ASAP 2010 apparatus (Micromeritics).

Electrical conductivity measurements on NTO nanoparticles were performed on pellets prepared by pressing finely ground nanoparticles under a pressure of 10 tons cm^{-2}. To further improve conductivity, thermal treatment under a nitrogen atmosphere was performed at 600 ^{o}C for 2 hours, with the ramp of 5 ^{o}C min^{-1}. The Hall mobility, charge carrier density and conductivity were measured by the Hall method (ECOPIA HMS 3000) using a magnetic field of 0.55 T.

X-ray photoelectron spectroscopy (XPS) analysis of the particles on a silicon substrate was performed using a VSW HA 100 electron analyzer and the K_α radiation provided by a non monochromatized magnesium anode system (Mg K_α = 1253.6 eV). Ar ion polishing was done at a rate of 1500 eV s^{-1}. The recorded elemental peaks were fitted by Gaussian-Lorentzian profiles and the elemental ratios were calculated by the equation $\frac{X_A}{X_B} = \frac{I_A / S_A}{I_B / S_B}$, where I_A/I_B is the ratio of fitted areas, and S is the sensitivity factor [38].

3.6. Chapter references

1. Fattakhova-Rohfing, D.; Brezesinski, T.; Rathousky, J.; Feldhoff, A.; Oekermann, T.; Wark, M.; Smarsly, B. Transparent Conducting Films of Indium Tin Oxide with 3D Mesopore Architecture Adv. Mater. **2006**, 18, 2980-2983.

2. Muller, V.; Rasp, M.; Stefanic, G.; Ba, J. H.; Gunther, S.; Rathousky, J.; Niederberger, M.; Fattakhova-Rohlfing, D. Transparent Conducting Films of Antimony-Doped Tin Oxide with Uniform Mesostructure Assembled from Preformed Nanocrystals. Chem. Mater. **2009**, 21, 5229-5236.

3. Hou, K.; Puzzo, D.; Helander, M. G.; Lo, S. S.; Bonifacio, L. D.; Wang, W. D.; Lu, Z. H.; Scholes, G. D.; Ozin, G. A. Dye-Anchored Mesoporous Antimony-Doped Tin Oxide Electrochemiluminescence Cell. Adv. Mater. **2009**, 21, 2492–2496.

4. Chopra, K. L.; Major, S.; Pandya, D. K. Transparent Conductors - a Status Review. Thin Solid Films **1983**, 102, 1-46.

5. Wang, Y. D.; Brezesinski, T.; Antonietti, M.; Smarsly, B. Ordered Mesoporous Sb-, Nb-, and Ta-Doped SnO_2 Thin Films with Adjustable Doping Levels and High Electrical Conductivity. Acs Nano **2009**, 3, 1373-1378.

6. Furubayashi, Y.; Hitosugi, T.; Yamamoto, Y.; Inaba, K.; Kinoda, G.; Hirose, Y.; Shimada, T.; Hasegawa, T. A TransparentMetal: Nb-doped Anatase TiO_2. Appl. Phys. Lett. **2005**, 86, 252101-3.

7. Emeline, A. V.; Furubayashi, Y.; Zhang, X. T.; Jin, M.; Murakami, T.; Fujishima, A. Photoelectrochemical Behavior of Nb-doped TiO_2 Electrodes. J. Phys. Chem. B **2005**, 109, 24441-24444.

8. Hitosugi, T.; Kamisaka, H.; Yamashita, K.; Nogawa, H.; Furubayashi, Y.; Nakao, S.; Yamada, N.; Chikamatsu, A.; Kumigashira, H.; Oshima, M.; Hirose, Y.; Shimada, T.; Hasegawa, T. Electronic Band Structure of Transparent Conductor: Nb-Doped Anatase TiO_2. Appl. Phys. Expr. **2008**, 1, 111203

9. Lu, X. J.; Mou, X. L.; Wu, J. J.; Zhang, D. W.; Zhang, L. L.; Huang, F. Q.; Xu, F. F.; Huang, S. M. Improved-Performance Dye-Sensitized Solar Cells Using Nb-Doped TiO_2 Electrodes: Efficient Electron Injection and Transfer. Adv. Funct. Mater. **2010**, 20, 509-515.

10. Dros, A. B.; Grosso, D.; Boissiere, C.; Soler-Lia, G.; Albouy, P. A.; Amenitsch, H.; Sanchez, C. Niobia-Stabilised Anatase TiO_2 Highly Porous Mesostructured Thin Films. Micropor. Mesopor. Mater. **2006**, 94, 208-213.

11. Hirano, M.; Matsushima, K. Photoactive and Adsorptive Niobium-Doped Anatase (TiO_2) Nanoparticles: Influence of Hydrothermal Conditions on their Morphology, Structure, and Properties. J. Amer. Ceram. Soc. **2006**, 89, 110-117.

12. Mattsson, A.; Leideborg, M.; Larsson, K.; Westin, G.; Osterlund, L Adsorption and Solar Light Decomposition of Acetone on Anatase TiO_2 and Niobium Doped TiO_2 Thin Films. J. Phys. Chem. B **2006**, 110, 12101220.

13. Ruiz, A. M.; Dezanneau, G.; Arbiol, J.; Cornet, A.; Morante, J. R. Insights into the Structural and Chemical Modifications of Nb Additive on TiO_2 Nanoparticles. Chem. Mater. **2004**, 16, 862871.

14. Hasin, P.; Alpuche-Aviles, M. A.; Li, Y.; Wu, Y. Mesoporous Nb-Doped TiO_2 as Pt Support for Counter Electrode in Dye-Sensitized Solar Cells. J. Phys. Chem. C **2009**, 113, 7456-7460.

15. De Koninck, M.; Manseau, P.; Marsan, B. Preparation and Characterization of Nb-Doped TiO_2 Nanoparticles Used as a Conductive Support for Bifunctional $CuCo_2O_4$ Electrocatalyst. J. Electroanal. Chem. **2007**, 611, 67-79.

16. Furubayashi, Y.; Hitosugi, T.; Yamamoto, Y.; Hirose, Y.; Kinoda, G.; Inaba, K.; Shimada, T.; Hasegawa, T. Novel Transparent Conducting Oxide: Anatase Ti1-xNbxO_2. Thin Solid Films **2006**, 496, 157-159.

17. Furubayashi, Y.; Yamada, N.; Hirose, Y.; Yamamoto, Y.; Otani, M.; Hitosugi, T.; Shimada, T.; Hasegawa, T. Transport Properties of d-Electron-Based Transparent Conducting Oxide: Anatase Ti1-xNbxO_2. J. Appl. Phys. **2007**, 101, 212106-212108.

18. Haosugi, T.; Ueda, A.; Nakao, S.; Yamada, N.; Furubayashi, Y.; Hirose, Y.; Konuma, S.; Shimada, T.; Hasegawa, T. Transparent Conducting Properties of Anatase $Ti_{0.94}Nb_{0.06}O_2$ Polycrystalline Films on Glass Substrate. Thin Solid Films **2008**, 516, 5750-5753.

19. Hitosugi, T.; Ueda, A.; Furubayashi, Y.; Hirose, Y.; Konuma, S.; Shimada, T.; Hasegawa, T. Fabrication of TiO_2-Based Transparent Conducting Oxide Films on Glass by Pulsed Laser Deposition Japan. J. Appl. Phys. 2 **2007**, 46, L86-L88.

20. Hitosugi, T.; Ueda, A.; Nakao, S.; Yamada, N.; Furubayashi, Y.; Hirose, Y.; Shimada, T.; Hasegawa, T. Fabrication of Highly Conductive $Ti_{1-x}Nb_xO_2$ Polycrystalline Films on Glass Substrates via Crystallization of Amorphous Phase Grown by Pulsed Laser Deposition. Appl. Phys. Lett. **2007**, 90, 212106.

21. Neumann, B.; Bierau, F.; Johnson, B.; Kaufmann, C. A.; Ellmer, K.; Tributsch, H. Niobium-Doped TiO_2 Films as Window Layer for Chalcopyrite Solar Cells. Phys. Stat. Solidi B **2008**, 245, 1849-1857.

22. Yamada, N.; Hitosugi, T.; Hoang, N. L. H.; Furubayashi, Y.; Hirose, Y.; Konuma, S.; Shimada, T.; Hasegawa, T. Structural, Electrical and Optical Properties of Sputter-Deposited Nb-doped TiO_2 (TNO) Polycrystalline Films. Thin Solid Films **2008**, 516, 5754-5757.

23. Zhang, S. X.; Kundaliya, D. C.; Yu, W.; Dhar, S.; Young, S. Y.; Salamanca-Riba, L. G.; Ogale, S. B.; Vispute, R. D.; Venkatesan, T. Niobium Doped TiO_2: Intrinsic Transparent Metallic Anatase Versus Highly Resistive Rutile Phase. J. Appl. Phys. **2007**, 102, 013701.

24. Zhang, S. X.; Dhar, S.; Yu, W.; Xu, H.; Ogale, S. B.; Venkatesan, T. Growth Parameter-Property Phase Diagram for Pulsed Laser Deposited Transparent Oxide Conductor Anatase Nb : TiO_2. Appl. Phys. Lett. **2007**, 91, 112113.

25. Noh, J. H.; Lee, S.; Kim, J. Y.; Lee, J. K.; Han, H. S.; Cho, C. M.; Cho, I. S.; Jung, H. S.; Hong, K. S. Functional Multilayered Transparent Conducting Oxide Thin Films for Photovoltaic Devices. J. Phys. Chem. C **2009**, 113, 1083-1087.

26. Morris, D.; Dou, Y.; Rebane, J.; Mitchell, C. E. J.; Egdell, R. G.; Law, D. S. L.; Vittadini, A.; Casarin, M. Photoemission and STM Study of the Electronic Structure of Nb-Doped TiO_2. Phys. Rev. B **2000**, 61, 13445-13457.

27. Sheppard, L.; Bak, T.; Nowotny, J.; Sorrell, C. C.; Kumar, S.; Gerson, A. R.; Barnes, M. C.; Ball, C. Effect of Niobium on the Structure of Titanium Dioxide Thin Films. Thin Solid Films **2006**, 510, 119-124.

28. Sheppard, L. R.; Bak, T.; Nowotny, J. Electrical Properties of Niobium-Doped Titanium Dioxide. 1. Defect Disorder. J. Phys. Chem. B **2006**, 110, 22447-22454.

29. Sheppard, L. R.; Bak, T.; Nowotny, J. Electrical Properties of Niobium-Doped Titanium Dioxide. 2. Equilibration Kinetics. J. Phys. Chem. B **2006**, 110, 22455-22461.

30. Grosso, D.; Soler-Illia, G.; Babonneau, F.; Sanchez, C.; Albouy, P. A.; Brunet-Bruneau, A.; Balkenende, A. R. Highly Organized Mesoporous Titania Thin Films Showing Mono-Oriented 2D Hexagonal Channels. Adv. Mater. **2001**, 13, 10851090.

31. Hwang, Y. K.; Lee, K. C.; Kwon, Y. U. Nanoparticle Routes to Mesoporous Titania Thin Films. Chem. Comm. **2001**, 17381739.

32. Szeifert, J. M.; Fattakhova-Rohlfing, D.; Georgiadou, D.; Kalousek, V.; Rathousky, J.; Kuang, D.; Wenger, S.; Zakeeruddin, S. M.; Gratzel, M.; Bein, T. "Brick and Mortar" Strategy for the Formation of Highly Crystalline Mesoporous Titania Films from Nanocrystalline Building Blocks. Chem. Mater. **2009**, 21, 1260-1265.

33. Müller, V.; Rasp, M.; Rathouský, J.; Schütz, B.; Niederberger, M.; Fattakhova-Rohlfing, D. Transparent Conducting Films of Antimony-Doped Tin Oxide with Uniform Mesostructure Assembled from Preformed Nanocrystals. Small **2010**, 6, 633-637.

34. Szeifert, J. M.; Feckl, J. M.; Fattakhova-Rohlfing, D.; Liu, Y.; Kalousek, V.; Rathousky, J.; Bein, T. J. Amer. Chem. Soc. **2010**, 132, 12605-12611.

35. Arbiol, J.; Cerda, J.; Dezanneau, G.; Cirera, A.; Peiro, F.; Cornet, A.; Morante, J. R. Effects of Nb Doping on the TiO_2 Anatase-to-Rutile Phase Transition. J. Appl. Phys. **2002**, 92, 853-861.

36. Di Valentin, C.; Pacchioni, G.; Selloni, A. Reduced and n-Type Doped TiO_2: Nature of Ti^{3+} Species. J. Phys. Chem. C **2009**, 113, 20543-20552.

37. Atashbar, M. Z.; Sun, H. T.; Gong, B.; Wlodarski, W.; Lamb, R. XPS Study of Nb-Doped Oxygen Sensing TiO_2 Thin Films Prepared by Sol-Gel Method. Thin Solid Films **1998**, 326, 238-244.

38. Dacca, A.; Gemme, G.; Mattera, L.; Parodi, R. XPS Analysis of the Surface Composition of Niobium for Superconducting RF Cavities. Appl. Surf. Sci. **1998**, 126, 219-230.

39. Kubacka, A.; Colon, G.; Fernandez-Garcia, M. Cationic (V, Mo, Nb, W) Doping of TiO_2-Anatase: A Real Alternative for Visible Light-Driven Photocatalysts. Catal. Today **2009**, 143, 286-292.

40. Hitosugi, T.; Kinoda, G.; Yamamoto, Y.; Furubayashi, Y.; Inaba, K.; Hirose, Y.; Nakajima, K.; Chikyow, T.; Shimada, T.; Hasegawa, T. Carrier Induced Ferromagnetism in Nb Doped Co : TiO_2 and Fe : TiO_2 Epitaxial Thin Film. J. Appl. Phys. **2006**, 99, 08M121.

41. Niederberger, M. Nonaqueous Sol-Gel Routes to Metal Oxide Nanoparticles. Acc. Chem. Res. **2007**, 40, 793-800.

42. Zunger, A. Practical Doping Principles. Appl. Phys. Letters **2003**, 83, 57-59.

43. Norris, D. J.; Efros, A. L.; Erwin, S. C. Doped Nanocrystals. Science **2008**, 319, 1776-1779.

44. Mikulec, F. V.; Kuno, M.; Bennati, M.; Hall, D. A.; Griffin, R. G.; Bawendi, M. G. Organometallic Synthesis and Spectroscopic Characterization of Manganese-Doped CdSe Nanocrystals. J. Amer. Chem. Soc. **2000**, 122, 2532-2540.

45. Grosso, D.; Boissiere, C.; Smarsly, B.; Brezesinski, T.; Pinna, N.; Albouy, P. A.; Amenitsch, H.; Antonietti, M.; Sanchez, C. Periodically Ordered Nanoscale Islands and Mesoporous Films Composed of Nanocrystalline Multimetallic Oxides. Nat. Mater. **2004**, 3, 787-792.

Chapter 4

Tuning the conduction mechanism in Nb-doped titania nanoparticle networks

This chapter is based on the collaborated project and the results were published in the following publication:

Hynek Němec, Zoltán Mics, Martin Kempa, and Petr Kužel, Oliver Hayden, Yujing Liu, Thomas Bein, Dina Fattakhova-Rohlfing. J. Phys. Chem. C 2011, 115, 6968–6974

4.1. Introduction

Nanoscaling and nanopatterning introduce additional functional properties to existing materials which opens a way to the conception of novel devices and techniques. For example, fabrication of transparent conducting oxides in the form of nanoparticles can significantly enrich the scope of the available materials in addition to dense films, enabling manufacturing of conducting composites, nanostructured transparent electrodes or low-temperature printing of patterned electrodes. However, the decrease of the grain dimensions to the nanoscale increases the role of the surface, which dramatically alters the dielectric properties and electron transport in the nanoparticle-based materials. The measured macroscopic conductivity in a sample composed of assembled nanosized particles is influenced (besides the intrinsic bulk properties of the material) by several factors such as electron confinement effects, the energy of surface states, the difference in surface and core composition of nanoparticles, the electron scattering on surface defects and on grain boundaries, and the connectivity of nanoparticles in the sample, just to name a few. The ability to resolve and characterize the individual factors controlling the total macroscopic conductivity is of extreme importance for the optimization of charge carrier transport properties in nanoscaled materials.

Many of these factors can be elucidated through the electromagnetic response measured in a broad frequency range. A very pertinent spectral domain for the investigation of nanoscaled materials is the terahertz (THz) range. First of all, different conductivity mechanisms lead to qualitatively different conductivity spectra in the THz region, and it is straightforward to distinguish between the response of delocalized electrons (described, e.g., by the Drude formula) and electrons localized in potential wells [1,2]. The electron confinement strongly affects the conductivity spectra if the particle size is comparable to or smaller than the electron diffusion length l_D on the timescale of one period of the probing radiation ($l_D \approx \sqrt{D/f}$, where D is the diffusion coefficient and f is the probing frequency). THz frequencies are thus optimal for the investigation of electron transport within and among nanometer-sized particles of common semiconductors [3]. Finally, the measured conductivity spectra reflect the distribution of depolarization fields, which are inherently related to the morphology of the nanomaterial [4,5].

In this sense, the THz spectral region contains rich information about nanoscaled systems covering conductivity mechanisms, carrier confinement and material morphology [6]. However, full quantitative interpretation of the conductivity spectra requires the development of a microscopic theoretical framework able to describe all the above-mentioned phenomena. Despite the great potential of THz spectroscopy in the field of nanoscaled materials, such an approach has been seldom applied up to now (see [4] and references therein).

Niobium-doped titanium dioxide (NTO) is a novel class of transparent conductors, which is considered as a cheap and chemically stable alternative to indium tin oxide [7]. Recently, we described a low-temperature synthesis approach for the fabrication of monosized dispersible crystalline NTO particles of just a few nanometers in size with different Nb contents, which can be assembled into mesoporous films with periodic porous architectures [8]. We observed that the Nb doping of the titania lattice leads to the introduction of donor levels into TiO_2, detectable as the reduced states of the Ti and Nb, and to a drastic increase in the electrical dc conductivity. Its dependence on the Nb doping level in the nanoparticles is, however, different from that in bulk materials fabricated by physical methods such as pulsed laser deposition or high-temperature solid state synthesis, and it is strongly influenced by the synthesis temperature and heat treatment conditions. In order to understand the conductivity mechanisms in this system it is important to identify the different contributions to the conductivity by measurements over a broad range of frequencies. The resulting understanding of the conductivity mechanism can be helpful for the characterization of other nanoscale semiconducting materials.

In this paper, we employ time-domain terahertz spectroscopy and microwave impedance spectroscopy to measure the conductivity and permittivity spectra in the terahertz and gigahertz spectral regions for a set of pellets of Nb-doped anatase nanoparticles with variable doping concentrations. We develop a detailed physical framework for the interpretation of the conductivity spectra where we establish the relation between depolarization fields and sample morphology, characterize the electron confinement, and identify the relevant conductivity mechanisms.

4.2. Experimental Results

TiO_2 nanoparticles were prepared by a non-aqueous synthesis at 60–150 ℃ via solvothermal procedures using tert-butanol as a reaction medium with three Nb doping levels (0 mol%, 10 mol% and 20 mol%): for details see [8]. Pellets were formed by pressing the nanoparticles under a pressure of 10 MPa with the sample holder of 13 mm in diameter; their thickness ranged from 0.55 to 1.28 mm. Pellets were studied as-prepared and annealed at 600 ℃ in nitrogen atmosphere to prevent oxidation and water vapor adsorption.

The elaboration procedure enables preparation of non-agglomerated nanoparticles, whose size and crystallinity can be controlled by the reaction temperature and time. At 60^oC completely amorphous particles are obtained. An increase of the reaction temperature to 100^oC leads to the formation of ~4 nm crystalline nanoparticles with a phase structurally related to anatase, which can incorporate more than 20 mol% of Nb ions without significant distortion of the anatase lattice or phase separation. The introduction of Nb in the anatase increases the dc conductivity by several orders of magnitude [8]. The dc conductivity of the pellets pressed from the particles prepared at 100^oC is 1×10^{-6} S/cm for undoped and 2×10^{-5} S/cm for the 20% doped nanoparticles. Heating of the as-produced NTO nanoparticles at 600^oC in nitrogen atmosphere further improves the dc electrical conductivity, which increases up to 0.25 S/cm for the 20% Nb sample. The onset of the dc conductivity in the Nb-doped particles is supported by an observation of reduced states of both titanium and niobium, Ti^{3+} and Nb^{4+} or lower, by x-ray photoelectron spectroscopy (XPS). The presence of these states in both as-prepared and heated particles enabled us to suggest that most of the extra electrons generated by Nb doping are released into the conduction band of TiO_2, leading to the formation of Ti^{3+} and resulting in the electrical conductivity [8].

To evaluate the role of Nb doping in the conductivity at THz frequencies we selected a set of nanoparticles synthesized in the same reaction conditions, namely at 100^oC, and with the Nb content varying from 0% to 20% (denoted further as NTO-X%@100^oC). The particles prepared in this way are crystalline, of about 4 nm diameter. Additionally, in order to investigate the role of crystallization conditions in the conductivity of the samples prepared from different types of particles, we prepared the NTO particles with a single doping level of 20 mol% but at different synthesis temperatures, 60^{o}C and 150^{o}C, (denoted further as NTO_20%@60^{o}C and NTO_20%@150^{o}C), which leads to the formation of amorphous and completely crystalline particles, respectivity. The particles were pressed into pellets and studied as-prepared and after heating in nitrogen at 600^{o}C.

The permittivity and conductivity at terahertz frequencies were measured using time-domain THz transmission spectroscopy [9]. The useful bandwidth in our custom-made setup, based on a femtosecond laser oscillator, spans from 0.1 to 3 THz [10]. The permittivity and conductivity spectra were retrieved from the directly measured transmittance spectra of THz radiation (i.e., in a non-contact fashion). These results are free of systematic errors related to electrodes and they are also very accurate [9, 10, 11]. The method provides the dielectric permittivity averaged over the entire thickness of the sample.

The impedance at microwave frequencies (20 MHz – 10 GHz) was measured using an open-end coaxial technique (Agilent 85070E dielectric probe) with an Agilent E8364B network analyzer. The drawback of this technique is the difficult control of the quality of the contact between the probe and the sample. Our samples are very rigid and their surface is rather rough. Under these conditions, it is rather difficult to obtain a good electrical contact. In fact, most of the measured microwave permittivities are lower than the THz permittivity which indicates that an air gap or dead layer was formed between the sample and the end of the probe. As a result, measurements of the microwave permittivity provide a good indication of the trends in the permittivity spectra, but the data are not accurate enough to be used for a common fitting with the THz data.

The permittivity spectra measured by microwave and THz spectroscopy are summarized in Figures 4.1 and 4.2. All the samples exhibit qualitatively similar behavior. At microwave frequencies, both the real and the imaginary part of the permittivity decreases with increasing frequency. This behavior is characteristic for a broadband dielectric relaxation. In principle, such a relaxation could originate from lattice dynamics. However, the lattice response of anatase is dominated by phonon modes and no relaxation is observed in bulk crystals [12]. We thus attribute the observed broadband response to an electron hopping with a wide distribution of hopping times [13].

For as-prepared particles with different Nb doping levels, the real part decreases continuously up to 0.4 – 1 THz, whereas at higher frequencies it starts to increase. Similar but less-pronounced trends are observed in the spectra of annealed samples (note that the accessible spectral range is narrower due to stronger absorption). The imaginary part of the permittivity increases with frequency in the THz region in all samples. The decreasing real part is the tail of the broadband response due to the hopping conduction. The slight parabolic increase in the real part accompanied by the almost linearly increasing imaginary part is naturally explained as the onset of the phonon contribution to this part of the spectrum [12].

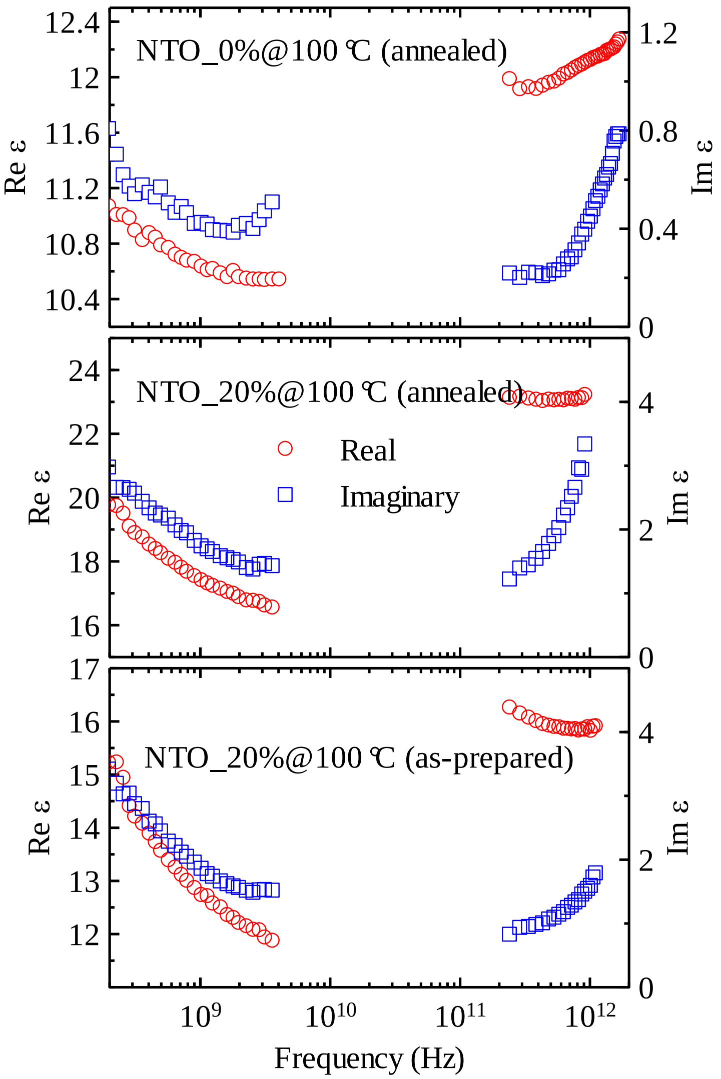

Figure 4.1 Measured real (red circles) and imaginary part (blue squares) of the permittivity of selected samples. The GHz spectra were measured by the microwave impedance analyzer whereas the THz spectra were measured by time-domain THz spectroscopy.

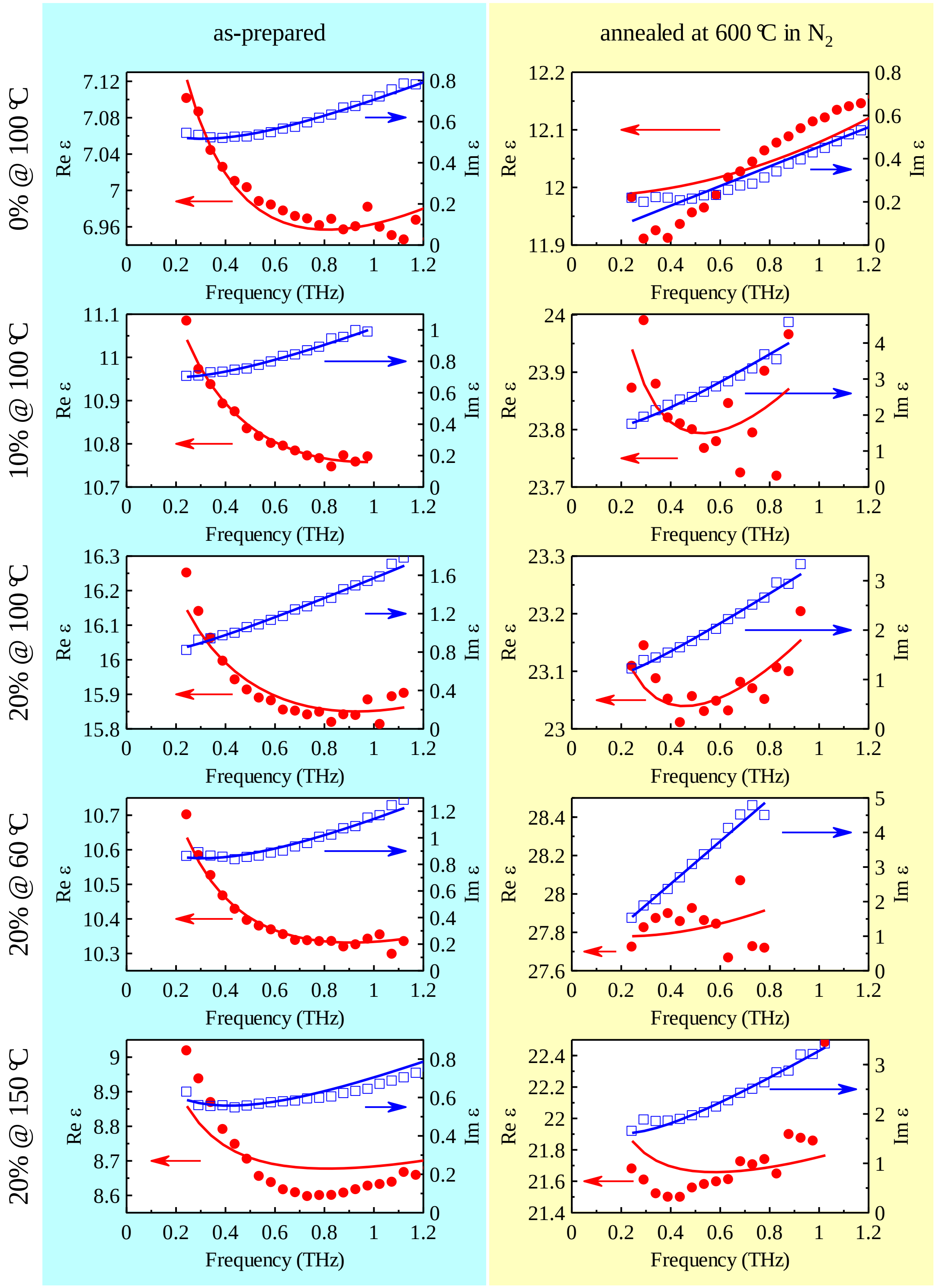

Figure 4.2 Permittivity in the THz spectral range. Symbols: measurement by time-domain THz spectroscopy, lines: fit by Equation 4.2. The red circles correspond to the real part and the blue squares represent the imaginary part of the permittivity.

4.3. Model of the dielectric function

Based on these considerations, we developed a model of the dielectric permittivity that allows us to get a more detailed qualitative and quantitative understanding of the observed response in all samples. This model takes into account factors that may influence the total conductivity of the particles pressed into pellets, namely: (i) permittivity and conductivity of individual particles, and (ii) inhomogeneous nature of the pellets.

(i) Permittivity of individual particles.

The response of the doped titania consists of lattice and electron contributions. As we have pointed out above, the former is related to a polar phonon mode whereas electron hopping dominates the latter contribution.

Anatase is a uniaxial crystal with static relative permittivities $\varepsilon_{a,0} = 22.7$ and $\varepsilon_{c,0} = 45.1$ for the electric field polarized perpendicularly to and along the optical axis, respectively, and with different phonon modes in polarized infrared spectra for these two polarizations [12]. For simplicity, we approximate the permittivity of anatase as the weighted average of the diagonal tensor elements: $\varepsilon_{\text{anatase}} = \frac{2\varepsilon_a}{3} + \frac{\varepsilon_c}{3}$. The static average relative permittivity of anatase is then $\varepsilon_{\text{anatase},0} = 37.6$.

For the hopping conductivity, we employ the Dyre's random free-energy model [14]

$$\sigma_{\text{hopping}}(f) = 2\pi i f \cdot \sigma_\infty \cdot \left[1 - \frac{\ln \frac{\tau_{\min}}{\tau_{\max}}}{\ln \frac{1 - 2\pi i f \tau_{\min}}{1 - 2\pi i f \tau_{\max}}} \right] \cdot \frac{\ln \frac{\tau_{\max}}{\tau_{\min}}}{\frac{1}{\tau_{\min}} - \frac{1}{\tau_{\max}}} \qquad \text{Equation 4.1}$$

which does not exhibit the conductivity divergence encountered, e.g., in a power-law ($\sigma \propto \omega^s$) model. The spectrum of the hopping conductivity (Equation 4.1) is sketched in Figure 4.3. At frequencies well above the electron hopping rate $1/\tau_{\mathrm{min}}$, the conductivity approaches a constant value of σ_∞ which we will call a "saturated conductivity" in the subsequent discussion. The time τ_{max} represents the longest waiting time found in the system and it delimits the range of dispersion at low frequencies – the conductivity is constant and low below $1/\tau_{\mathrm{max}}$. The dc conductivity [$\sigma_{\mathrm{hopping}}(0)$] decreases with increasing τ_{max}.

The total permittivity of the conducting nanoparticles reflecting both the lattice and the electron contribution then reads $\varepsilon = \varepsilon_{\mathrm{anatase}} + i\sigma_{\mathrm{hopping}}/(2\pi f\varepsilon_0)$.

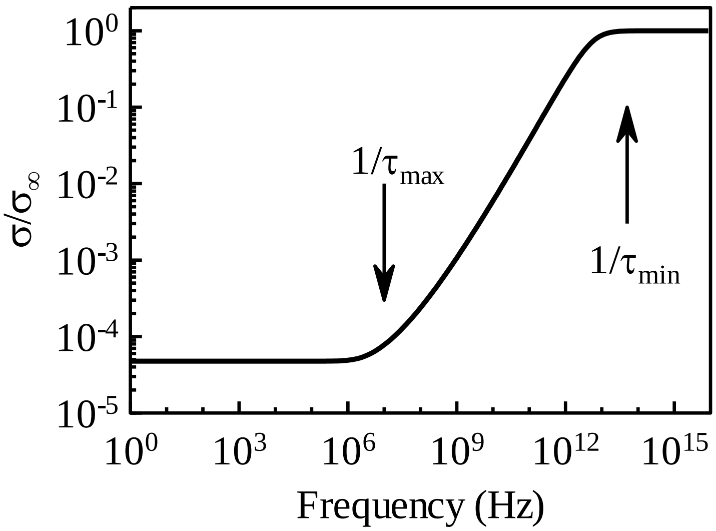

Figure 4.3 Sketch of the real part of hopping conductivity defined by Equation 4.1 [τmin = 20 fs, τmax = 100 ns]. Note that both scales are logarithmic.

(ii) Permittivity of the pellets.

A substantial complication in the analysis of the measured permittivity is imposed by the inhomogeneous nature of the pellets which gives rise to depolarization fields [5]. Since the nanoparticles are much smaller than the wavelength of the incident radiation, we use an effective medium approximation that yields a relation between the permittivity of nanoparticles and the effective (measured) permittivity of the samples. The effective medium approximation should account for the broad range of the observed permittivities: these span from ~7.0 for the as-prepared NTO_0%@100 ^{o}C sample to ~27.8 for the annealed NTO_20%@60^{o}C sample (Figure 4. 2). Different dilutions of anatase nanoparticles cannot be responsible for this large difference, since the mass densities of all pellets are roughly comparable to each other. The observed differences in permittivities thus necessarily originate from different degrees of dielectric percolation of nanoparticles. For example, the permittivity value of the annealed sample NTO_20%@60^{o}C is quite close to the average permittivity of the anatase (ca. 37.6), which shows that a significant fraction of the titania is percolated in this sample. Conversely, the low permittivity observed in the undoped crystalline sample NTO_0%@100^{o}C indicates that the titania is not percolated: individual titania nanoparticles are isolated from each other by the low-permittivity organic shell or by a low-permittivity dead layer. In order to account for both these extreme cases, we express the effective permittivity ε_{eff} as a sum of these two contributions, which is analogous to a parallel connection of two capacitors (Figure 4. 4) [15]:

$$\varepsilon_{\text{eff}} = s_{\text{p}}\varepsilon_{\text{percolated}} + (1 - s_{\text{p}})\varepsilon_{\text{non-percolated}}. \qquad \text{Equation 4.2}$$

Here $\varepsilon_{\text{percolated}} = \varepsilon$ is the permittivity of the percolated part, which is equal to the permittivity of the anatase nanoparticles ε, and s_{p} is the volume fraction of the percolated part. The permittivity of the non-percolated part is calculated within the Maxwell-Garnett model which assumes no dielectric connectivity between the nanoparticles:

$$\varepsilon_{\text{non-percolated}} = \frac{\varepsilon(1 + 2s_{\text{n}}) + 2(1 - s_{\text{n}})}{\varepsilon(1 - s_{\text{n}}) + (s_{\text{n}} + 2)} \qquad \text{Equation 4.3}$$

The non-percolated titania nanoparticles are assumed to occupy a volume fraction $s_n = 0.65$ (tightly-packed spheres) whereas the rest of the space is occupied by a material with the permittivity close to 1 (air pores, residual organic parts). It should be noted that the permittivity ε is frequency dependent; Equation 4.3 then implies that its shape generally differs from the spectrum of the effective permittivity ε_{eff} [4].

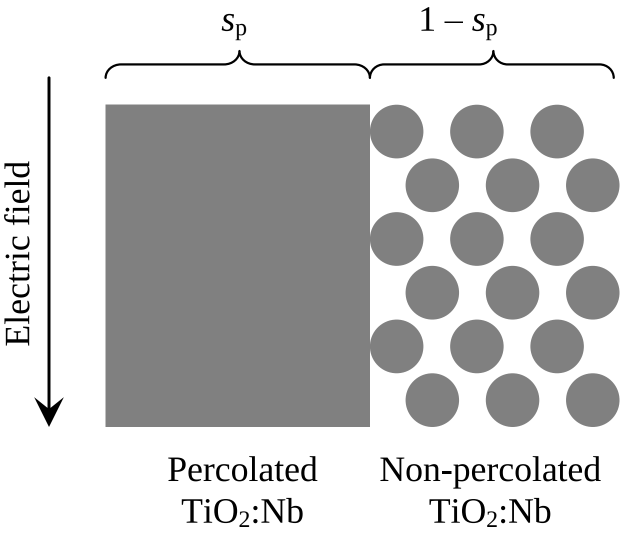

Figure 4.4 Scheme of the structure proposed to account for the depolarization fields.

4.4. Discussion

For fitting of the experimental spectra in the THz range, the model described by Equation 4.2 was used. The charge carrier hopping rate τ_{min} in Equation 4.1 was set to 20 fs, which corresponds to the phonon frequency [13], whereas τ_{max} was kept at 100 ns which is well below the available spectral window (this parameter has no influence on THz spectra). The model described by

Equation 4. 2 then contains only two adjustable parameters: s_p and σ_∞. However, the above model did not yield fully satisfactory results and it turned out to be necessary to enhance the anatase dielectric losses related to the phonon mode (Im $\varepsilon_{anatase}$) by a multiplication factor to obtain good fits – we shall refer to this factor as to the loss enhancement factor. This enhancement can be understood in terms of extrinsic dielectric losses [16].

The best fits of the THz permittivities by Equation 4.2 are shown in Figure 4. 2. The quality of the fits is very good for most of the non-annealed samples; moreover, extrapolation of the effective permittivity (Equation 4.2) to the microwave region yields a spectrum qualitatively agreeing with that measured by the open-end coaxial probe. The fit of the THz data is worse for the NTO_20%@150^{o}C sample, which is the only non-annealed sample composed of fully crystalline nanoparticles, and for some of the doped samples after annealing. It is then possible that, besides the hopping process, the band-like transport of electrons starts to significantly contribute to the terahertz conductivity (see discussion below).

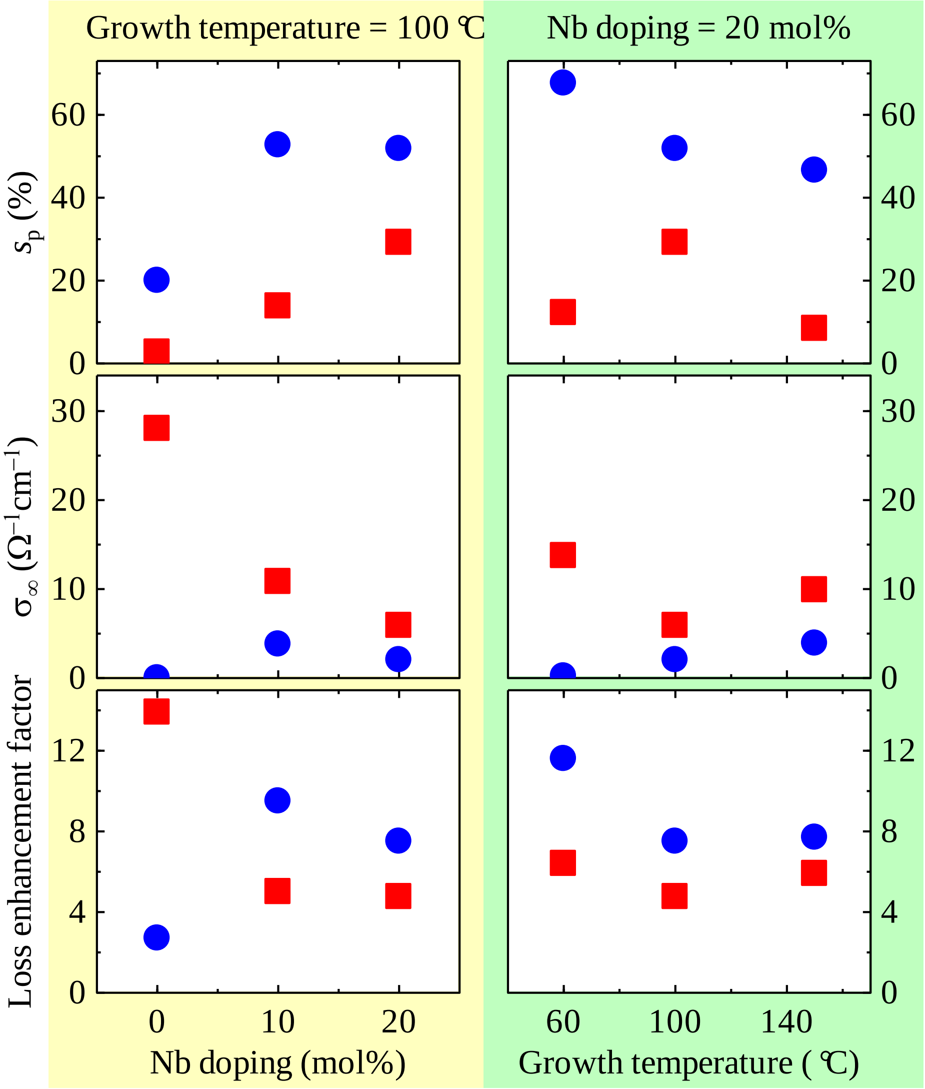

Figure 4.5 Results of the fits of the THz permittivity for the pellets pressed from nanoparticles with varying doping level synthesized at 100 oC (left column), and nanoparticles with the doping level of 20 % synthesized at several temperatures (right column). Squares: as-prepared samples, circles: annealed samples.

The fitting parameters are summarized in Figure 4. 5. The most pronounced trend is the increase of the percolated titania fraction s_p upon annealing. This is related to the sintering and maybe also to a further crystallization and crystal growth of titania nanoparticles. All the Nb-doped annealed samples exhibit a comparable level of the percolated fraction s_p. A significantly lower s_p is observed in the annealed undoped sample. This indicates that Nb-doping has a positive effect on nanoparticle sintering. Note that the real morphology of the samples may differ to a certain extent from that sketched in Figure 4. 4. As a result, trends in the percolated volume fraction s_p provide reliable information, but its absolute values as well as the absolute value of the total titania fraction $s_p + s_n(1 - s_p)$ should be taken with care.

The highest saturated conductivity σ_∞ is observed for the as-prepared undoped sample NTO_0%@100^{o}C, which, on the other hand, exhibits the lowest dc conductivity. This apparent contradiction can be explained in terms of Equation 4.1: this sample must contain a large density of localized states between which the electron hopping occurs with very long hopping times (high τ_{max}). Such assumptions are well justifiable in the as-prepared nanoparticles that probably contain a high density of defects: in this case the dc conductivity can be very low. Thermal annealing then removes defects which in turn may suppress the hopping conductivity. This is observed with the annealed undoped sample NTO_0%@100^{o}C where the hopping conductivity is almost zero (Figure 4. 5).

From the data plotted in Figure 4. 5 we see that the saturated hopping conductivity σ_∞ of all doped samples is lower than that of the as-prepared undoped pellet. The saturated hopping conductivity σ_∞ then decreases upon annealing, but it does not vanish. As in the case of the undoped samples, this indicates that a part of the hopping conductivity is related to the existence of defect states that disappear upon thermal annealing. The remaining portion is then induced by the Nb doping. The dc conductivity in the annealed samples is still much lower than the Nb-doping-induced hopping conductivity and it is strongly dependent on the doping density. This dependence can be explained through the variation of τ_{max} in Equation 4.1. With increasing doping density, the hopping distance decreases, the longest hopping time thus shortens and the dc conductivity is enhanced.

For completeness, we also studied the possible contribution of *delocalized* conduction band electrons. The conduction band electrons can interact with the nanoparticle surface, which decreases their mobility. The impact of the interaction on the conductivity spectra was studied in detail in Ref.[3] and we used the same model here in our calculations. The electrons exhibit a Brownian motion within nanoparticles given by isotropic scattering events in the bulk and, in addition, they can interact with the nanoparticle boundaries. In Figure 4. 6 we illustrate the conductivity spectra calculated for two extreme cases: (a) electrons are scattered by the nanoparticle boundary in a random direction, and (b) electrons cannot penetrate through the nanoparticle surface, i.e., they are confined within the nanoparticle. These spectra essentially differ from the measured ones (Figure 4. 2), which leads us to the conclusion that band conduction is not dominant at THz frequencies. More specifically, the density of delocalized electrons must be significantly lower than 3×10^{18} cm^{-3} used in Figure 4. 6. However, Hall effect measurements show that the electron density is much higher; for example, in the annealed samples with 20 mol% Nb doping it was ~10^{20} cm^{-3} [8]. This means that the vast majority of carriers contribute to the hopping conductivity which is the dominating contribution at THz frequencies. Note that it is not possible to resolve the contributions to the conductivity under the dc field: the longest hopping time τ_{max}, which determines the dc hopping conductivity, cannot be determined from the measurements, and we obtained only the upper limit of the density of delocalized electrons.

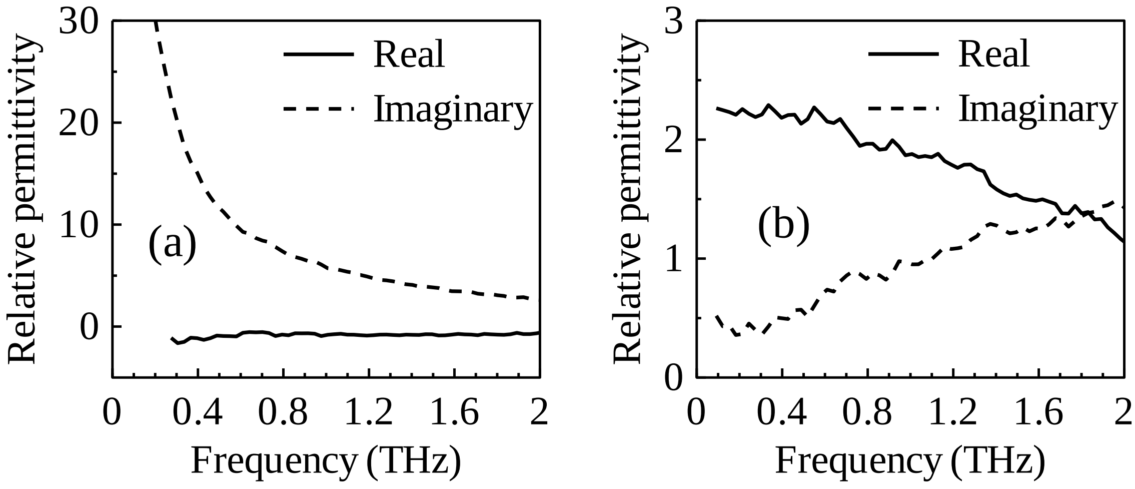

Figure 4.6 Calculated contribution of conduction-band electrons to the relative permittivity. Parameters: nanoparticle diameter 4.5 nm, electron effective mass 6me, carrier density 3×10^{18} cm^{-3}. (a) Nanoparticle boundaries randomly scatter the carriers. (b) Nanoparticle boundaries reflect the carriers, i.e., the carriers are localized within the nanoparticle.

The phonon-mode-related dielectric losses are most enhanced in the undoped non-annealed sample (Figure 4. 5), which is consistent with the hypothesis of a high defect density in this sample. On the other hand, the loss enhancement factor drops to ~3 upon annealing, which agrees with the improvement of the anatase crystallinity upon annealing. The loss enhancement factor for the doped samples is then ~5 before annealing and ~9 after annealing. This suggests that Nb doping leads to a lattice deformation both in as-prepared and in annealed samples and thus to the enhanced dielectric losses. These results show that dielectric losses in semiconductor nanoparticles are enhanced compared to the bulk material. It is not clear whether this is a size effect or an effect due to residual defects present even in the annealed samples.

The obtained results suggest that the doping with Nb in nanosized particles introduces a large amount of reduced states that are observed by XPS, but electrons in these states are rather localized and their dc mobility (not the THz one) is rather low. The electron transport in the doped samples is then determined to a significant extent by the hopping between the reduced states. This explains the fact that the dc conductivity increases significantly with the increasing Nb content and thus with increasing density of the introduced reduced states (which also implies reduction of distances between these states). The increase in the dc conductivity in our nanoparticles is observed at doping levels up to 20 % of Nb, which is much higher than the doping level of ~4 % in the bulk materials grown by physical methods or solid state high temperature synthesis [17,18,19] with a much more perfect and defect-free crystalline lattice. The strong localization of the reduced states also explains the low dc conductivity in as-prepared particles. Thermal annealing then decreases the lattice defect density, which leads to the improvement of the dc conductivity. On the other hand, electron transport still occurs by hopping and electron dc mobility is thus still much lower than that found in bulk anatase crystals.

4.5. Conclusion

Time-domain THz transmission spectroscopy and microwave impedance spectroscopy were used to investigate dielectric and conduction properties of undoped and Nb-doped TiO_2 mesoporous pellets in a wide frequency range (20 MHz – 1 THz). A model accounting for the inhomogeneous nature of the pellets was developed – it was shown that the percolation of the titania significantly increases upon annealing. The THz and microwave response of titania nanoparticles is dominated by charge hopping and by the tail of phonon modes. We conclude that the transport of a vast majority of electrons in the doped samples occurs by hopping (=low mobility) between the reduced states and not by the free electron motion in delocalized conduction band states (=high mobility). The dielectric losses of titania nanoparticles are higher than in bulk. Thermal annealing of doped samples reduces their high-frequency saturated hopping conductivity and their dielectric loss which point on lattice improvement upon annealing.

4.6. Chapter references

1. F. A. Hegmann, O. Ostroverkhova, and D. G. Cooke, in: Photophysics of Molecular Materials, Wiley-VCH, New York, 2006, pp. 367–428.

2. L. Fekete, P. Kužel, H. Němec, F. Kadlec, A. Dejneka, J. Stuchlík, and A. Fejfar, Ultrafast carrier dynamics in microcrystalline silicon probed by time-resolved terahertz spectroscopy, Phys. Rev. B **79**, 115306 (2009).

3. H. Němec, P. Kužel, and V. Sundström, Far-infrared response of free charge carriers localized in semiconductor nanoparticles, Phys. Rev. B **79**, 11 5309 (2009).

4. H. Němec, P. Kužel, and V. Sundström, Charge transport in nanostructured materials for solar energy conversion studied by time-resolved terahertz spectroscopy, J. Photochem. Photobiol. A **215**, 123 (2010).

5. E. Hendry, M. Koeberg, B. O'Regan, and M. Bonn, Local field effects on electron transport in nanostructured TiO_2 revealed by terahertz spectroscopy, Nano Lett. **6**, 755 (2006).

6. H. Němec, P. Kužel, F. Kadlec, D. Fattakhova-Rohlfing, J. Szeifert, T. Bein, V. Kalousek, and J. Rathouský, Ultrafast terahertz photoconductivity in nanocrystalline mesoporous TiO_2 films, Appl. Phys. Lett. **96**, 06 2103 (2010).

7. Y. Furubayashi, T. Hitosugi, Y. Yamamoto, K. Inaba, G. Kinoda, Y. Hirose, T. Shimada, and T. A. Hasegawa, A transparent metal: Nb-doped anatase TiO_2, Appl. Phys. Lett. **86**, 252101 (2005).

8. Y. Liu, J. M. Szeifert, J. M. Feckl, B. Mandlmeier, J. Rathouský, O. Hayden, D. Fattakhova-Rohlfing, and T. Bein, Niobium doped titania nanoparticles: synthesis, assembly into mesoporous films and electrical conductivity, ACS Nano, **4**, 5373 (2010).

9. G. Grüner, Millimeter and submillimeter wave spectroscopy of solids, Springer-Verlag, Berlin, Heidelberg (1998).

10. P. Kužel, H. Němec, F. Kadlec, and C. Kadlec, Gouy shift correction for highly accurate refractive index retrieval in time-domain terahertz spectroscopy, Opt. Exp. **18**, 15338 (2010).

11. L. Duvillaret, F. Garet, and J.-L. Coutaz, Highly precise determination of optical constants and sample thickness in terahertz time-domain spectroscopy, Appl. Opt. **38**, 409 (1999).

12. R. J. Gonzalez, R. Zallen, and H. Berger, Infrared reflectivity and lattice fundamentals in anatase TiO_2, Phys. Rev. B **55**, 7014 (1997).

13. S. R. Elliott, A.c. conduction in amorphous chalcogenide and pnictide semiconductors, Adv. Phys. **36**, 135 (1987).

14. J. C. Dyre, The random free-energy barrier model for ac conduction in disordered solids, J. Appl. Phys. **64**, 2456 (1988).

15. C. Kadlec, F. Kadlec, P. Kužel, K. Blary, and P. Mounaix, Materials with on-demand refractive indices in the terahertz range, Opt. Lett. **33**, 2275 (2008).

16. J. Petzelt and S. Kamba, Submillimetre and infrared response of microwave materials: extrapolation to microwave properties, Mater. Chem. Phys. **79**, 175 (2003).

17. Y. Furubayashi, N. Yamada, Y. Hirose, Y. Yamamoto, M. Otani, T. Hitosugi, T. Shimada,; T. Hasegawa, Transport Properties of d-Electron-Based Transparent Conducting Oxide: Anatase $Ti_{1-x}Nb_xO_2$. J. Appl. Phys. **101**, 212106 (2007).

18. T. Haosugi, A. Ueda, S. Nakao, N. Yamada, Y. Furubayashi, Y. Hirose, S. Konuma, T. Shimada, T. Hasegawa, Transparent Conducting Properties of Anatase $Ti_{0.94}Nb_{0.06}O_2$ Polycrystalline Films on Glass Substrate. Thin Solid Films **516**, 5750 (2008).

19. S. X. Zhang, D. C. Kundaliya, W. Yu, S. Dhar, S. Y. Young,; L. G. Salamanca-Riba, S. B. Ogale, R. D. Vispute, T. Venkatesan, Niobium Doped TiO_2: Intrinsic Transparent Metallic Anatase Versus Highly Resistive Rutile Phase. J. Appl. Phys. **102**, 013701 (2007).

Chapter 5

Nano-hydroxides as versatile primary units for the assembly of mesoporous indium tin oxide electrodes

This chapter is based on the following publication:

Yujing Liu, Goran Stefanic, Jiri Rathousky, Oliver Hayden, Thomas Bein, Dina Fattakhova-Rohlfing. Submitted to RSC Journal Chemical Science.

5.1. Introduction

The development of nanostructured electrode layers with defined morphology is an important challenge in modern electrochemistry, as it enables the controlled design of complex electrochemical systems. Transparent conducting oxides (TCOs) play a special role in electrochemistry, being used as transparent electrodes for optoelectrochemical and electrochromic applications as well as spectroelectrochemistry. TCOs such as doped indium, tin or zinc oxides have been known for a long time in the form of dense flat layers obtained by physical deposition methods such as magnetron sputtering, but only recently the fabrication of 3D-conducting TCO networks has been reported [1-6]. The growing interest in such 3D-electrode architectures is based on their large interface area enabling incorporation of large amounts of functional redox guests, with the electrical conductivity of the framework providing direct electronic access to the incorporated species, and their optical transparency allowing interactions with light.

An established strategy to produce TCO layers with a periodic porous nanostructure involves self-assembly of aggregated amphiphilic molecules acting as templates with molecular precursors for the metal oxide framework. A crucial issue here is the conversion of the self-assembled precursor species into a fully crystalline interconnected framework without significant perturbation of the mesostructure. For preparation of mesoporous indium tin oxide (ITO) - one of the most frequently used TCOs - a special type of molecular precursor, indium tin tris-tert-butoxide, has recently been developed [6,7]. The latter enables the formation of an amorphous tin-rich indium oxide network showing high conductivity even in the amorphous state [6,7]. When conventional molecular precursors such as indium acetylacetonate or indium trichloride are used, the formation of fully crystalline mesoporous ITO layers is possible only by using special amphiphilic polymers such as the KLE or PIB-PEO type with enhanced hydrophilic/hydrophobic contrast [1,5,8].

A promising strategy for the elaboration of mesoporous crystalline layers is the use of already crystalline nanoscale building blocks instead of molecular metal oxide precursors for the mesostructure assembly, which can even be achieved with commercially available templates [2,9-12]. However, the universality of this approach is restricted by the limited availability of suitable nanoparticles, which need to be only a few nanometers in size, dispersible at high concentrations without agglomeration, and compatible with the solutions of the template molecules. Although different protocols have been developed for the synthesis of crystalline ITO nanoparticles [13-15], they are either not small enough to be compatible with the size of the template micelles (the typical sizes reported in the literature are over 10 nm), and/or their dispersibility in polar solvents used for the self-assembly is too low.

Here we present an alternative strategy to form crystalline mesoporous ITO materials which is based on the initial formation of indium tin hydroxide nanoparticles, their assembly into periodic mesoscopic structures directed by an amphiphilic polymer, and a subsequent transformation to mesoporous indium tin oxide. Indium is known to form crystalline hydroxides that can be converted into crystalline indium oxides at very mild temperatures of 200 – 300 ℃ [16-18]. This attractive feature of indium hydroxides was recently explored by different authors and used for the fabrication of nanostructured indium oxide materials [16,18-20]. The utility of this approach for the formation of conducting tin-doped indium oxide nanostructures is much less explored, but several reports already demonstrate their great potential as building blocks for nanostructure assembly. Qiu et al [21] described the formation of indium tin hydroxide films with tunable rod-like morphology by deposition of in-situ formed hydroxide units. Kovtyukhova et al [22,23] applied electrochemically initiated hydrolysis for preparing indium tin hydroxide nanostructures, which could subsequently be transformed into ITO films without a significant change in morphology. However, practically all the reported strategies rely on the in-situ formation and assembly of primary hydroxide units. This limits the control over the morphology of the resulting nanostructure, as the assembly is strongly influenced by the reaction conditions such as type of synthesis, type of solvent, ionic composition and ionic strength of the reaction mixture. Typically, only sheet-like or rod-like morphologies can be obtained in such a way due to the preferential anisotropic stacking of the resulting building blocks.

As we demonstrate in this report, a more universal strategy towards the formation of desirable ITO nanostructures relies on the controlled self-assembly of ultra-small hydroxide nanoparticles. The fabrication of such particles has not yet been reported; existing approaches provide anisotropic needle-like or rod-like particles [24,25]. We have developed a new strategy for preparing nanosized, nearly spherical and highly dispersible nanoparticles of indium tin hydroxide, which can be assembled into regular mesoporous architectures featuring the large pore size directed by a commercially available Pluronic polymer. The assembled structures are easily transformed into conducting crystalline mesoporous ITO films by a mild heat treatment at 300 ℃. The resulting ITO layers can accommodate large amounts of redox-active molecules and serve as efficient conducting electrodes with a very high surface area. To our knowledge, this is the first report on the preparation of mesoporous ITO films from pre-formed nanocrystals using the commercially available Pluronic templates.

5.2. Results and discussion

5.2.1. Synthesis of indium tin hydroxide nanoparticles

Indium tin hydroxide nanoparticles (named 'nano-hydroxides' here) were prepared by a solvothermal reaction in ethylene glycol. Above 250 ℃, this reaction leads to indium tin oxide (ITO) nanocrystals 15 to 50 nm in size depending on the reaction conditions [13]. However, when the reaction temperature is decreased to 200 ℃, nanoparticles are formed that do not correspond to an ITO phase (see below). TEM images show that the nanoparticles have a slightly elongated shape of about 3.5 nm x 8 nm in size (Figure 5.1). No particles with other shape or size were detected, suggesting the presence of just one phase. Besides the individual particles, particle agglomerates are also observed in the TEM images, which result from drying of nanoparticles on the TEM grid during the TEM sample preparation. The nanoparticles are very hydrophilic and well-dispersible in water forming stable colloidal dispersions, which become more translucent with an increase in the particle content (Figure 5.2, inset a). Addition of a small amount of acetic acid turned the dispersions clear, probably due to the disintegration of loose aggregates of nanoparticles (Figure 5.2, inset b). Dynamic light scattering (DLS) analysis of these dispersions shows that the particles in solution are monodisperse with a hydrothermal diameter of about 8 nm and a narrow particle size distribution (Figure 5.2).

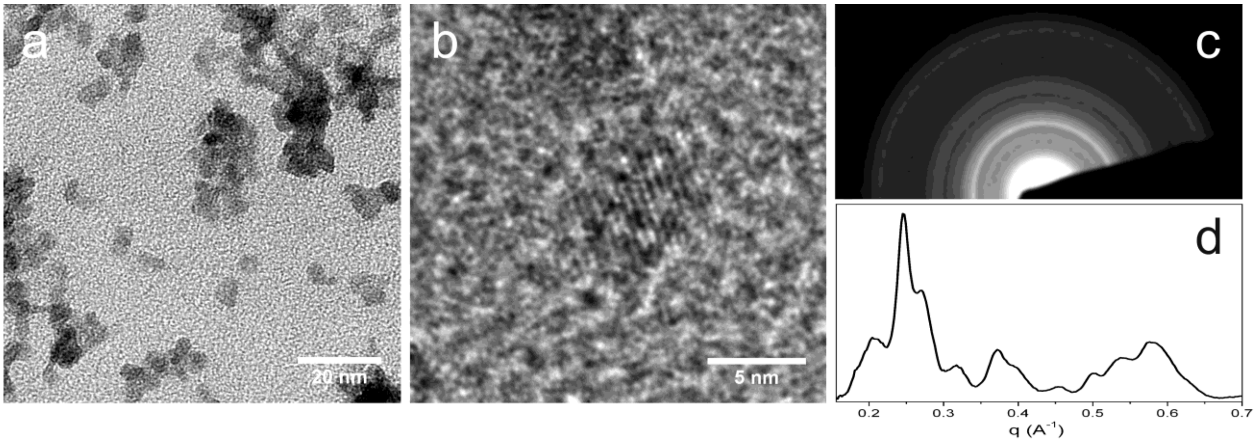

Figure 5.1 Morphology and crystallinity of as-produced indium tin hydroxide nanoparticles: TEM image of the dried particles (a), high resolution TEM image of a single nanoparticle (b), SAED pattern (c) and its corresponding intensity profile (d).

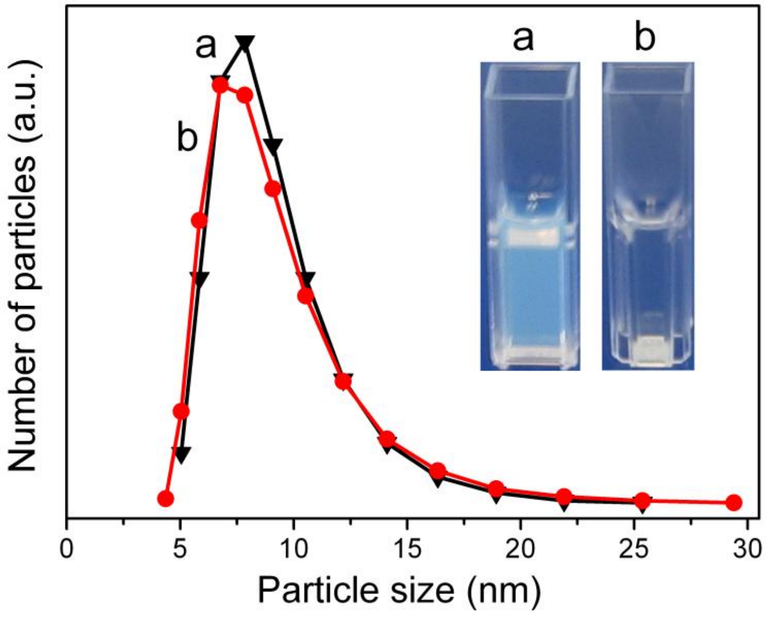

Figure 5.2 Dynamic light scattering (DLS) measurements of colloidal solutions of indium tin hydroxide nanoparticles in water: as-produced (black triangles, a) and after the addition of a few

drops of acetic acid (red circles, b). The inset shows the corresponding images of the colloidal solutions in water with a concentration of 8 wt% of nanoparticles.

Elemental analysis of the as-produced nanoparticles reveals that the atomic content of tin and indium is 10.5% and 89.5 % of the total metal content, respectively, which is very close to the synthesis mixture (10% and 90%, respectively). High resolution TEM images of single nanoparticles, electron diffraction patterns of a number of particles in TEM (Figure 5.1 b–d) and XRD patterns of the as-prepared dry particles (Figure 5.3a) demonstrate the crystallinity of the particles. The crystalline structure of the nanoparticles, however, neither corresponds to cubic ITO, nor can it be assigned to any known indium hydroxide, indium oxohydroxide or hydrated tin oxide phases. On the other hand, the observed diffraction pattern is very similar to that described by Qiu et al. [21] for tin-doped indium hydroxide films obtained by a hydrogen peroxide-assisted method, which they assigned to a yet unknown hexagonal tin-doped indium hydroxide phase with lattice parameters *a* and *c* equaling 10.89 and 3.99 Ǻ, respectively. We compared positions of the diffraction maxima calculated for this phase with those obtained for our particles (see Table AI1 and Figures AI1 and AI2 in Appendix I). Although the correct crystal lattice could not be determined with complete certainty due to the significant broadening and overlapping of diffraction lines, the results indicate that the crystalline phase of as-prepared indium tin hydroxide is structurally closely related to the hexagonal phase proposed by Qui et al. [21] (see Experimental Part for details). The line broadening (FWHM) values (Table AI1), estimated from the results of individual profile fitting, show that the diffraction lines at 2θ equaling 22.3 ° and 45.5 ° are much narrower than the other lines. Those two lines, which coincide with the diffraction lines 200 and 400 for cubic $In(OH)_3$ (JCPDS 76-1463), indicate the presence of size/strain anisotropy. The volume-averaged domain size (D_{hkl}) in the hkl direction corresponding to those two lines (direction 00l in the hexagonal lattice in Ref. 21) was roughly estimated, using the Scherrer equation, to be about 8 nm. Crystallite sizes in the perpendicular *hkl* directions are two to three times smaller (about 3 nm). The presence of size-anisotropy agrees with the results of HR-TEM analysis (Figure 5.1a), which shows crystallites appearing to be elongated in one direction.

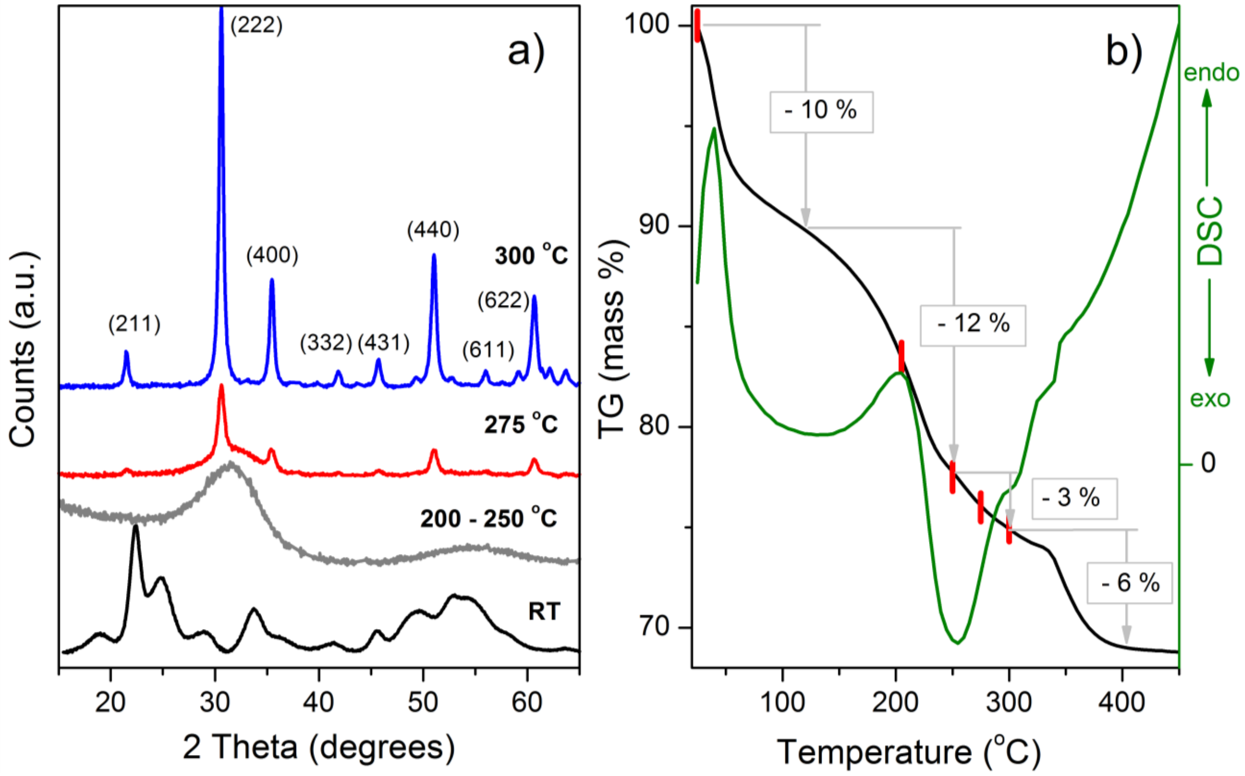

Figure 5.3 Monitoring the phase transformations of indium tin hydroxide nanoparticles at different temperatures: (a) XRD patterns and (b) thermogravimetric analysis (TG) (black curve) and differential scanning calorimetry (DSC) (green curve) of indium tin hydroxide nanoparticles. The XRD measurements were performed ex situ. For that, the as prepared indium tin hydroxide nanoparticles were heated at selected temperatures for 2 h (the red labels in Fig. 2b indicate the temperatures at which the samples were heated) and then characterized by XRD.

Thermal analysis of the as-prepared indium tin hydroxide nanocrystals shows two major mass losses in the temperature range of 25–300 °C. The first step of 10 wt% at 25–100 °C is attributed to the evaporation of molecular water and solvents in an endothermal process. The second endothermal mass decrease of ca. 12 % at 150 to 250 °C can be attributed to the loss of hydroxide groups or water of hydration. As follows from the XRD patterns, this step is accompanied by a transformation of the initially crystalline phase into an amorphous one. In a very narrow temperature range of 250–300 °C this amorphous phase crystallizes into a cubic one in an exothermal process with only small mass changes. At 275 °C, an onset of crystallization and the simultaneous presence of amorphous and crystalline ITO phases was observed. The transformation into cubic ITO was complete at 300 °C (Figure 5.3a). Further heating to 400 °C leads to particle sintering, as follows from some crystal domain growth from 23 nm at 300 °C (Figure 5.3a) to 28 nm at 400 °C (Figure 5.4) detected from the peak broadening in the XRD patterns, and which is accompanied by a loss of surface hydroxide groups (mass decrease of 6 wt %). No phase other than cubic bixbyite ITO was observed after calcination at 400 °C (Figure 5.4). Obviously, the as-produced crystalline indium tin hydroxide nanoparticles recrystallize into the cubic ITO phase at 275–300 °C, making them promising precursors for the low-temperature formation of ITO. Such kind of transformation is well documented for undoped as well as tin-doped indium hydroxides with different morphologies. It is the first time that the formation of an intermediate amorphous phase during this process was detected (see for comparison the reports on the phase transformations of macroscopic indium tin hydroxide – ITO systems) [16,26].

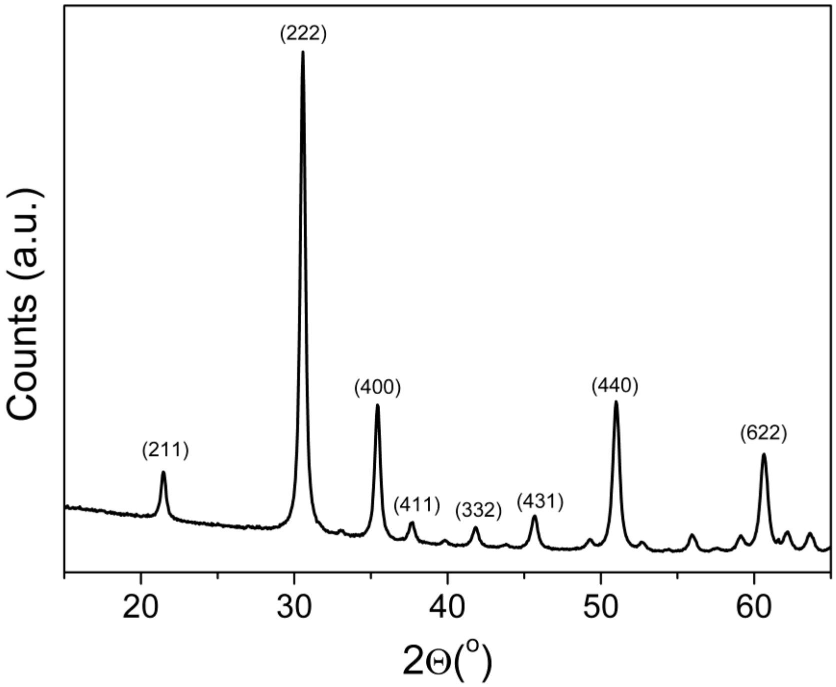

Figure 5.4 XRD pattern of indium tin hydroxide nanoparticles after calcination at 400 ℃ in air.

5.2.2. Self-assembly of pre-formed nano-hydroxides into mesoporous conducting ITO films

The properties of nano-hydroxides such as a small particle size, uniform size distribution, dispersibility without agglomeration, and facile transformation into crystalline ITO make them promising building blocks for the assembly of more complex porous 3D- structures in a template-assisted self-assembly process. Moreover, due to the hydrophilicity of the nano-hydroxides their preferential interaction with the hydrophilic part of the amphiphilic molecules can be expected, which should favor formation of periodic assemblies even for templates with a lower hydrophilic/hydrophobic contrast such as commercial block copolymers of the Pluronic family. In order to examine the ability of nano-hydroxides to self-assemble with surfactant templates, we added Pluronic F127 polymer to their colloidal dispersion in water and deposited the sols on various substrates by dip- or spin-coating. The resulting thin films are smooth, crack-free and homogeneous, and their thickness could be varied from a monolayer coating (ca. 20 nm) to 250 nm depending on the coating rate. The films were subsequently calcined first at 300 ℃ in air to remove the polymer and to transform the hydroxide to the ITO phase, and then in inert N_2 or reducing H_2/N_2 atmospheres at 300 to 500 ℃ to enhance the electrical conductivity of the obtained ITO framework. The results of Raman and X-ray photoelectron (XPS) spectroscopy confirm that the pore interface did not exhibit carbon-containing residues and that the polymer was completely removed (Figure 5.5).

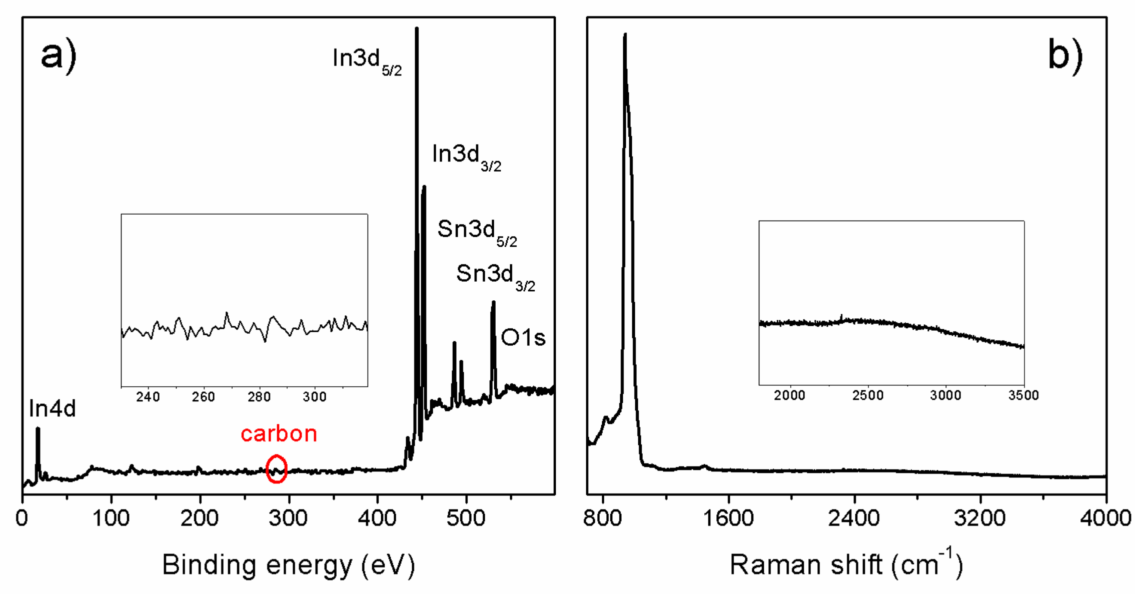

Figure 5.5 XPS (a) and Raman (b) spectra of the ITO films assembled from nano-hydroxides after calcination at 300 ℃ in air and heating at 300 ℃ in forming gas. The inset in (a) zooms in the energy region corresponding to carbon, indicating that no carbon residuals are present on the surface, and the inset in (b) zooms in the region between 1800 and 3500 cm-1 showing the absence of stretching vibrations of the aliphatic groups characteristic for Pluronic polymer.

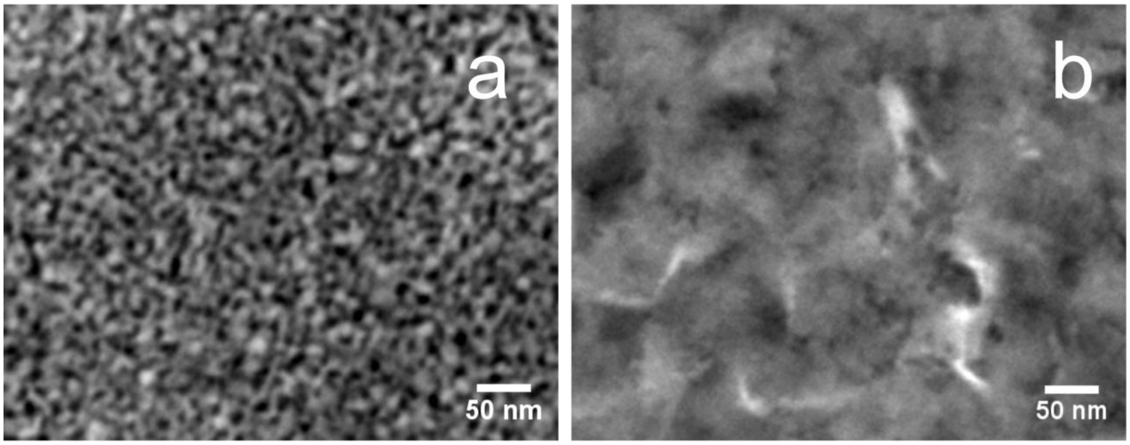

Figure 5.6 SEM images (top view) (a, b) of mesoporous ITO films assembled from nano-hydroxides (a) and from molecular precursors (In(III) and Sn(IV) chlorides in EtOH) (b) treated at 300 ℃ in air followed by a treatment at 300 ℃ in N_2/H_2.

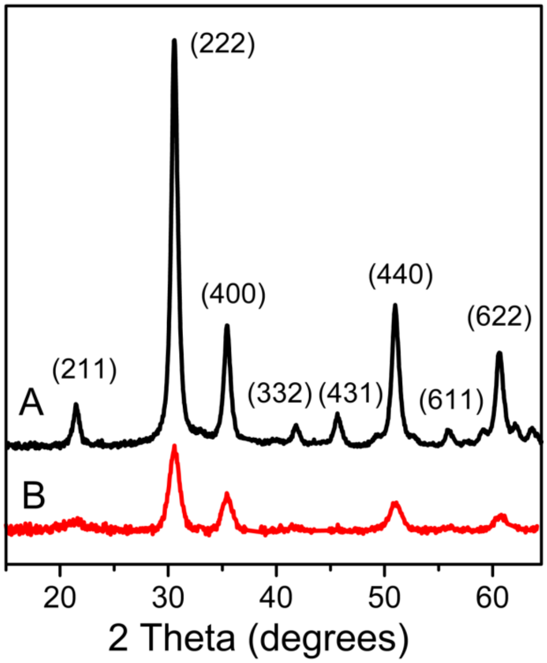

Figure 5.7 XRD patterns of mesoporous ITO films assembled from nano-hydroxides (A) and from molecular precursors (In(III) and Sn(IV) chlorides in EtOH) (B) treated at 300 ℃ in air followed by a treatment at 300 ℃ in N_2/H_2.

SEM images (Figure 5.6 (a)) demonstrate that the annealed films assembled from nano-hydroxides feature a regular highly porous morphology (i.e., all pores with the same size and shape), and some degree of pore ordering. The presence of repeating structural features is also detected by XRD, which shows a diffraction peak at small angles (Figure 5.8 (d)). The wall-to-wall distance of the obtained mesostructure estimated from SEM data and from the small angle XRD patterns is about 13 ± 2 nm, which is similar to the values obtained with the same template for other metal oxides assembled from nanoparticles [2,9,27]. The mesoporous morphology of the ITO films is also confirmed by TEM (Figure 5.8 (a)). The HR-TEM images of the films after annealing reveal that they are highly crystalline, being composed of crystals about 8 nm in size (Figure 5.8 (b)). The d-spacing of the lattice fringes in the crystals and the SAED patterns of the larger areas of the films (Figure 5.8 (c)) correspond solely to the cubic ITO structure in the walls.

We emphasize that our attempts to prepare mesoporous crystalline ITO films from molecular $InCl_3$ and $SnCl_4$ precursors using the same Pluronic template were not successful, in spite of numerous efforts to optimize self-assembly conditions such as metal ion to polymer ratio, humidity control during deposition, annealing temperature and annealing program. The films assembled from the molecular precursors do not possess any regular mesoporous morphology, but rather contain irregular larger pores that could originate from a phase separation of inorganic and polymer components (Figure 5.6 (b)). We also observed sheet-like particles randomly oriented about perpendicular to the substrate surface (bright areas in Fig5.6 (b)). A similar kind of a sheet-like morphology was described for In-Sn hydroxide films obtained by electrochemically initiated hydrolysis [22], which suggests some similarity in the crystallization mechanism of the indium tin oxide films obtained from molecular precursors. Besides the obvious difference in morphology, the films assembled from molecular precursors significantly differ in the degree of crystallinity. The crystalline structure of the framework formed from both nano-hydroxides and the molecular precursors correspond to the cubic ITO phase after annealing at 300 ℃ (Figure

5.7). However, the films assembled from nano-hydroxides feature much higher crystallinity and a larger crystal size compared to those obtained from the molecular precursors after the thermal treatment at the same conditions. The volume-averaged size of crystalline domains of the film formed from nano-hydroxides was estimated at about 9.3 nm and ca. 9.1 nm by whole-powder-pattern profile refinements and the double-Voigt method, respectively (see Experimental Part and Appendix I for details), while the volume-averaged domain size of the film obtained from the molecular precursors was estimated at about 5.3 nm by both methods. These results indicate the presence of very small strains in both samples. (Note that the size of the crystals in the walls of mesoporous films is much smaller than that obtained for pure nano-hydroxide treated at the same temperature in the absence of Pluronic polymer – see Figure 5.3 (a), which could be attributed to a constraining effect of the latter).

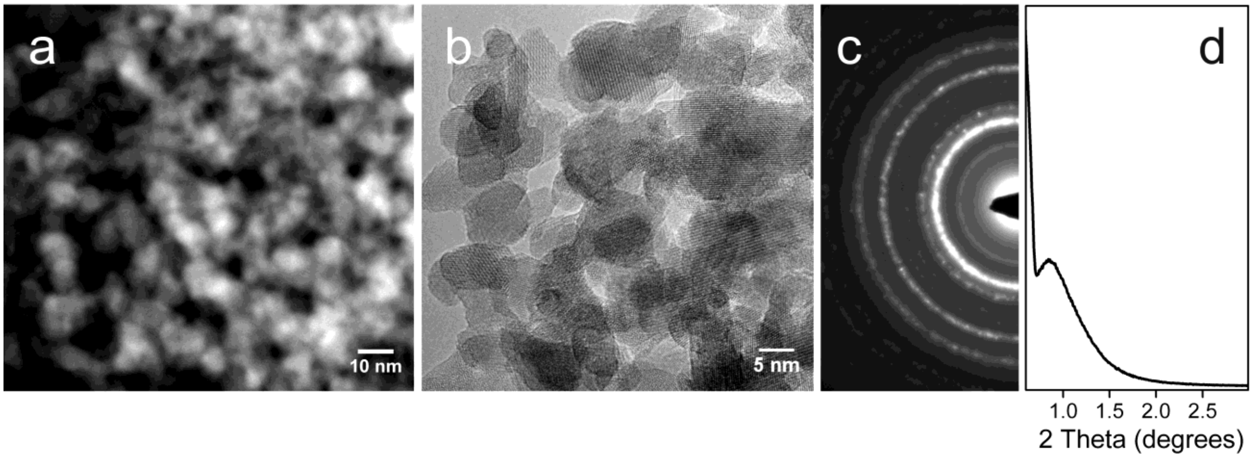

Figure 5.8 Mesoporosity and crystallinity of the ITO films assembled from nano-hydroxides: (a) STEM-HAAD image, (b) HR-TEM image, (c) SAED pattern and (d) small angle XRD pattern of mesoporous ITO films after heat treatment at 300 ℃ in air followed by heating at 300 ℃ in 5% H2/N2.

The textural properties and the accessibility of the internal surface of the films were determined by the analysis of krypton sorption isotherms taken at 77 K (Figure 5.9). The film annealed at 300 ℃ in N_2/H_2 atmosphere exhibits a typical type IV isotherm with adsorption branch approaching a plateau at the relative pressure close to 1. The capillary condensation at a larger equilibrated saturated pressure denotes a large pore size, while the steepness of the adsorption and desorption branches indicate a rather sharp pore size distribution. It can be concluded that the mesoporous structure of this sample is characterized by a narrow pore size distribution and the absence of pore blocking. Considering the specific surface area of 190 m^2/cm^3, roughness factor of 45 ± 2 cm^2/cm^2 for a film ca. 200 nm in thickness and the porosity of 44% (see Experimental part for details), the mesostructured film assembled from pre-formed indium tin hydroxide nanoparticles and treated at 300 ℃ is highly porous with a regular pore size distribution and excellent accessibility of the pores.

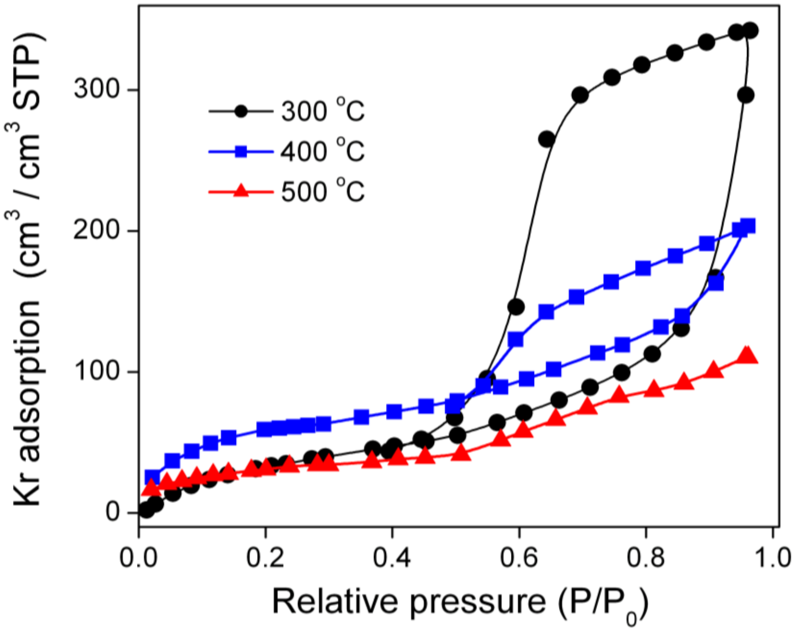

Figure 5.9 Kr sorption isotherms (measured at 77 K) on mesoporous ITO films assembled from nano-hydroxides treated in forming gas (5% H2/N2) at different temperatures.

A further increase in the annealing temperature in N_2/H_2 atmosphere leads to restructuring of the mesoporous system. At 400 ℃, the decrease in the volume of adsorbed krypton and the flatness of the hysteresis loop indicates that the pore size distribution has become much broader with some proportion of pores lager than ca 10 nm, which might be caused by an increase in the crystal size. The sample calcined at 500 ℃ does not exhibit pores smaller than ca. 10 nm any more, which can be attributed to a mesostructure collapse due to the extensive crystal growth at this temperature.

5.2.3. Electrical conductivity and application as electrodes

The ITO material obtained after calcination of nano-hydroxides at 300 ℃ in air shows some electrical conductivity ($5.2\cdot10^{-4}$ S/cm), which is still rather low for practical applications. In order to increase the conductivity, we treated the particles and films either in inert N_2 or in a reducing forming gas (5% H_2 in N_2) atmosphere at temperatures ranging from 300 ℃ to 500 ℃, which is commonly performed for enhancing the conductivity of chemically produced ITO. The subsequent annealing in inert or reducing atmospheres leads to a change in the color of powder samples from yellow to dark blue or black, which is usually attributed to the formation of oxygen vacancies (the color change of the films after similar treatment is practically undetectable by the naked eye because of their much smaller thickness).

As can be seen from the Figure 5.10, the additional thermal treatment in non-oxidative conditions indeed significantly increases the conductivity of mesoporous ITO frameworks. Annealing at 300 °C in nitrogen increases the conductivity to $1.5\cdot10^{-3}$ S/cm, and after treatment in the forming gas the conductivity becomes as high as $5.4\cdot10^{-1}$ S/cm. The difference in conductivity of the films annealed in different atmospheres becomes however less pronounced with the increased annealing temperature. For a film annealed at 400 ℃ the conductivity after treatment in nitrogen and forming gas atmosphere become already comparable (0.8 and 9.5 S/cm, respectively), and for the films heated at 500 ℃ the reverse effect is observed, which could originate from deterioration of the films' continuity due to the mesostructure collapse.

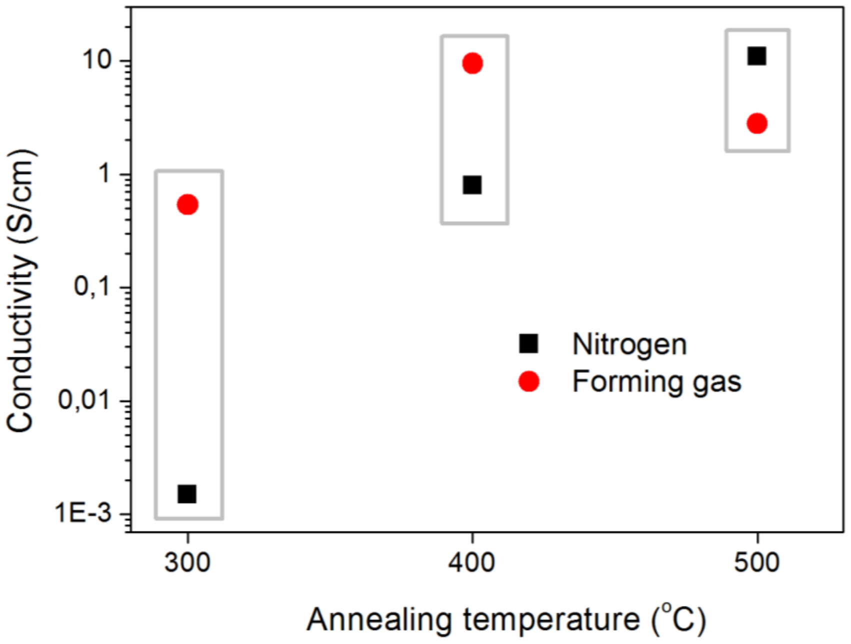

Figure 5.10 Specific conductivity of mesoporous ITO films produced from nano-hydroxides, calcined in air at 300 ℃ and treated in nitrogen or forming gas at 300 ℃ to 500 ℃.

The large internal surface area, accessibility of pores and conductive transparent framework offer potential for novel applications of mesoporous ITO films, such as a conducting electrode matrix for immobilization of functional redox molecules. To test the utility of mesoporous ITO films as electrodes, we functionalized them with standard redox molecules using both non-covalent and covalent immobilization (the data presented here are obtained with the ITO films subsequently heated at 300 °C in air and forming gas, respectively). Negatively charged hexacyanoferrate $K_3Fe(CN)_6$ complexes were grafted electrostatically using a cationic polyelectrolyte adsorbed on the ITO surface. Ferrocene carboxylic acid was anchored covalently on the amino-functionalized ITO electrode via amide bonds [2,28]. The cyclic voltammograms of the molecules grafted into the mesoporous ITO films exhibit Gaussian-shaped peaks of reversible reduction and oxidation, characteristic for electrodes with immobilized redox species (Figure 5.11). The electrochemically accessible surface coverage obtained from the area under the oxidation/reduction peaks is 810 pmol/cm^2 for hexacyanoferrate and 380 pmol/cm^2 for ferrocene molecules. The difference in surface loading can be attributed primarily to a different efficiency of immobilization. The polycationic electrolyte provides a high density of anchoring sites, leading to a much higher amount of incorporated molecules in comparison with the covalently bonded ferrocene carboxylic acid. In comparison, surface coverage on a flat reference ITO surface is 19 pmol/cm^2 and 8 pmol/cm^2 for electrostatically immobilized hexacyanoferrate and covalently bound ferrocene molecules, respectively. In both cases, the electrochemically accessible loading is up to 50 times higher for mesoporous electrodes compared to the flat ITO electrodes modified in the same way. This increase in the Faradaic charge is in excellent agreement with the specific surface areas of ca. 45 cm^2/cm^2 of the films obtained by Kr adsorption measurements. Consequently, the mesoporous ITO films are perfectly suitable for the application as transparent electrode layers with a very high surface area, enabling direct electrochemical addressing of redox molecules immobilized on their surface.

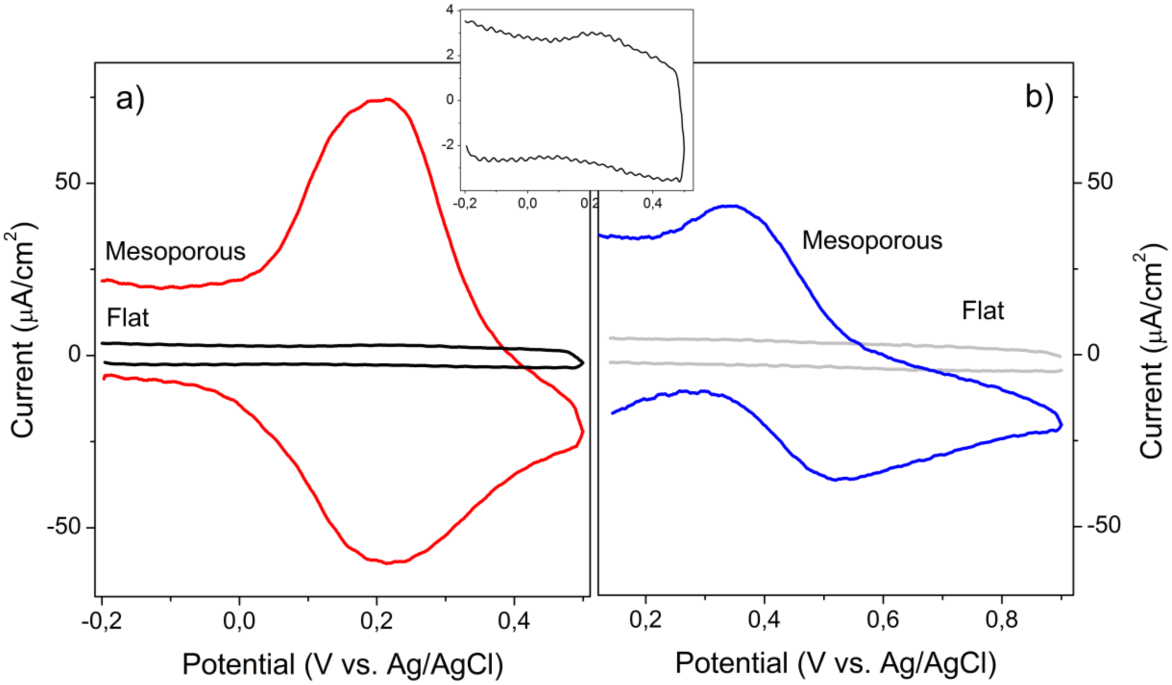

Figure 5.11 Cyclic voltammograms of (a) hexacyanoferrate $K_3Fe(CN)6$ immobilized on the mesoporous ITO electrode subsequently heated at 300 ℃ in air and forming gas, respectively (red) and flat ITO film (black and inset) via electrostatic interactions with polycationic electrolyte, and (b) ferrocene carboxylic acid covalently immobilized in the pores of mesoporous ITO (blue) and flat ITO (grey) by amide bonds. The inset shows cyclic voltammogram of $K_3Fe(CN)6$ immobilized on the flat ITO film via electrostatic interactions with polycationic electrolyte. Scan rate 200 mV/s.

5.3. Conclusions

Solvothermal reactions in ethylene glycol or higher polyols have been known for a long time as a suitable approach towards the fabrication of crystalline indium tin oxide (ITO) nanoparticles. We have found that a decrease in the reaction temperature leads to the formation of another type of crystalline nanoparticles corresponding to hexagonal indium tin hydroxide. The obtained 'nano-hydroxides' are just a few nanometer in size, nearly spherical, non-agglomerated and, in contrast to ITO nanoparticles, very hydrophilic and perfectly dispersible in water at high concentrations. A remarkable feature of the obtained hydroxide nanoparticles is their facile transformation to ITO at about 300 °C. The nano-hydroxide/ITO transformation involves the intermediate formation of an amorphous state due to a loss of the covalently bond water, but without significant changes in size and shape of the nanocrystals.

The novel crystalline mesoporous ITO films assembled from nano-hydroxides and the commercial surfactant Pluronic F127 polymer and heat treated at 300 °C feature a regular mesoporosity with a mesostructure periodicity of about 13 ± 2 nm, high surface area of 190 m^2/cm^3, and a porosity of 44% (see details in Experimental part). Upon thermal treatment in inert N_2 or reducing forming gas atmospheres, the electrical conductivity of the films increases remarkably, reaching up to 9.5 S/cm. As a result, the films coated on the electrode surfaces can be used as conducting porous matrices for incorporation of redox molecules with a very high loading using covalent or electrostatic grafting procedures. Due to the high conductivity of the ITO framework, each incorporated molecule can be addressed electrochemically, leading to a largely increased electrochemical signal proportional to the electrode surface area.

The perfect dispersibility of nano-hydroxides without any stabilizing agents and their preferential interaction with the hydrophilic part of amphiphilic molecules leading to their self-assembly make the ultra-small nano-hydroxides very attractive building blocks for the elaboration of nanostructured ITO materials. Their compatibility with amphipilic polymer template molecules enables their controlled manipulation and assembly into desirable nanostructures directed by the choice of the template, and the solubility in water further extends the choice of possible structure-directing agents. Finally, the facile transformation of the assembled nano-hydroxides into mesoporous crystalline ITO with similar morphology makes the hydroxide/oxide approach a very promising tool for the fabrication of various ITO nanostructures. We believe that the nano-hydroxides can become universal building blocks for the fabrication of crystalline ITO materials with arbitrary nano-morphologies.

5.4. Experimental part

5.4.1. Synthesis of nanoparticles and mesoporous films

Nanoparticles of indium tin hydroxide were prepared by a solvothermal synthesis using indium(III) chloride and tin(IV) chloride as metal oxide precursors, ethylene glycol (EG) as a solvent, and sodium hydroxide as a hydrolysis reagent. In a typical procedure, 0.091 g (0.35 mmol, 0.04 mL) of tin (IV) chloride (Aldrich) was added to a clear solution of 0.698 g (3.15 mmol) of indium (III) chloride (ABCR) in 7 mL (0.13 mmol) of ethylene glycol (Sigma-Aldrich, ≥99%, used without further drying). The molar ratio of tin and indium was 1:9 (mol:mol). Separately, 0.420 g (10.5 mmol) of sodium hydroxide (Aldrich, 97%) was dissolved in 7 mL (0.13 mmol) of EG at 0 ℃. Both solutions were mixed at 0 ℃ and stirred for another 15 minutes. The mixture was transferred into a Teflon-lined autoclave and kept in a laboratory oven for 28 hours at 200 ℃. The formed product was separated by centrifugation (50000 rcf, 20 min) and washed twice with bi-distilled water (Milli-Q Academic A10), being separated by centrifugation after each washing step. The solid part resulting from centrifugation was collected and used without drying for the preparation of colloidal solutions. The solid content of the collected material could differ for different synthesis batches; it was determined for each new batch either by weighing of a certain amount before and after evaporation of water, or using thermogravimetric analysis. The average solid content in the washed nanoparticles after centrifugation was 50 ± 10 %.

For the fabrication of mesoporous films, the wet nanoparticles containing 90 mg of solid indium tin hydroxide were first re-dispersed in 0.5 ml (27 μmol) of water to result in a slightly turbid colloidal dispersion, which turned transparent after the addition of 0.2–0.5 ml of concentrated acetic acid depending on the concentration of nanoparticles in the colloidal solution. Afterwards, 30 mg (2.6 μmol) of Pluronic F127 (Sigma) was dissolved in the particle dispersion. The resulting clear solutions were deposited on different substrates such as glass, ITO-coated glass or Si wafers (size ca. 1.5 cm x 2 cm) by dip-coating (withdrawal speed 6 mm/s) or spin-coating (30 - 50 μL per 1 cm^2 substrate area) at 1000 rpm for 30 seconds. The dried films were heated to 300 ℃ in air (with a ramp of 0.5 ℃/min) for 2 hours. For improvement of electrical conductivity, template-free mesoporous ITO films were further annealed in inert N_2 or reducing forming gas (5% H_2/N_2) atmosphere at 300 to 500 ℃ (with a ramp of 1 ℃/min) for 30 min.

For electrochemical characterization, the mesoporous ITO films were deposited on a conducting ITO-coated glass substrate by spin-coating as described above. Functionalization of ITO films was performed in two ways. For electrostatic anchorage of potassium hexacyanoferrate $K_3[Fe(CN)_6]$, the films were immersed first in a 0.20 wt% solution of poly(diallyldimethylammoniumchloride) (PDDA, MW 100.000 - 200.000) in water for 12 hours at room temperature. The PDDA-modified mesoporous ITO films were then stirred in a 10 mM $K_3[Fe(CN)_6]$ aqueous solution for 6 hours. The electrode was washed twice with bi-distilled water after each functionalization step. For electrochemical measurements, 0.1 M KCl in water was used as electrolyte. For the covalent anchorage of ferrocene moieties, the mesoporous ITO films were treated first in a 20 mM solution of 3-aminopropyltriethoxysilane (APTES) in dichloromethane under reflux for 3 h, followed by washing twice with dichloromethane. The APTES-functionalized films were stirred in reflux for 3 h in a 0.2 mM solution of ferrocene carboxylic acid and a 2 mM solution of N,N-dicyclohexylcarbodiimid in dichloromethane in reflux for 3 h and washed twice with dichloromethane. For electrochemical measurements, 0.5 M $LiClO_4$ in acetonitrile was used as electrolyte.

5.4.2. Characterization of nanoparticles and mesoporous films

Transmission electron microscopy (TEM) was performed using a FEI Titan 80-300 instrument equipped with a field emission gun. Due to the fast decomposition of hydroxide nanoparticles in the electron beam, the measurements were performed at 80 kV. The particulate samples were prepared by evaporating a drop of a diluted suspension of particles in water on a Plano holey carbon-coated copper grid. TEM of films was carried out by removing the thin-film samples from the substrate and transferring them onto a holey carbon-coated copper grid. Scanning electron microscopy (SEM) was performed on a JEOL JSM-6500F scanning electron microscope equipped with a field emission gun operated at 4 kV.

X-ray diffraction measurements at small and wide angle were carried out in reflection mode using a Bruker D8 Discover diffractometer with Ni-filtered CuK$_\alpha$-radiation ($\lambda = 1.5406$ Å), and equipped with a Vantec-1 position-sensitive detector. XRD patterns of the unknown tin-doped indium hydroxide phase were analyzed with computer programs PRO-FIT [29] and CheckCell (a software performing automatic cell/space group determination) [30]. The Bragg angle position ($2\theta_B$), integrated intensities and FWHM values of the diffraction lines (Table AI1) were determined by using the individual profile fitting method with program PRO-FIT and taken as input data for the program CheckCell. The pseudo-Voigt profile function defined by Wertheim et al. [31] and a second order polynomial model for background intensity were used in the refinement. Due to the significant overlap of broad diffraction lines, the values extracted by program PRO-FIT (Table AI1) were obtained after individual refinement of 2θ regions (~ 20°) containing 5 to 6 diffraction lines.

The particle size d of indium tin hydroxide nanoparticles was estimated from the broadening of the diffraction lines with $2\theta_B$ positions at 22.3° and 45.5° in the XRD pattern using the Scherrer equation $d = K\lambda/(B\cos\theta_B)$, where B is the full width at half maximum (FWHM) of a diffraction line corrected for the corresponding FWHM value for standard, θ_B is the diffraction angle and K

is the Scherrer's constant (about 0.9), and from the HRTEM images. The particle size in HRTEM was measured manually for ca. 100 particles.

A more accurate crystalline domain size determination from a line-broadening analysis of XRD patterns was performed by using two different methods: whole-powder-pattern profile refinements (Le Bail method [32], program GSAS [33] with graphical user interface EXPGUI [34]) and double-Voigt method [35] (programs SHADOW [36] and BREDTH [37]). The results of whole-powder-pattern profile refinements were obtained by following the procedure proposed in the Size/Strain Round Robin [38]**.** In the refinement we used a modified pseudo-Voigt function defined by Thompson et al [39], which gave the following expression for Gaussian and Lorentzian observed line widths:

$$\Gamma_G^2 = U\tan^2\theta + V\tan\theta + W + P/\cos^2\theta \qquad (1)$$

$$\Gamma_L = (X + X\mathrm{e}\cos\phi)/\cos\theta + (Y + Y\mathrm{e}\cos\phi)\tan\theta + Z \qquad (2)$$

where Γ is the full width at half maximum (FWHM) of the line profile, U, V, W, X, Y, Z, Xe and Ye are refinable parameters. The size and strain contribution to the line broadening can be given by the following equation:

$$\beta_S = \lambda/(D_V\cos\theta) \qquad (3)$$

$$\beta_D = e\, 4\tan\theta \qquad (4)$$

where λ is the wavelength, D_v is the volume-averaged domain size, e represents the upper limits of micro-strain, while β_S and β_D represent the integral breadths of the Voigt function resulting from size and strain contribution, respectively. By comparing the equations (1) and (2) with the equations (3) and (4) it is easy to recognize that parameters X, Xe and P will relate to size broadening and Y, Ye and U to strain broadening. Therefore only those 6 profile parameters were refined in the Le Bail refinements of ITO samples, while all other profile parameters assumed the values obtained upon the refinement of the LaB_6 standard (Figure AI3). In order to obtain pure physically broadened profile parameters, used in the calculation of β_S and β_D values, the obtained values of the refined parameters *U, X, Y, P* for samples were corrected by the corresponding values obtained for the standard [38]. (See Ref. 38 for a more detailed description of the whole procedure).

In the double-Voigt method [35], which is equivalent to the Warren-Averbach approach [40], both area- and volume-weighted domain size and the root-mean-square strain (RMSS) were calculated from 'pure' physically (specimen, structurally) broadened diffraction-line profiles of several most prominent diffraction lines (program BREADTH [37]). Pure physically broadened diffraction-line profiles were obtained by varying the parameters of the Voigtian profile shape function convoluted with the instrumental profile (split Person VII function fitted to the diffraction lines of LaB_6 standard) to obtain the best fit to the observed data [41] (program SHADOW) [36].

Textural properties of the mesostructured films were analysized by Kr sorption measurements at 77 K using an ASAP 2010 apparatus (Micromeritics). Porosity of the films was determined from the measured pore volume related to the volume of the film (calculated from exposed film area and the film thickness). Film thickness was determined using a profilometer Veeco Dektak 150 equipped with a diamond stylus (12.5 µm radius) in contact mode. The TGA analysis was performed on a Netzsch STA 4400 C TG/DSC (heating rate of 1 K/min in a stream of synthetic air of 25 ml/ min).

The dispersion behavior of nanoparticles was studied by dynamic light scattering using a Malvern Zetasizer-Nano equipped with a 4 mW He-Ne laser (633 nm) and an avalanche photodiode detector.

XPS (X-ray photoelectron spectroscopy) analysis of the template free mesoporous ITO films on silicon substrate was performed using a VSW HA 100 electron analyzer and the K_{α} radiation provided by a non-monochromatized aluminum anode system (Al K_{α} = 1486.6 eV). Raman spectra were recorded with a LabRAM HR UV-VIS (Horiba Jobin Yvon) Raman microscope (Olympus BX41) with a Symphony CCD detection system using a HeNe laser at 632.8 nm.

DC electrical conductivity measurements on template-free mesoporous ITO films were conducted following the Hall method (ECOPIA HMS 3000) using a magnetic field of 0.55 T.

Cyclic voltammograms were collected using a PARSTAT 2273 potentiostat with PowerSuite 2.56 software for data collection and analysis in a standard three-electrode electrochemical cell using Pt wire as a counter electrode and Ag/AgCl/1M KCl as a reference electrode. Functionalized films on ITO glass used as working electrodes were masked with a Teflon-coated glass fiber tape leaving an exposed area of 0.75 cm^2.

5.5. Chapter references

1. Fattakhova-Rohfing, D., et al., Transparent conducting films of indium tin oxide with 3D mesopore architecture. Adv. Mater., 2006. **18**(22): p. 2980-+.

2. Müller, V., et al., Transparent Conducting Films of Antimony-Doped Tin Oxide with Uniform Mesostructure Assembled from Preformed Nanocrystals. Small, 2010. **6**(5): p. 633-637.

3. Hou, K., et al., Dye-Anchored Mesoporous Antimony-Doped Tin Oxide Electrochemiluminescence Cell. Adv. Mater., 2009. **21**(24): p. 2492-+.

4. Frasca, S., et al., Mesoporous Indium Tin Oxide as a Novel Platform for Bioelectronics. Chemcatchem, 2010. **2**(7): p. 839-845.

5. Wang, Y.D., et al., Ordered Mesoporous Sb-, Nb-, and Ta-Doped SnO2 Thin Films with Adjustable Doping Levels and High Electrical Conductivity. ACS Nano, 2009. **3**(6): p. 1373-1378.

6. Aksu, Y., et al., A Molecular Precursor Approach to Tunable Porous Tin-Rich Indium Tin Oxide with Durable High Electrical Conductivity for Bioelectronic Devices. Chem. Mater., 2011. **23**(7): p. 1798-1804.

7. Aksu, Y. and M. Driess, A Low-Temperature Molecular Approach to Highly Conductive Tin-Rich Indium Tin Oxide Thin Films with Durable Electro-Optical Performance. Angew. Chem. Int. Ed., 2009. **48**(42): p. 7778-7782.

8. von Graberg, T., et al., Mesoporous tin-doped indium oxide thin films: effect of mesostructure on electrical conductivity. Sci. Tech. Adv. Mater., 2011. **12**(2): p. 025005.

9. Liu, Y.J., et al., Niobium-Doped Titania Nanoparticles: Synthesis and Assembly into Mesoporous Films and Electrical Conductivity. ACS Nano, 2010. **4**(9): p. 5373-5381.

10. Ba, J.H., et al., Non-aqueous synthesis of tin oxide nanocrystals and their assembly into ordered porous mesostructures. Adv. Mater., 2005. **17**(20): p. 2509-+.

11. Coquil, T., et al., Thermal Conductivity of Ordered Mesoporous Titania Films Made from Nanocrystalline Building Blocks and Sol-Gel Reagents. J. Phys. Chem. C, 2010. **114**(29): p. 12451-12458.

12. Brezesinski, T., et al., Templated Nanocrystal-Based Porous TiO2 Films for Next-Generation Electrochemical Capacitors. J. Am. Chem. Soc., 2009. **131**(5): p. 1802-1809.

13. Endo, Y., et al., Direct Preparation and Size Control of Highly Crystalline Cubic ITO Nanoparticles in a Concentrated Solution System. Chem. Lett., 2008. **37**(12): p. 1278-1279.

14. Buhler, G., D. Tholmann, and C. Feldmann, One-pot synthesis of highly conductive indium tin oxide nanocrystals. Adv. Mater., 2007. **19**: p. 2224-+.

15. Ba, J., et al., Crystallization of indium tin oxide nanoparticles: From cooperative behavior to individuality. Small, 2007. **3**(2): p. 310-317.

16. Xu, X.X. and X. Wang, Size- and Surface-Determined Transformations: From Ultrathin InOOH Nanowires to Uniform c-In2O3 Nanocubes and rh-In2O3 Nanowires. Inorg. Chem., 2009. **48**(8): p. 3890-3895.

17. Askarinejad, A., et al., Synthesis and characterisation of In(OH)3 and In2O3 nanoparticles by sol-gel and solvothermal methods. J. Exp. Nanosci., 2010. **5**(4): p. 294-301.

18. Perez-Maqueda, L.A., L.F. Wang, and E. Matijevic, Nanosize indium hydroxide by peptization of colloidal precipitates. Langmuir, 1998. **14**(16): p. 4397-4401.

19. Dong, H.X., et al., Nanosheets-Based Rhombohedral In2O3 3D Hierarchical Microspheres: Synthesis, Growth Mechanism, and Optical Properties. J. Phys. Chem. C, 2009. **113**(24): p. 10511-10516.

20. Wang, C.Q., D.R. Chen, and X.L. Jiao, Flower-like In2O3 Nanostructures Derived from Novel Precursor: Synthesis, Characterization, and Formation Mechanism. J. Phys. Chem. C, 2009. **113**(18): p. 7714-7718.

21. Qiu, Y., et al., Aqueous deposition of ultraviolet luminescent columnar tin-doped indium hydroxide films. Adv. Funct. Mater., 2008. **18**(17): p. 2572-2583.

22. Kovtyukhova, N.I. and T.E. Mallouk, Electrochemically Assisted Deposition as a New Route to Transparent Conductive Indium Tin Oxide Films. Chem. Mater., 2010. **22**(17): p. 4939-4949.

23. Kovtyukhova, N.I. and T.E. Mallouk, Conductive indium-tin oxide nanowire and nanotube arrays made by electrochemically assisted deposition in template membranes: switching between wire and tube growth modes by surface chemical modification of the template. Nanoscale, 2011. **3**(4): p. 1541-1552.

24. Song, J.E., et al., Preparation and characterization of monodispersed indium-tin oxide nanoparticles. Coll. Surf. A, 2005. **257-58**: p. 539-542.

25. Xu, H.F., et al., Template synthesis of tin-doped indium oxide (ITO)/polymer and the corresponding carbon composite hollow colloids. Coll. Polym. Sci., 2007. **285**(10): p. 1101-1107.

26. Pramanik, N.C., S. Das, and P.K. Biswas, The effect of Sn(IV) on transfonnation of co-precipitated hydrated In(III) and Sn(IV) hydroxides to indium tin oxide (ITO) powder. Mater. Lett., 2002. **56**(5): p. 671-679.

27. Szeifert, J.M., et al., Ultrasmall Titania Nanocrystals and Their Direct Assembly into Mesoporous Structures Showing Fast Lithium Insertion. J. Am. Chem. Soc., 2010. **132**(36): p. 12605-12611.

28. Fattakhova-Rohlfing, D., et al., Functionalized mesoporous silica films as a matrix for anchoring electrochemically active guests. Langmuir, 2005. **21**(24): p. 11320-11329.

29. Toraya, H., Whole-powder-pattern fitting without reference to a structure model - application to X-Ray-powder diffractometer data. J. Appl. Cryst., 1986. **19**: p. 440.

30. Laugier, J. and B. Bochu, CHECKCELL: A Software Performing Automatic Cell/Space Group Determination, Collaborative Computational Project Number 14. 2000: Laboratory of Materials and Physical Engineering, School of Physics, University of Grenoble, France.

31. Wertheim, G.K., et al., Determination of Gaussian and Lorentzian content of experimental line-shapes. Rev. Sci. Instrum., 1974. **45**: p. 1369-1371.

32. Le Bail, A., H. Duroy, and J.L. Fourquet, Abinitio Structure Determination of Lisbwo6 by X-Ray-Powder Diffraction. Mater. Res. Bull., 1988. **23**(3): p. 447-452.

33. Larson, A.C.V.D., R. B., General Structure Analysis System GSAS, in Los Alamos National Laboratory Report. 2001.

34. Toby, B.H., EXPGUI, a graphical user interface for GSAS. J. Appl. Cryst., 2001. **34**: p. 210-213.

35. Balzar, D. and H. Ledbetter, Voigt-function modeling in Fourier-analysis of size-broadened and strain-broadened X-Ray-diffraction peaks. J. Appl. Cryst. , 1993. **26**: p. 97-103.

36. Howard, S.A., Adv. X-Ray Anal. , 1989. **32**: p. 523-530.

37. Balzar, D., Profile fitting of X-Ray diffraction lines and Fourier-analysis of broadening J. Appl. Cryst. , 1992. **28**: p. 559-570.

38. Balzar, D., et al., Size-Strain Line-Broadening Analysis of the Ceria Round-Robin Sample. J. Appl. Cryst. , 2004. **37**: p. 911-924.

39. Thompson, P., D.E. Cox, and J.B. Hastings, Rietveld refinement of Debye-Scherrer synchrotron X-Ray data from Al2O3 J. Appl. Cryst. , 1987. **20**: p. 79-83.

40. Warren, B.E., X-ray Diffraction. Reading. 1969: MA. Addison-Wesley

41. Bish, D.L. and J.E. Post, eds. Modern powder diffraction, Reviews in Mineralogy. Vol. 20. 1989, Mineralogical society of America: Washington.

Chapter 6

Macroporous ITO films assembled from indium tin hydroxide nanoparticles

6.1. Introduction

3D periodically organized porous transparent conducting oxide electrodes have been considered as promising platforms for immobilizing functional species onto the interfaces, by taking advantage of increased surface area, accessible pores and a conductive framework [1-4]. When the functional species are at the scale of hundred nanometers, a suitably-sized periodicity for nanostructured TCO electrodes is however required, for example, to achieve the incorporation of biological elements into the nanostructure for tissue engineering, of organic polymers for enhanced photovoltaic devices, and so on. Colloidal crystal templating (CCT) is the most commonly employed method to fabricate periodic porous films with large pores from about 50 nm to 1000 nm, where colloids such as silica spheres, polystyrene (PS) spheres, poly(methyl methacrylate) (PMMA) latex beads can be taken as the templates [5-10]. This approach has been applied to the fabrication of a series of metal oxides, however, the synthesis of transparent conducting oxides has not been much investigated so far.

Recently, Ozin [11] and Xu [12] have taken silica balls and polystyrene spheres as opal templates, and prepared macroporous inverse-opal structured antimony doped tin oxide (ATO) films [11] and fluorine doped tin oxide (FTO) films [12], respectively. A critical step in their work is the liquid infiltration of inorganic precursors into the voids of preformed opal templates. On one side, it is a time consuming step; on the other side, a suitable control on the infiltration is very important, since excessive infiltration will result in the formation of a dense crust top layer that can block the macropores, while insufficient infiltration will produce a metastable structure that can collapse during the following thermal treatment. Additionally, using this method, capillary forces attributed to the solvent evaporation and inorganic framework crystallization can easily create unwanted cracks in the layers. Hatton et al. have very recently reported an alternative approach to fabricate crack-free periodically ordered macroporous silica films, through the co-assembly of colloidal crystal template PMMA and inorganic precursor tetraethoxy silane (TEOS). This approach avoids the critical step of liquid infiltration in the template self-assembly method employed in Ozin and Xu's work. Besides, it also strongly reduces the formation of cracks.

Here in this work, we employed the procedure of co-assembly to fabricate macroporous indium tin oxide (ITO) films, with PMMA latex beads as the template, and preformed nanoparticles of indium tin hydroxide as the inorganic precursors for ITO. Different from Hatton's work [13], which took the molecular precursors (TEOS) as the inorganic source, we attempted to employ the preformed nanoparticles in the co-assembly procedure and examine the applicability of this method. Moreover, using PMMA latex beads as the templates can be considered as a second example for the versatile utilization of preformed indium tin nanohydroxide as basic building blocks to fabricate complex nanostructured ITO materials.

6.2. Results and Discussion

A highly intimate mixing between templates and inorganic precursors, i.e., mono-dispersion of both the PMMA beads and inorganic precursors in their separate colloidal solutions, plays a fundamental role for the successful application of the co-assembly procedure (Figure 6.1). In this work, both the inorganic precursors and the templates were dispersed in the water first and the solution mixture was then deposited onto glass or ITO coated glass substrates by a dip coating process. A further heat treatment at 400 °C in air was performed to remove the PMMA template and condense the inorganic framework, leading to template-free periodic macroporous films with crystalline ITO walls.

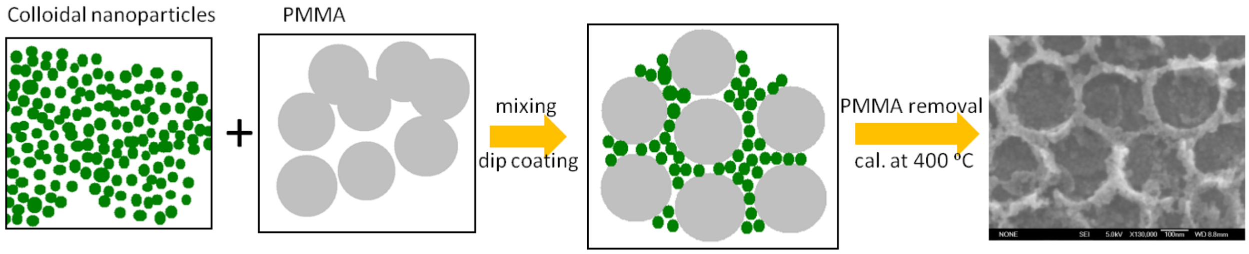

Figure 6.1 Schematic description of the fabrication process by co-assembly of ITO precursors and PMMA latex beads

For comparison, besides taking indium tin hydroxide nanoparticles as the inorganic precursors for the ITO phase, we additionally selected two other different types of precursors, crystalline ITO nanoparticles and the molecular precursors indium trichloride and tin tetrachloride.

The crystalline ITO nanoparticles were synthesized from the same material source as the indium tin hydroxide nanoparticles, with 90% indium trichloride and 10% tin tetrachloride. The solvothermal reaction at a temperature of 220 °C and reaction time of ca. 40 h leads to the generation of crystalline ITO nanoparticles. Wide-angle XRD patterns (Figure 6.2) represent their differences, where the crystalline ITO nanoparticles occur in the cubic bixbyite phase with particle size of about 10 nm (calculated from the Scherrer equation) and indium tin hydroxide nanoparticles are crystalline in the hexagonal phase [4]. The crystalline ITO particles can be dispersed in water at up to about 10 wt%, however, this suspension is not very stable and particles start to form agglomerates after the ending of external stirring. In contrast, as described in chapter 5 and [4], indium tin hydroxides could be well dispersed in water and the colloidal solution is rather stable.

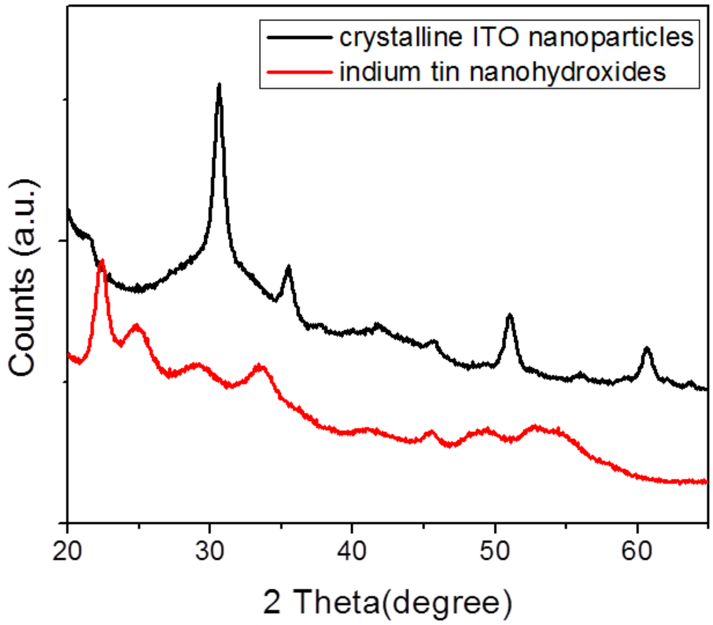

Figure 6.2 Wide angle XRD patterns of as-prepared crystalline ITO nanoparticles and indium tin nanohydroxides

PMMA latex beads with the same spherical size (initial diameter ca. 100 nm) were taken as templates to direct the assembly of these three different inorganic precursor systems. The relative weight ratio between inorganic precursor and PMMA template was kept constant, at 3:1. Top view SEM images of template-free films (figure 6.3) clearly illustrate the differences of the resulting films. For the film assembled from crystalline ITO nanoparticles (figure 6.3 (a)), it is difficult to observe any periodically ordered structure, but the agglomeration of nanoparticles; while the film assembled from highly dispersible indium tin nanohydroxides features obviously periodic porous structure (in small domains, figure 6.3 (b)), which can be attributed to its efficient dispersion in the mixture and hydrophilic surface-assisted homogeneous distribution around the template PMMA spheres. The few larger non-uniform pores might be due to the initial agglomeration of PMMA spheres. In comparison, although the molecular precursors indium trichloride and tin tetrachloride have the best solubility among the three precursors, co-assembly with PMMA template did not lead to periodically organized structure but to irregular phase separations (figure 6.3 (c) and (d)).

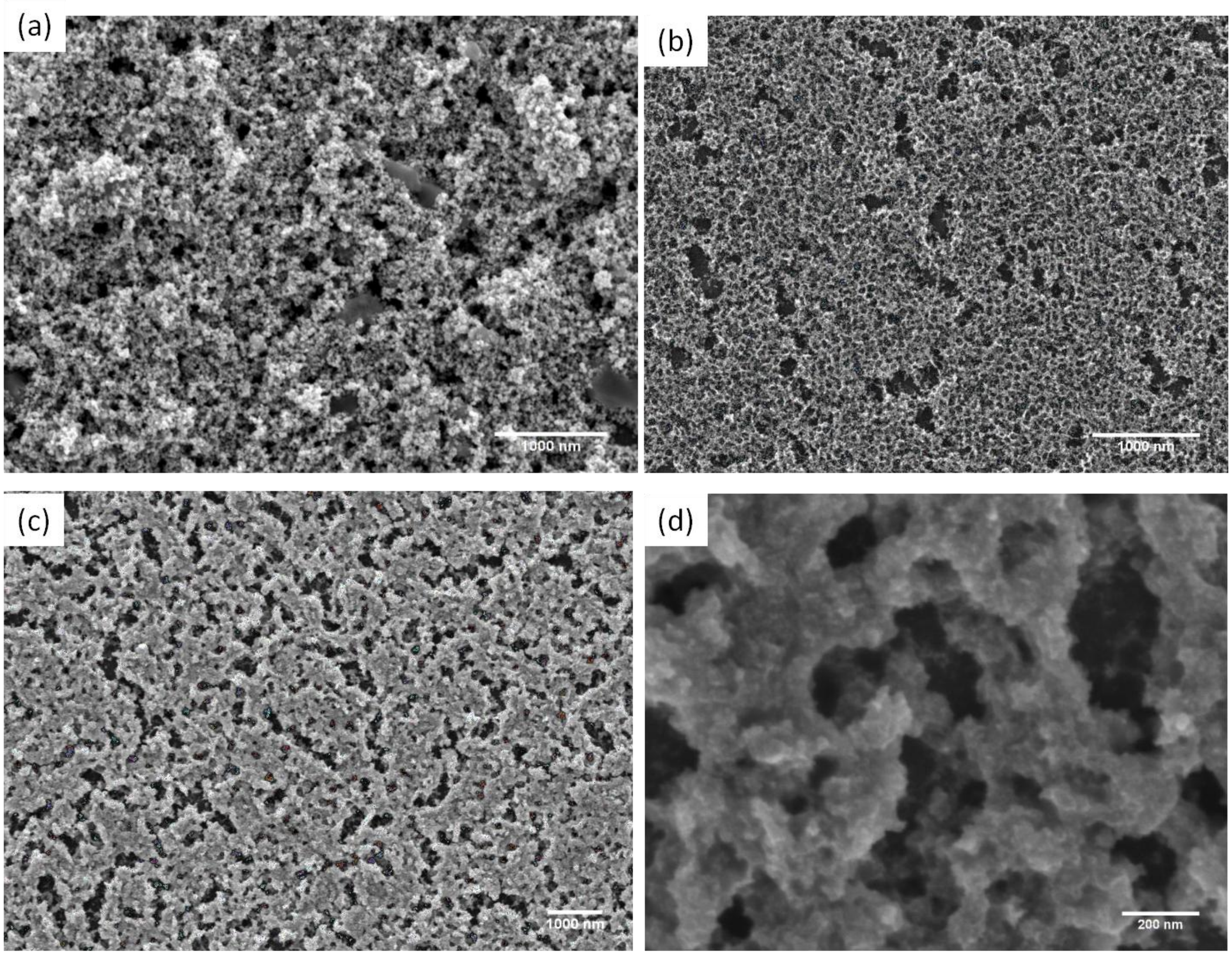

Figure 6.3 Top view SEM images of macroporous ITO films fabricated via co-assembly with different ITO precursors, (a) crystalline ITO nanoparticles, (b) indium tin nanohydroxide, and (c) and (d) molecular precursors indium trichloride and tin tetrachloride. The films were subsequently treated at 400 ℃ in air.

Moreover, using indium tin nanohydroxide nanoparticles as the basic building blocks, we also managed to prepare macroporous ITO films with different periodicities, via templating with differently sized spherical PMMA latex beads. After template removal, the average pore sizes evaluated from the SEM images are about 70 nm for films templated with 100 nm diameter PMMA latex beads (figure 6.4 (a)), and about 250 nm for films templated with 370 nm diameter PMMA latex beads (figure 6.4 (b)). The pore size decrease of about 30 % after the heat treatment can be caused by shrinkage induced by the evaporation of liquid content in the PMMA template, as well as condensation of the inorganic framework. Top view SEM images illustrate that the films feature periodic (in small domains) porous morphology with open pores. The macroporous ITO films deposited by the dip coating process are rather thin, at the order of a few hundred nanometers in thickness.

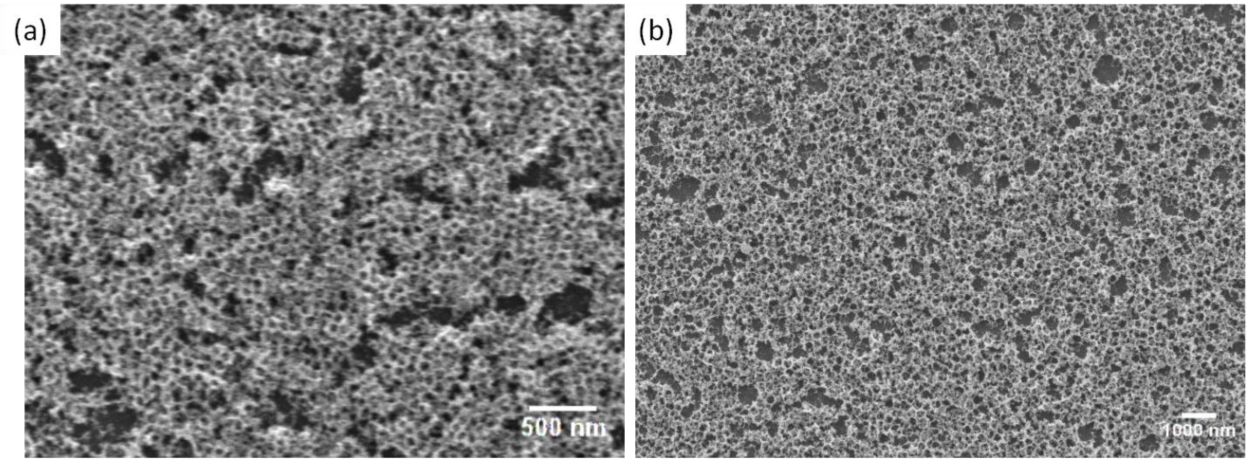

Figure 6.4 Top view SEM images of macroporous ITO with pore sizes (a) 70 nm, and (b) 250 nm. The films were treated at 400 ℃ in air and 400 ℃ in N_2.

For template-free macroporous ITO materials with these two different pore sizes, both of their XRD patterns (Figure 6.5) correspond to the cubic bixbyite ITO phase (JCPDS card 89-4596).

The results are in good agreement with the crystallization process of indium tin nanohydroxide without the presence of templates [4]. This suggests that the presence of PMMA templates does not interfere with the crystallization process of the indium tin nanohydroxide.

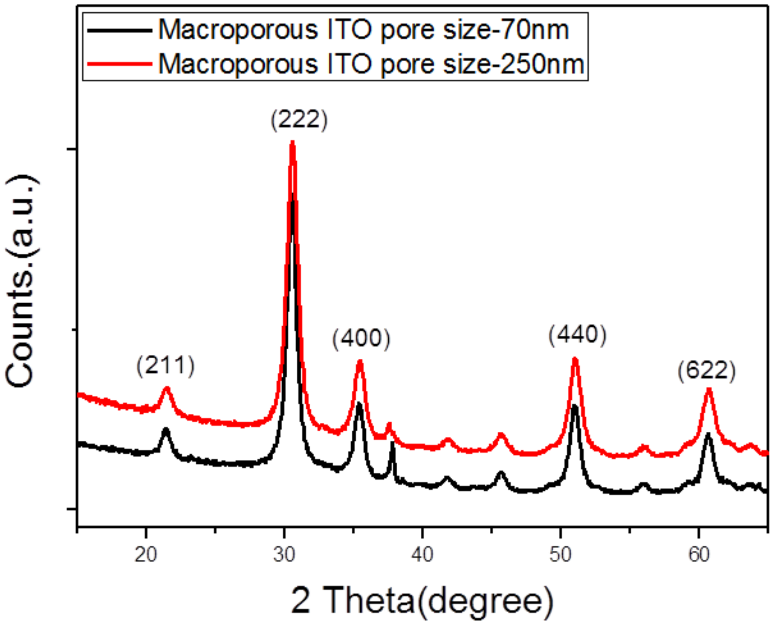

Figure 6.5 Wide-angle XRD of macroporous ITO powders with pore size of ca. 70 nm and 250 nm, respectively. The cast powders were treated at 400 ℃ in air.

The obtained results demonstrate that the co-assembly of PMMA latex beads and indium tin nano-hydroxide is a suitable approach towards the fabrication of periodically organized 3D porous ITO films with large pores. Template-free macroporous ITO films also possess high electrical conductivity. Using four point Hall measurements, we have evaluated the dc conductivities of macroporous ITO films with a thickness of about 150 nm coated on glass substrates. By conducting an annealing process at 400 ^{o}C in N_2 with the template-free films, the films with the pore size of about 70 nm show a specific conductivity of 5 S/cm, while the films with the larger pore size of 250 nm show a conductivity of about 0.6 S/cm. It has to be noted that the specific conductivity was calculated as a product of the measured sheet conductivity and the total film thickness, without taking into account the films' porosity and the actual amount of ITO in the films. Thus, the obtained high conductivity values represent both the available percolation paths for electrons and the highly conductive behavior of the macroporous ITO scaffold itself.

Additionally, the macroporous ITO films also show good optical quality and high transparency. The transmittance of the macroporous ITO films deposited on the ITO substrates is only slightly decreased compared to the substrate alone (figure 6.6), being above 75 % in the range from 450 nm to 750 nm for both pore sizes.

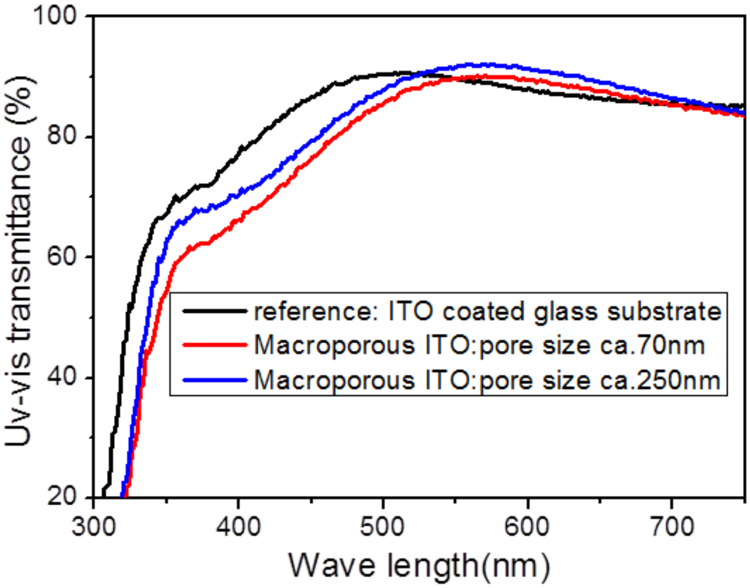

Figure 6.6 UV-vis transmittance of a commercial ITO substrate (black), and the same substrate after coating with macroporous ITO films with the pore size of 70 nm (red) and 250 nm (blue). Films are shown after the treatment at 400 ℃ in air and 400 ℃ in N_2.

6.3. Summary

In this project, we explored the simple, low-cost co-assembly approach and fabricated 3D periodically organized macroporous ITO films with preformed indium tin nano-hydroxide particles as the inorganic precursors and PMMA latex beads as the templates. The obtained ITO films feature high porosity and periodic pore systems in small domains, a crystalline and highly conductive framework, and optical transparency in the visible range. The successful preparation of ITO films with a macroporous architecture underlines the versatility of indium tin nanohydroxide particles in fabricating various nanostructured ITO materials; moreover, this also demonstrates the extension of the co-assembly approach for macroporous inverse opals from the initially used molecular species to pre-formed nanoparticles acting as basic building blocks.

6.4. Experimental part

The PMMA latex bead templates were kindly provided by Benjamin Mandlmeier in our research group. The detailed synthetic procedure can be found in [14]. For the synthesis and characterization of the pre-formed indium tin nano-hydroxides, we described the whole procedure in chapter 5 and in another publication [4]. For crystalline ITO nanoparticles, the solution mixture was prepared in the same way as indium tin hydroxide nanoparticles, but the reaction was kept at 220 ^{o}C for ca. 40 h.

To fabricate the macroporous ITO films with pore size 250 nm, 70 mg of pre-formed indium tin nano-hydroxide (inorganic content) was first dispersed in 1 mL water and stirred until the colloidal solution turned transparent (or slightly opaque). Then, the clear nano-hydroxide colloidal solution was put into an ultrasonication bath for 30 min and filtered by a 200 nm diameter filter. In parallel, 1 mL aqueous colloidal solution of 370 nm diameter PMMA latex beads (11.8 wt%) were taken into another glass vessel and the solution was put into an ultrasonication bath for 30 min. Immediately after the filtration of the nano-hydroxide colloidal solution and the ultrasonication of the PMMA suspension, the two colloidal solutions were mixed together and kept stirring for another 3-4 hours. Before transferring the mixture into the dip-coating solution container, 15-30 min ultrasonication was required to assure smooth surfaces of nanostructured ITO layers. The nanostructured ITO films were deposited via a dip coating approach. The organic PMMA latex bead templates were removed to free the pores through thermal treatment of the coated films at 400 ^{o}C in air, with a ramp of half a degree per minute and soaking time of 30 min. The annealing process was performed with a ramp speed of 1^{o}C per minute and soaked at 400 ^{o}C for 30 min in nitrogen.

A similar procedure was applied to fabricate macroporous ITO films with pore size 70 nm. The required amount of indium tin nanohydroxide was 36 mg, and the 100 nm diameter PMMA aqueous colloidal solution had a concentration of 5.5 wt%. The co-assembly of PMMA and crystalline ITO nanoparticles required 36 mg of the ITO nanoparticles (inorganic content), dispersed in 1 mL water and mixed with 1 mL 5.5 wt% PMMA colloidal solution. For the co-assembly procedure with molecular precursors, 55 mg $InCl_3$ (0.249 mmol) and 9.7 mg $SnCl_4$ (0.036 mmol) were dissolved in 2 mL 5.5 wt% PMMA suspension. The deposited films were thermally treated at 400 ℃ in air to remove the PMMA templates, with a ramp of half a degree per minute and soaking time of 30 min.

Wide angle X-ray diffraction analysis was carried out in reflection mode using a Bruker D8 Discover diffractometer with Ni-filtered CuK_α-radiation (λ = 1.5406 Å), and equipped with a Vantec-1 position-sensitive detector. Scanning electron microscopy (SEM) was performed on a JEOL JSM-6500F scanning electron microscope equipped with a field emission gun, at 4 kV. UV-vis transmittance spectra were measured in a U-3501 Spectrophotometer (Hitachi) (4 nm resolution).

6.5. Chapter References

1. Fattakhova-Rohfing, D., et al., Transparent conducting films of indium tin oxide with 3D mesopore architecture. Advanced Materials, 2006. **18**(22): p. 2980-+.

2. Aksu, Y., et al., A Molecular Precursor Approach to Tunable Porous Tin-Rich Indium Tin Oxide with Durable High Electrical Conductivity for Bioelectronic Devices. Chemistry of Materials, 2011. **23**(7): p. 1798-1804.

3. Frasca, S., et al., Mesoporous Indium Tin Oxide as a Novel Platform for Bioelectronics. Chemcatchem, 2010. **2**(7): p. 839-845.

4. Yujing Liu, G.S., Jiri Rathousky, Oliver Hayden, Thomas Bein, Dina Fattakhova-Rohlfing, Nano-hydroxides as versatile primary units for the assembly of mesoporous indium tin oxide electrodes. submitted.

5. Chen, X., et al., Forced Impregnation Approach to Fabrication of Large-Area, Three-Dimensionally Ordered Macroporous Metal Oxides. Chemistry of Materials, 2010. **22**(12): p. 3583-3585.

6. Shchukin, D.G. and R.A. Caruso, Inorganic macroporous films from preformed nanoparticles and membrane templates: Synthesis and investigation of photocatalytic and photoelectrochemical properties. Advanced Functional Materials, 2003. **13**(10): p. 789-794.

7. Turner, M.E., T.J. Trentler, and V.L. Colvin, Thin films of macroporous metal oxides. Advanced Materials, 2001. **13**(3): p. 180-183.

8. Carreon, M.A. and V.V. Guliants, Ordered meso- and macroporous binary and mixed metal oxides. European Journal of Inorganic Chemistry, 2005(1): p. 27-43.

9. Velev, O.D., et al., Porous silica via colloidal crystallization. Nature, 1997. **389**(6650): p. 447-448.

10. Orilall, M.C., et al., Highly crystalline inverse opal transition metal oxides via a combined assembly of soft and hard chemistries. Journal of the American Chemical Society, 2008. **130**(28): p. 8882-+.

11. Arsenault, E., N. Soheilnia, and G.A. Ozin, Periodic Macroporous Nanocrystalline Antimony-Doped Tin Oxide Electrode. Acs Nano, 2011. **5**(4): p. 2984-2988.

12. Yang, Z., et al., Three-Dimensional Photonic Crystal Fluorinated Tin Oxide (FTO) Electrodes: Synthesis and Optical and Electrical Properties. Acs Applied Materials & Interfaces, 2011. **3**(4): p. 1101-1108.

13. Hatton, B., et al., Assembly of large-area, highly ordered, crack-free inverse opal films. Proceedings of the National Academy of Sciences of the United States of America, 2010. **107**(23): p. 10354-10359.

14. Mandlmeier, B., et al., Formation of Interpenetrating Hierarchical Titania Structures by Confined Synthesis in Inverse Opal. Journal of the American Chemical Society, 2011. **133**(43): p. 17274-17282.

Chapter 7

Bulk heterojuntion solar cells with nanostructured ITO electrodes

7.1. Introduction

Photovoltaic technology, converting sunlight into electricity, is being widely recognized as an essential component for future global energy production [1-4]. In the last few years, organic photovoltaic devices have been extensively investigated owning to their environmentally safe materials, low fabrication cost, as well as the predicted high device performance (energy conversion efficiency above 10%).

In a typical organic solar cell based on conjugated polymers as electron donor and fullerene derivatives as electron acceptor, photon absorption induces the generation of excited states (strongly bound 'electron-hole' pairs, called excitons)[2-3, 5]. These excited states can dissociate into free charges only at the interfaces of donor and acceptor materials, accompanied by rapid electron transfer from the donor to the acceptor. This is the process of charge separation or charge generation. Since the exciton diffusion length is only about 10 nm in many materials, some of the excitions are however not able to generate free charges if they cannot encounter the donor-acceptor interface within their lifetime. Thus, for efficient charge separation, a higher possibility for excitons to diffuse to the interface is required, which demands a dramatic increase in the interface area and reduction of the thickness of the phases involved. This is usually achieved by formation of a bulk heterojunction (BHJ) between the donor and the acceptor materials. Such a network of interpenetrating donor and acceptor phases features a large interface area thus facilitating the charge separation process, which can occur at many places in the BHJ layer [5].

There is however another process playing an equally important role in determining final photocurrents, namely charge recombination. The increased interface area enhances the meeting chances for opposite charges, resulting in a high recombination rate between electrons and holes. Therefore, to produce high photocurrents in the organic BHJ solar cells with minimized recombination, the separated charges should be removed from the interface to respective current collecting electrodes. This requires a fast transport of the separated charges to the current collectors.

One of the intensively explored approaches to decrease the recombination rate during the transport process while maintaining the large interface area is the generation of percolated charge transport pathways within the BHJ layer. It is mainly achieved by controlling the preparation conditions of the BHJ layer such as solvents, annealing treatment and deposition approaches [6-10]. Some other works were focused on vertically aligning the donor and acceptor phases by the nano-imprinting technique [11] or template-assisted fabrication methods [12] to create direct charge transport pathways.

Another recently proposed strategy to reduce the recombination rate during the charge transport process is to extend the 2D planar current collecting electrode (transparent conducting oxide film) into a 3D nanostructured electrode. Such morphology can accommodate photoactive BHJ material and shorten the charge transport distance within the polymer phases, which is expected to decrease the recombination rate between opposite charge carriers. A schematic description of this concept is presented in Figure 7.1. Instead of travelling across the BHJ layer composed of interpenetrating network between donor and acceptor materials, the separated charges can be transferred to the adjacent nanostructured matrix and be transported through the direct path towards the collecting electrode [13]. Thus, the chance for separated charges to encounter the interface is expected to be reduced. Furthermore, the nanostructured inorganic electrodes normally possess higher transport mobility compared to conjugated polymers and fullerenes. In the case of P3HT and PCBM, the mobilities are about 10^{-4} to 10^{-3} $m^2V^{-1}s^{-1}$, respectively. For comparison, the mobility of TiO_2 or ITO are several to tens of $m^2V^{-1}s^{-1}$. Additionally, due to the shortened actual charge transport distance and decreased recombination rate in this configuration, a thicker layer of photoactive BHJ material might be allowed. This will enhance the light harvesting ability, generating higher current density and, consequently, more efficient photovoltaic devices.

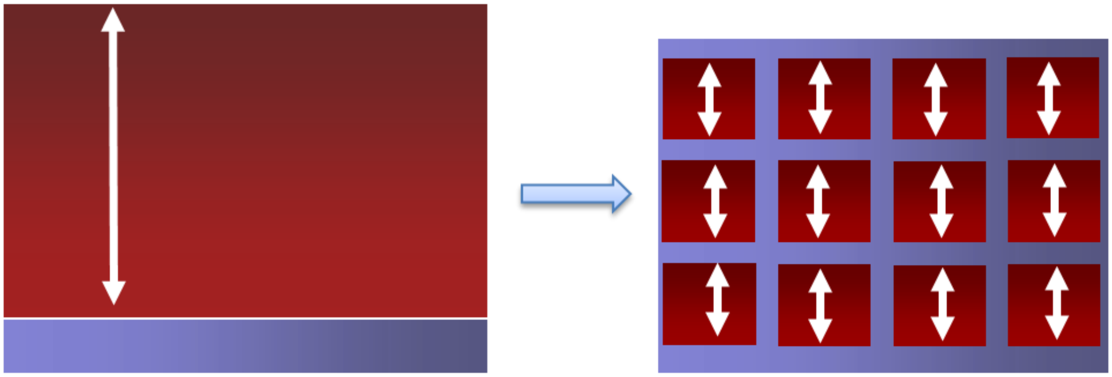

Figure 7.1 Schematic representations of the charge diffusion pathways (white arrows) to the current collector (blue) for a flat electrode (left) and 3D nanostructured electrode (right). The red part denotes the bulk heterojunction materials.

Several research groups have already examined the implementation of nanostructured TCO layers for different types of solar cells. Hupp et al. [14] and Joanni et al. [15] used ITO nanotubes prepared by hard templating in anodic aluminum oxide (AAO), and branched ITO nanofibers, respectively, as the 3D extended current collecting electrodes in dye-sensitized solar cells

(DSSCs). They found that the nanostructured electrodes are promising for improving photocurrent density. However, due to the limitation of modest light harvesting efficiency (dye absorption), the achieved device performance was still lower compared with their analogues fabricated from crystal TiO_2 photoanodes. Ozin [16] and Xu [17] have recently reported fabrication of macroporous antimony doped tin oxide (ATO) [16] and fluorine doped tin oxide (FTO) [17], respectively, aiming at their application as nanostructured transparent electrodes in organic solar cells. However, the proposed concept was not tested yet.

In this project, after demonstrating the fabrication of 3D macroporous indium tin oxide films possessing periodically organized large accessible pores (as described in chapter 6), we implemented them as nanostructured electrodes in a new type of BHJ solar cells. The solar cell performance was characterized by photocurrent-voltage measurements. To the best of our knowledge, this work is the first report on implementation of 3D nanostructured TCO electrodes in organic BHJ solar cells. Work on this project was performed in the group of Prof. Thomas Bein in cooperation with Prof. Lukas Schmidt-Mende. Dr. Oliver Hayden from Siemens, Erlangen has kindly provided P3HT and PCBM materials for the cell fabrication.

7.2. Results and discussion

In this project we have prepared the so called inverted organic solar cells according to a reported structure layout [18] (Figure 7.2), where planar ITO layer acts as the photoanode while the top electrode Ag acts as the cathode, due to their work function difference. In order to efficiently extract the separated charge carriers, the interfaces between photoactive layer and current collecting electrodes were modified with the so called charge selection layers [19]. For the collection of electrons, a thin dense n-type semiconductor layer, in our case titanium dioxide, was coated above the photoanode ITO film (see below for procedure); for the collection of positive charges, we deposited a very thin layer of WO_3 (3 nm) over the photoactive layer to assist the selection of holes. The photoactive layer was composed of regioregular poly(3-hexylthiophene) (P3HT) as the electron donor and the fullerene derivative [6-6]-phenyl-C61-butyric acid methyl ester (PCBM) as the electron acceptor. The polymer-fullerene blend with the thickness of about 250 nm was deposited by spin coating. The fabrication procedure of the cells (denoted further as inverted organic solar cells) was kept same for all the prepared samples, which have differed only in the morphology of the ITO bottom layer.

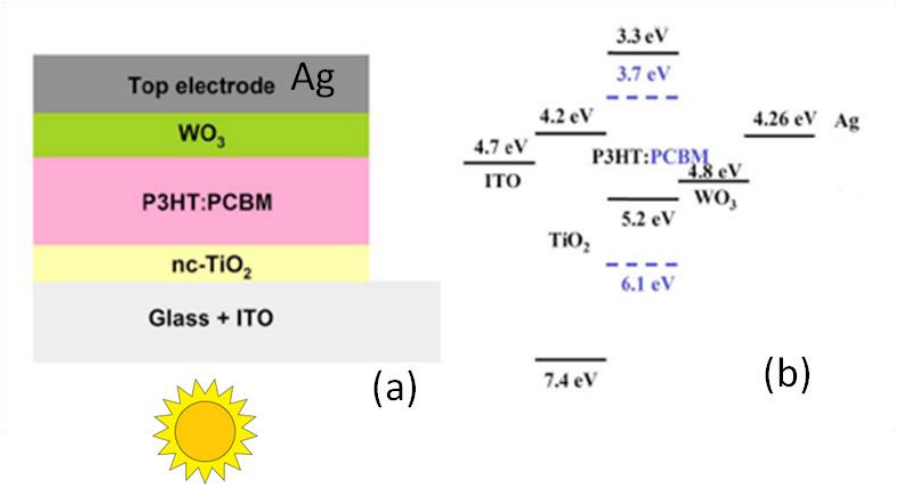

Figure 7.2 Layout of an inverted organic BHJ solar cell (a) and energy levels of materials involved in the device (b) [18]. The device is illuminated from the anode ITO side.

For fabrication of the solar cells with the nanostructured electrodes, the macroporous ITO films (synthetic details are given in chapter 6) were prepared on ITO glass substrates prior to the cell assembly (Figure 7.3). In order to investigate the influence of the morphology of the nanostructured ITO materials on the efficiency of current collection, we have prepared devices based on three different ITO electrode morphologies: (A) non-templated ITO films deposited from the suspension of indium tin hydroxide nanoparticles (thickness about 20 nm), (B) macroporous ITO films with the pore size of 70 nm (thickness about 80 nm), (C) macroporous ITO films with pore size of 250 nm (thickness about 60 nm). The reference cells were fabricated in the same way on commercial ITO glass substrates. The corresponding solar cells fabricated with different ITO electrodes are assigned as electrode-ref (commercial ITO substrate), electrode A (with the integration of non-templated ITO film), electrode B (with the integration of macroporous ITO film with pore size ca. 70 nm), and electrode C (with the integration of macroporous film with pore size ca. 250 nm).

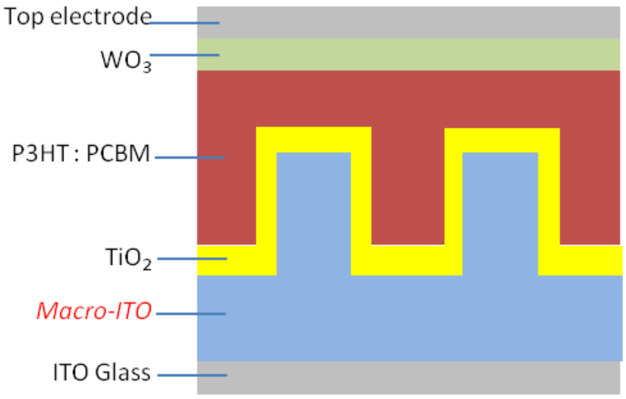

Figure 7.3 Layout of the inverted organic solar cell with the integration of nanostructured ITO electrodes.

7.2.1. Optimization of the titania electron selection layer

On comparison of solar cells fabricated with and without the layer of TiO$_2$, we noticed that the presence of the titania electron selection layer is very important for the efficient operation of the described inverted solar cells (Figure 7.4). The enhancement of device performance due to the presence of the titania selection layer could be explained with energy level differences between the materials involved in the device (Figure 7.2). The small difference in the energy of the LUMO level of PCBM and conduction band of TiO_2 favors the electron injection from PCBM to TiO_2, while the lower energy of the valence band of TiO_2 blocks the holes from flowing to ITO electrode. On one side, this process decreases the recombination between electrons and holes; one the other side, the accumulation of positive or negative charges forms an electrical potential difference across the BHJ layer, which is possibly useful for the dissociation of neutral excitons.

The properties of the titania layer such as its thickness, crystallinity and density are decisive for its performance as the efficient electron selection layer. Additionally, the quality of the titania layer coating over the ITO electrode is also important for the suppression of charge recombination processes.

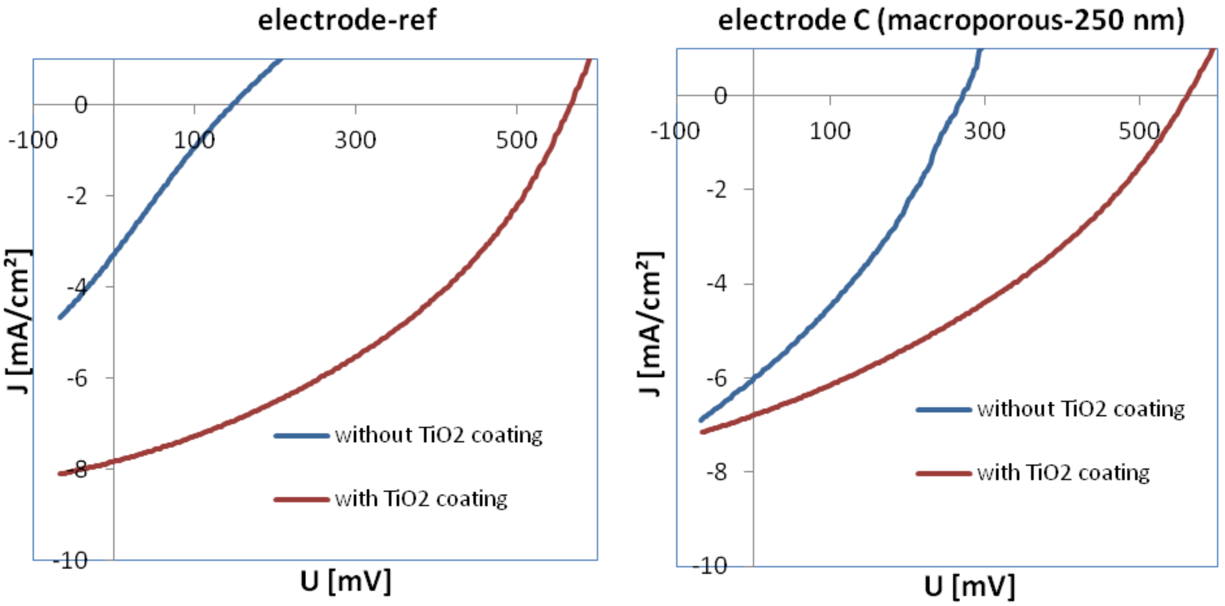

Figure 7.4 Influence of the titania electron selection layer on the photovoltaic performance of the inverted organic solar cells with different nanostructured ITO electrodes. Photocurrent–voltage curves of the cells with (left) electrode-ref: commercial flat ITO substrate and (right) electrode C: macroporous ITO layer with the pore size of 250 nm.

In order to optimize the coating parameters for the titania layer, we first kept the electron collecting electrode as commercial flat ITO substrates, and fabricated solar cells with TiO_2 layers deposited under different conditions. The optimized coating procedure was applied to fabricate solar cells with the integration of nanostructured ITO electrodes, which will be presented in the next part.

Titania thin layers were made following a sol-gel approach. The preparation conditions we have investigated include: (i) coating techniques, which involved immersion of ITO substrates in TEOT solutions and spin coating (Figure 7.5); (ii) annealing conditions, which included the annealing temperature and the annealing program (Figure 7.6); and (iii) the solution concentration of TEOT in absolute ethanol (30 mM, 60 mM and 86 mM) (Figure 7.7). Photocurrent-voltage curves illustrate the performance of solar cells fabricated according to the related parameters.

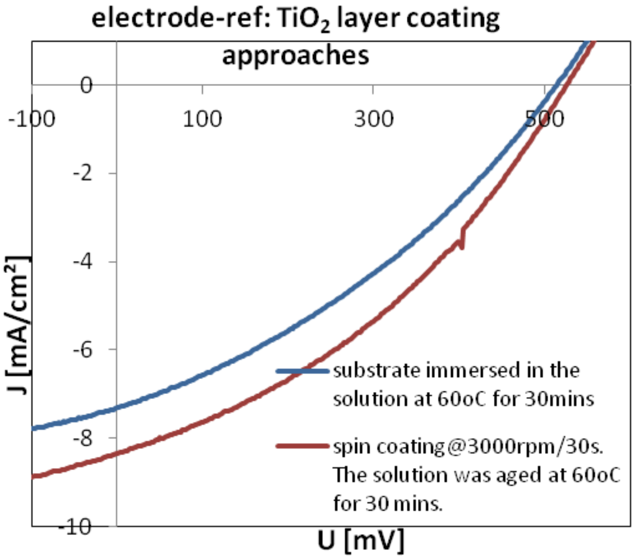

Figure 7.5 I-V curves of solar cells on electrode-ref. The titania layers were made by using different coating approaches: immersion (blue) and spin-coating (red). TEOT concentration 86 mM. The films were annealed at 300 ^oC for 30 min.

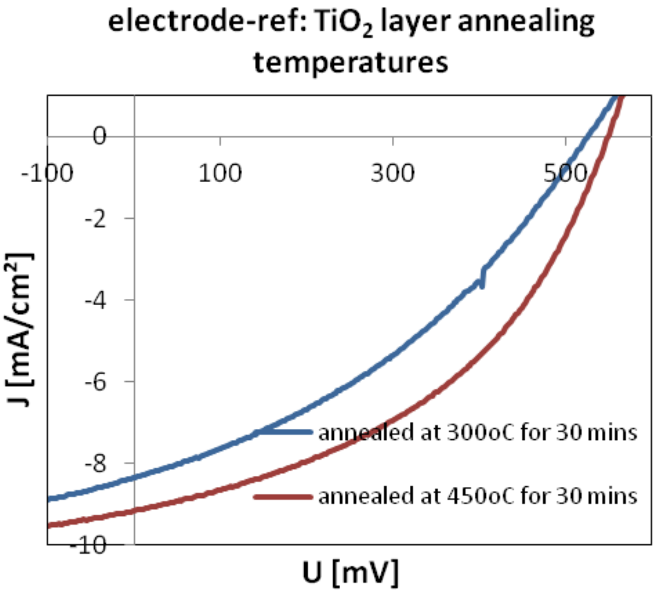

Figure 7.6 I-V curves of solar cells on electrode-ref. The titania layers were annealed at different temperatures: 300 ℃ (blue) and 450 ℃ (red). TEOT solution concentration 86 mM. The films were spin coated at 3000 rpm for 30s.

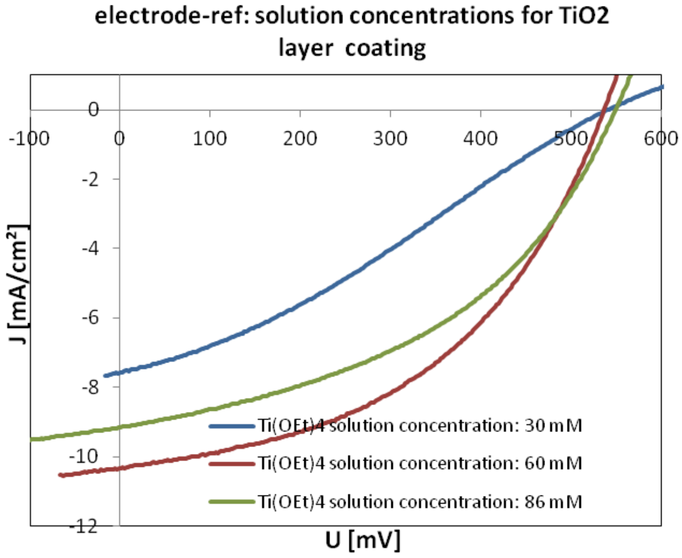

Figure 7.7 I-V curves of solar cells on electrode-ref. The titania layers were made from TEOT solutions with different concentrations: 30 mM (blue), 60 mM (red) and 86 mM (green). The layers were spin coated at 3000 rpm for 30s and annealed at 450 ℃ for 30 min.

On the base of solar cell performances, we selected the optimized parameters for the titania layer coating. It is the procedure involving a spin coating process of 60 mM concentrated $Ti(OEt)_4$ solution in ethanol and a further calcination step at 450 ^oC for 30 min.

7.2.2. Solar cells with the integration of nanostructured ITO electrodes

The optimized procedure for deposition of the titania electron selection layer described above was applied for coating the nanostructured ITO layers. Although the deposition of the titania layer was optimized for the flat ITO substrate based on the solar cell performances, the application of this protocol to the more complex porous electrode geometries still had to be examined. The morphology needed for the efficient solar cell performance requires a uniform coating of the nanostructure substrate with a very thin continuous titania layer. Undesired features to be avoided include filling of the pores with the titania material, formation of a dense titania top layer on the surface of the macroporous ITO, or the growth of disconnected titania crystals on the macroporous ITO scaffold.

The SEM images of the macroporous ITO layers show the same open porous morphology after deposition of the titania layer, without filling the pores and without formation of any dense titania layer on the top (Figure 7.8 b and e). The width of the plot profiles taken at the walls of the macroporous scaffold (250 nm pores) does not show obvious differences before and after the deposition of the titania layer (Figure 7.8 e), probably due to the very small thickness of the TiO_2 coating. However, the high resolution SEM image (Figure 7.8 f) suggests there is a homogeneous and continuous shell covering the inorganic scaffold. A more detailed characterization of the morphology and composition of the titania layer as well as the quality of the coating requires TEM investigation of the films’ cross-sections, which still has to be performed.

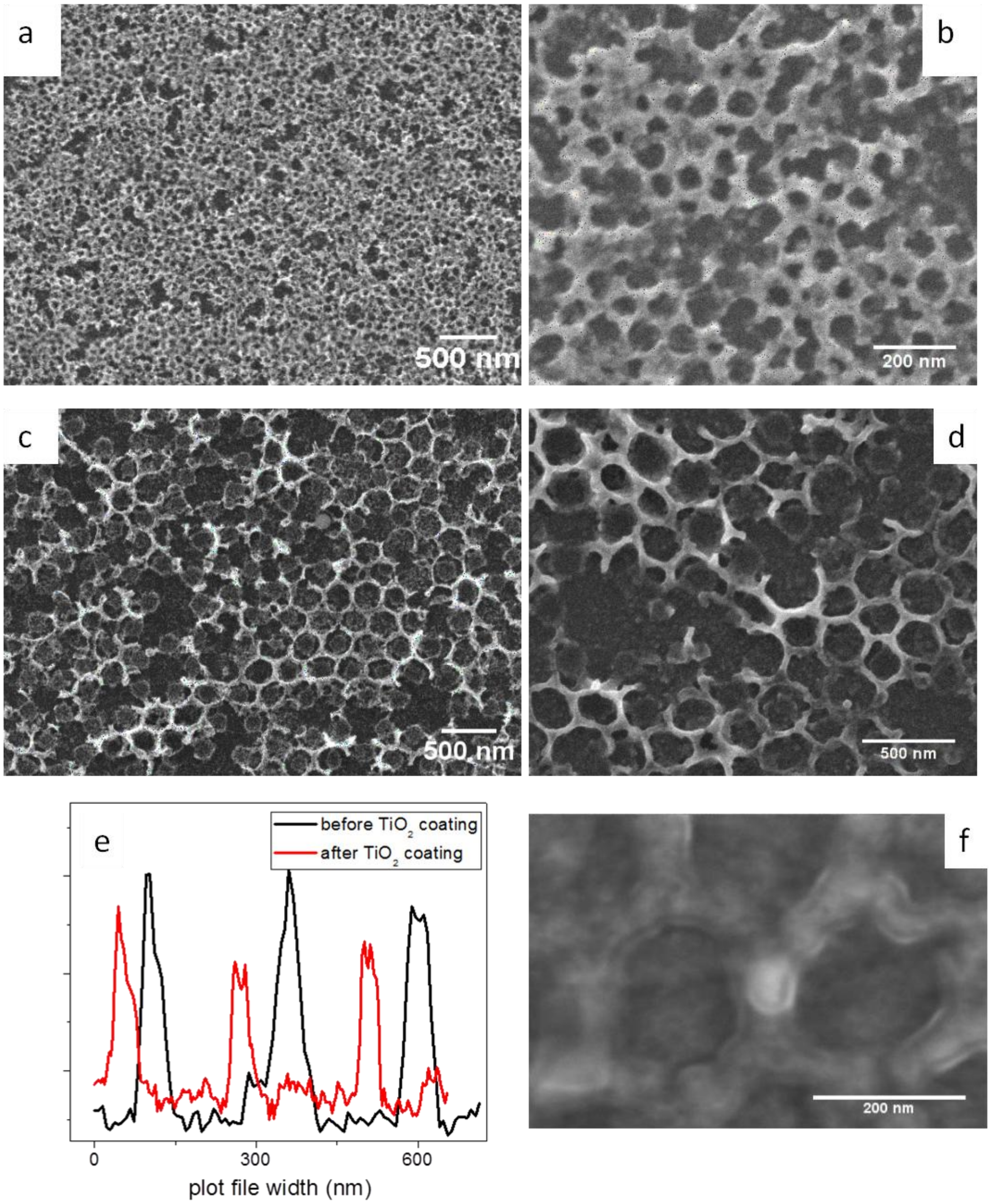
a
500 nm
b
200 nm
c
500 nm
d
500 nm
e
before TiO2 coating
after TiO2 coating
0
300
600
plot file width (nm)
f
200 nm

Figure 7.8 Macroporous ITO electrodes before (a, c) and after (b, d) deposition of the titania layer: macroporous ITO film with pore size 70 nm before (a) and after (b) titania coating, macroporous ITO film with pore size 250 nm before (c) and after (d) titania coating. (e) the wall thickness comparison with (red curve) and without (black curve) TiO_2 coating on the macroporous film with about 250 nm pore size. (the plots were made based on the image contrast and the peaks

denote the wall widths) (f) High resolution SEM image of TiO_2 coated ITO framework (macroporous ITO film with pore size 250 nm, after TiO_2 layer coating).

Titania-coated macroporous ITO electrodes were used for the assembly of inverted organic solar cells according to the procedure described above. Representative photocurrent-voltage (I-V) curves and average values of the basic photovoltaic characteristics are presented in Figure 7.9 and Table 7.1.

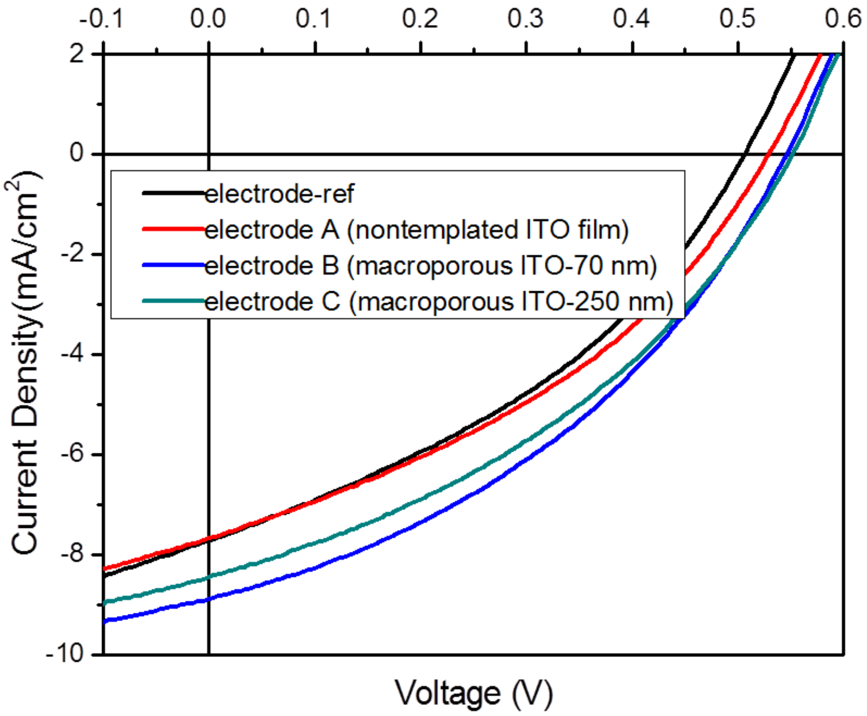

Figure 7.9 I-V curves of inverted organic BHJ solar cells with nanostructured ITO electrodes. Curve in black denotes the solar cell performance on electrode-ref (flat ITO substrate); curve in red denotes the solar cell performance on electrode-A (non-templated ITO film); curve in blue denotes the solar cell performance on electrode-B (macroporous ITO film with pore size 70 nm); curve in green denotes the solar cell performance on electrode-C (macroporous ITO film with pore size 250 nm).

Table 7.1 Solar cell performance parameters corresponding to Figure 7.9.

ITO electrodes	Isc (mA/cm^2)	Voc (mV)	FF(%)	Efficiency (%)
electrode-ref	6,6	500	37	1,22
electrode A (nontemplated ITO)	6.9	520	37	1,30
electrode B (macroITO-pores 70 nm)	7,8	546	38	1,58
electrode C (macroITO-pores 250 nm)	7,3	535	38	1,44

Note: The data are average values based on five different solar cells in the same batch. Detailed results of all the five solar cells can be found in Appendix II.

With the integration of nanostructured ITO layers, solar cells demonstrate increased short circuit currents I_{sc} and open circuit voltages V_{oc}, compared to their analogues made on flat ITO substrates (the amount of BHJ material is similar, as determined by Uv-vis absorpion). The maximum increase in the photocurrent is about 18%, from 6.6 mA/cm^2 for solar cell on electrode-ref to 7.8 mA/cm^2 for solar cell on electrode B (70 nm macroporous ITO film). For the solar cells on electrode C, 250 nm macroporous ITO film, an increase in short circuit current is also observed, from 6.6 mA/cm^2 to 7.3 mA/cm^2. The different increases in I_{sc} probably result from their pore size difference, since the macroporous ITO film with smaller pores (70 nm) features shorter periodicity, providing more efficient routes to collect the charges and transfer them to the flat ITO electrode, while the electrode with larger periodicity (250 nm) might weaken its possible advantage when concerning this aspect. Furthermore, for solar cells fabricated on electrode B, which is not able to efficiently accommodate BHJ material and offer short transport routes for electrons, the short circuit current shows a much weakened increase (from 6.6 mA/cm^2 to 6.9 mA/cm^2).

The measured open circuit voltages also exhibit improvements when comparing solar cells with nanostructured ITO electrodes and those without. The exact causes for such increases are not clear yet. To speculate, the nanostructure-based larger interface area between TiO_2 and BHJ materials might also be one reason, since ‘built in’ potentials generated at their interfaces could act as drift force for charge transport and enhance the process of charge separation. More insights are expected from a detailed solar cell analysis with other techniques such as impedance spectroscopy.

In this work, the values for short circuit currents and open circuit voltages are rather compatible with reported results on similar inverted solar cells; however fill factors are very low. The low fill factors are likely related with high interface resistances between different layers in the solar cells. Since the characteristic of low fill factor exists in our solar cells both with and without nanostructured ITO electrodes, at this point we attribute it to still imperfect solar cell fabrication procedures introducing defects.

Nevertheless, the above results suggest that the integration of a nanostructured electrode (macroporous ITO films) into organic photovoltaics can be a promising approach to enhance the current collection efficiency and device performance. To ultimately realize a larger increase of the photocurrent and efficiency, we will investigate thicker nanostructured electrodes with more volume for the accommodation of the BHJ phase.

7.3. Summary and outlook

The approach towards employing 3D nanostructured current collecting electrodes to accommodate photoactive material and collect the separated charges at a much shortened distance can be considered as separating the charge-collection function from the charge-generation function in organic bulk heterojunction solar cells. It has the potential to greatly decrease the charge recombination rates and enhance current collection efficiency, without sacrificing the large donor-acceptor interfaces required for efficient charge generation. The preliminary results described in this report provide first hints that this approach may indeed be feasible.

More specifically, by the implementation of macroporous ITO layers with pore size 70 nm and 250 nm, we successfully fabricated inverted organic solar cells with short circuit currents and open circuit voltages comparable to published results. Comparing with solar cells missing the macroporous ITO layers but otherwise from the same batch, the observed photocurrents increased by 18%, and energy conversion efficiency by 30%. Besides, instead of applying the expensive atomic layer deposition technique to coat the macroporous ITO films with TiO_2, we utilized a simple sol-gel approach and the solar cell results suggest that the coating is homogeneous and effective. More work to characterize the layer of TiO_2 will be necessary. Additionally, in the future thicker layers of nanostructured electrodes and included BHJ layers will be advantageous for demonstrating the potential of this concept.

7.4. Experimental part

To examine the influence of nanostructured ITO layers as 3D extended current-collecting electrodes in the organic solar cells, we only prepared macroporous ITO films with small thicknesses. This is a present limitation of the preparation technique because so far a larger surface roughness is always associated with a thicker layer and thus the solar cell is more prone to be short circuited. The nanostructured ITO layers were dip-coated on the ITO-coated glass substrate with a size of 1.5 cm × 2 cm. The films were then annealed to free the pores by a calcination in air, with a ramp speed of half a degree per minute and soaked at 400 ^{o}C for 30 min. More detailed information on the synthesis of macroporous ITO layers can be found in chapter 6.

For the fabrication of inverted OPV solar cells, we first coated the nanostructured ITO film with a thin layer of TiO_2 by the sol-gel approach. To prepare $Ti(OEt)_4$ solutions with concentrations 30 mM, 60 mM and 86 mM, 0.035 g, 0.070g, and 0.100g dry $Ti(OEt)_4$ was diluted in 5 mL absolute EtOH and then kept stirring for 1 hour. For the coating approach based on immersion, the nanostructured ITO films were immersed into the prepared solution and then held at 60 ^{o}C for 40 mins. After removal from the solution, the substrates were washed with absolute EtOH 3 times and dried with blowing air. For the TiO_2 layer deposited with the spin-coating method, the $Ti(OEt)_4$ solution was transferred into a 60 ^{o}C oven to age for 40 mins, after stirring for 1 hour at room temperature; thereafter the solution was used for spin coating after filtering with a 200 nm diameter filter; the spin coating speed was 3000 rpm, time 30 s; and the amount of solution was 50 uL for a substrate sized 1.5×2cm. TiO_2-coated films were heat treated in air at 300 ^{o}C for 30 min (ramp period of 8 hours) or at 450 ^{o}C for 30 min (ramp period of 11 hours).

The photoactive polymers poly(3-hexylthiophene) (P3HT) and the fullerene derivative [6-6]-phenyl-C61-butyric acid methyl ester (PCBM) were stored in an Ar filled glove box. To prepare the bulk hetero-junction (BHJ) solution, 20 mg P3HT and 15 mg PCBM were dissolved separately in 0.5 mL chlorobenzene in the glove box. Their solution mixture was kept stirring at room temperature for 3 days before use.The BHJ solution was coated on the TiO_2-coated nanostructured ITO layers and flat ITO substrates by a two-step spin coating process - 500 rpm for 1 min and then 800 rpm for 5 s to get a homogeneous layer. The obtained thickness was about 250 nm. The BHJ coated films were then annealed in Ar atmosphere at 140 ^{o}C for 5 min.

The hole extraction layer of 3 nm WO_3 and the top electrode (100 nm Ag) were deposited on top of the BHJ layer to complete the solar cell structure. These two layers were deposited by thermal evaporation of the material source WO_3 and Ag at a vacuum level of 10^{-6} mbar in the chamber. The distance between material source and deposition substrate was 15 cm. The WO_3 layers were evaporated at a speed of 0.01 nm/s, the Ag layer with a speed of 0.01 nm/s for first 10 nm, followed by 0.1 nm/s for the next 15 nm and then 0.2 nm/s until reaching 100 nm. The photocurrent voltage (I-V) characteristics of organic inverted solar cells were examined without a further annealing process.

The photocurrent voltage characteristics (I-V curves) of the solar cells were analyzed by using a Zahner Xpot setup with a self-made Lab-view program. The curves were recorded under illumination with an AM 1.5G solar simulator (power density was adjusted to 100 mW/cm^2 before the measurements). Solar cells were illuminated through a shadow mask, yielding an active area of 0.11 cm^2. The input bias voltage was varied from 100 mV to -600 mV.

7.5. Chapter references

1. Brabec, C.J., et al., Polymer-Fullerene Bulk-Heterojunction Solar Cells. Advanced Materials, 2010. **22**(34): p. 3839-3856.

2. Blom, P.W.M., et al., Device physics of polymer : fullerene bulk heterojunction solar cells. Advanced Materials, 2007. **19**(12): p. 1551-1566.

3. Hoppe, H. and N.S. Sariciftci, Polymer Solar Cells, in Photoresponsive Polymers II, S.R. Marder and K.S. Lee, Editor. 2008. p. 1-86. S.R. Marder and K.S. Lee

4. Helgesen, M., R. Sondergaard, and F.C. Krebs, Advanced materials and processes for polymer solar cell devices. Journal of Materials Chemistry, 2010. **20**(1): p. 36-60.

5. Benson-Smith, J. and J. Nelson, Nanostructured and photoelectrochemical systems for solar photon conversion. Chapter 7: Organic donor-acceptor heterojunction solar cells, 2008.

6. Hallermann, M., et al., Charge Transfer Excitons in Polymer/Fullerene Blends: The Role of Morphology and Polymer Chain Conformation. Advanced Functional Materials, 2009. **19**(22): p. 3662-3668.

7. Chen, D., et al., P3HT/PCBM Bulk Heterojunction Organic Photovoltaics: Correlating Efficiency and Morphology. Nano Letters, 2011. **11**(2): p. 561-567.

8. Janssen, G., et al., Optimization of morphology of P3HT/PCBM films for organic solar cells: effects of thermal treatments and spin coating solvents. European Physical Journal-Applied Physics, 2007. **37**(3): p. 287-290.

9. van Bavel, S., S. Veenstra, and J. Loos, On the Importance of Morphology Control in Polymer Solar Cells. Macromolecular Rapid Communications, 2010. **31**(21): p. 1835-1845.

10. van Bavel, S., et al., Relation between Photoactive Layer Thickness, 3D Morphology, and Device Performance in P3HT/PCBM Bulk-Heterojunction Solar Cells. Macromolecules, 2009. **42**(19): p. 7396-7403.

11. Wiedemann, W., et al., Nanostructured interfaces in polymer solar cells. Applied Physics Letters, 2010. **96**(26).

12. Chang, C.-Y., et al., Enhanced Performance and Stability of a Polymer Solar Cell by Incorporation of Vertically Aligned, Cross-Linked Fullerene Nanorods. Angewandte Chemie-International Edition, 2011. **50**(40): p. 9386-9390.

13. Fortunato, E., et al., Transparent conducting oxides for photovoltaics. Mrs Bulletin, 2007. **32**(3): p. 242-247.

14. Martinson, A.B.F., et al., Radial electron collection in dye-sensitized solar cells. Nano Letters, 2008. **8**(9): p. 2862-2866.

15. Joanni, E., et al., Dye-sensitized solar cell architecture based on indium-tin oxide nanowires coated with titanium dioxide. Scripta Materialia, 2007. **57**(3): p. 277-280.

16. Arsenault, E., N. Soheilnia, and G.A. Ozin, Periodic Macroporous Nanocrystalline Antimony-Doped Tin Oxide Electrode. Acs Nano, 2011. **5**(4): p. 2984-2988.

17. Yang, Z., et al., Three-Dimensional Photonic Crystal Fluorinated Tin Oxide (FTO) Electrodes: Synthesis and Optical and Electrical Properties. Acs Applied Materials & Interfaces, 2011. **3**(4): p. 1101-1108.

18. Tao, C., et al., Role of tungsten oxide in inverted polymer solar cells. Applied Physics Letters, 2009. **94**(4).

19. Ma, H., et al., Interface Engineering for Organic Electronics. Advanced Functional Materials, 2010. **20**(9): p. 1371-1388.

Chapter 8

Conclusions and Outlook

The main focus of this thesis was the development of nanostructured transparent conducting oxide (TCO) films with defined 3D porous morphologies featuring large interface areas, accessible pores and interconnected conducting frameworks. Such systems are of great interest as nanostructured transparent electrodes for various optoelectronic and electrochemical applications. The main strategy for the elaboration of the desired 3D porous TCO nanostructures was a templated self-assembly of crystalline TCO nanoparticles, which act as the nanostructure building blocks.

In chapter 3, based on the newly reported TCO system niobium doped titanium oxide (NTO), we have developed a novel nonaqueous solvothermal synthesis of NTO nanoparticles using *tert*-butanol as the reaction medium. The reaction of $Ti(Cl)_4$ and $Nb(OEt)_5$ with *tert*-butanol enables the preparation of crystalline doped and undoped titania nanoparticles with a narrow particle size distribution and homogeneous incorporation of doping atoms within the host lattice. Particle crystallinity and size can be controlled by adjusting the reaction temperature and time. Substitutional doping with niobium ions drastically increases the electrical conductivity of the titania particles from $2 \cdot 10^{-5}$ S/cm to 0.25 S/cm for the undoped and 20% Nb-doped particles, respectively. The mechanism of the electrical conductivity in such nanoparticles was investigated in collaboration with Dr. Hynek Nemec and Prof. Petr Kuzel from the Institute of Physics of the Academy of Sciences of the Czech Republic, Prague. Time-domain THz transmission spectroscopy and microwave impedance spectroscopy were used to investigate dielectric and conduction properties of undoped and Nb-doped TiO_2 nanoparticles in a wide frequency range

(20 MHz – 1 THz) and revealed that the transport of a vast majority of electrons in the doped samples is dominated by hopping between the reduced states and not by the free electron motion in delocalized conduction band states (see chapter 4).

The 4-5 nanometer-sized crystalline niobium doped titania nanoparticles are well dispersible in various solvents forming stable colloidal solutions. We have tested the applicability of the as-synthesized nanoparticles for the assembly of mesoporous films using the commercial Pluronic F127 polymer as a structure-directing agent. The obtained mesoporous NTO films feature a crystalline framework, uniform pore size of 10 nm, large surface area of 190 m^2/cm^3 and enhanced framework conductivity. The developed mesoporous NTO layers extend the library of available TCO nanoarchitectures which can be beneficial for different optoelectronic applications.

In order to develop the new nanostructured morphologies for the well established TCO system tin doped indium oxide (ITO), in chapter 5 we have worked out an alternative strategy to form crystalline mesoporous ITO materials which is based on the initial formation of indium tin hydroxide nanoparticles. The new type of crystalline indium tin hydroxides has been developed by using a solvothermal reaction in ethylene glycol as the solvent. The obtained particles are just a few nanometers in size, nearly spherically shaped and very well dispersible in water. Importantly, they can be transformed into the cubic bixbyite ITO phase at a mild temperature of 300 ^{o}C. Their assembly into periodic mesostructures directed by an amphiphilic polymer, and a subsequent transformation to mesoporous indium tin oxide are described in the chapter 5. To our knowledge, this is the first report on the preparation of mesoporous ITO films from pre-formed nanocrystals using the commercially available Pluronic templates. The resulting ITO layers can accommodate large amounts of redox-active molecules and serve as efficient conducting electrodes with a very high surface area.

The good dispersibility of the newly developed indium tin nanohydroxides in water further extends the choice of possible templates. In chapter 6, we describe a procedure for the fabrication of macroporous ITO films based on a co-assembly of aqueous colloidal suspensions of PMMA beads and the indium tin nanohydroxides. This procedure enables the fabrication of macoporous ITO films with periodically organized pores with 70 and 250 nm pore size, depending on the size of the PMMA beads. These films are characterized by a crystalline ITO framework, high electrical conductivity and optical transparency.

For the first time, we have employed the macroporous ITO films as nanostructured electrodes in inverted bulk heterojunction organic solar cells aiming at reducing the recombination loss via shortening the charge transport distance, as described in chapter 7. The preliminary results indicate that this strategy of enhancing current collection by nanostructuring the current collector leads to an increased solar cell efficiency, and is very promising for further optimization of device performance. Work in chapter 7 builds the basis for further development and optimization of this concept.

To summarize, we have developed novel synthesis strategies for the formation of ultra-small and well-dispersed crystalline nanoparticles based on two different TCO systems. Assembly of these nanoparticeles with templates of amphiphilic block copolymers and PMMA colloids allows the fabrication of nanostructured TCO electrodes with various periodically organized pores and nanoscale pore sizes. Their structural advantages including large interface area, accessible inner spaces and conductive framework are expected to lead to enhanced device performance in the fields of electrochemistry and photovoltaic technology.

Appendix I

Table AI1: Output of the PRO-FIT program giving the refined least-squares parameters (the Bragg angle positions ($2\theta_B$)), FWHM values and integrated intensities of the diffraction lines) for the as-prepared indium tin hydroxide in the three selected 2θ regions containing 5 to 6 diffraction maxima.

Line	Individual profile fitting results (PRO-FIT)			
	$2\theta_B$	FWHM	Integrated intensity	R_{wp}
1	18.69(2)	2.86(7)	37549 ±1067	0.022
2	22.34(1)	1.17(1)	80634 ±744	
3	24.85(1)	2.87(3)	136284 ±1436	
4	28.97(1)	2.66(5)	43302 ±910	
5	33.66(1)	2.45(3)	71576 ±946	
6	36.41(3)	2.68(3)	19849 ±503	
7	41.12(2)	2.37(4)	10235 ±231	0.020
8	45.51(1)	1.21(2)	11001 ±239	
9	49.24(1)	3.45(2)	64069 ±338	
10	52.60(1)	3.06(2)	65540 ±399	
11	54.75(1)	3.86(2)	87257 ±414	
12	58.16(3)	2.67(7)	12931 ±313	
13	63.67(4)	1.72(9)	1546 ±102	0.015
14	69.60(1)	3.69(2)	30827 ±178	
15	73.42(3)	3.51(5)	10196 ±142	
16	76.76(1)	3.20(2)	26328 ±163	
17	80.64(2)	2.32(5)	4651 ±147	

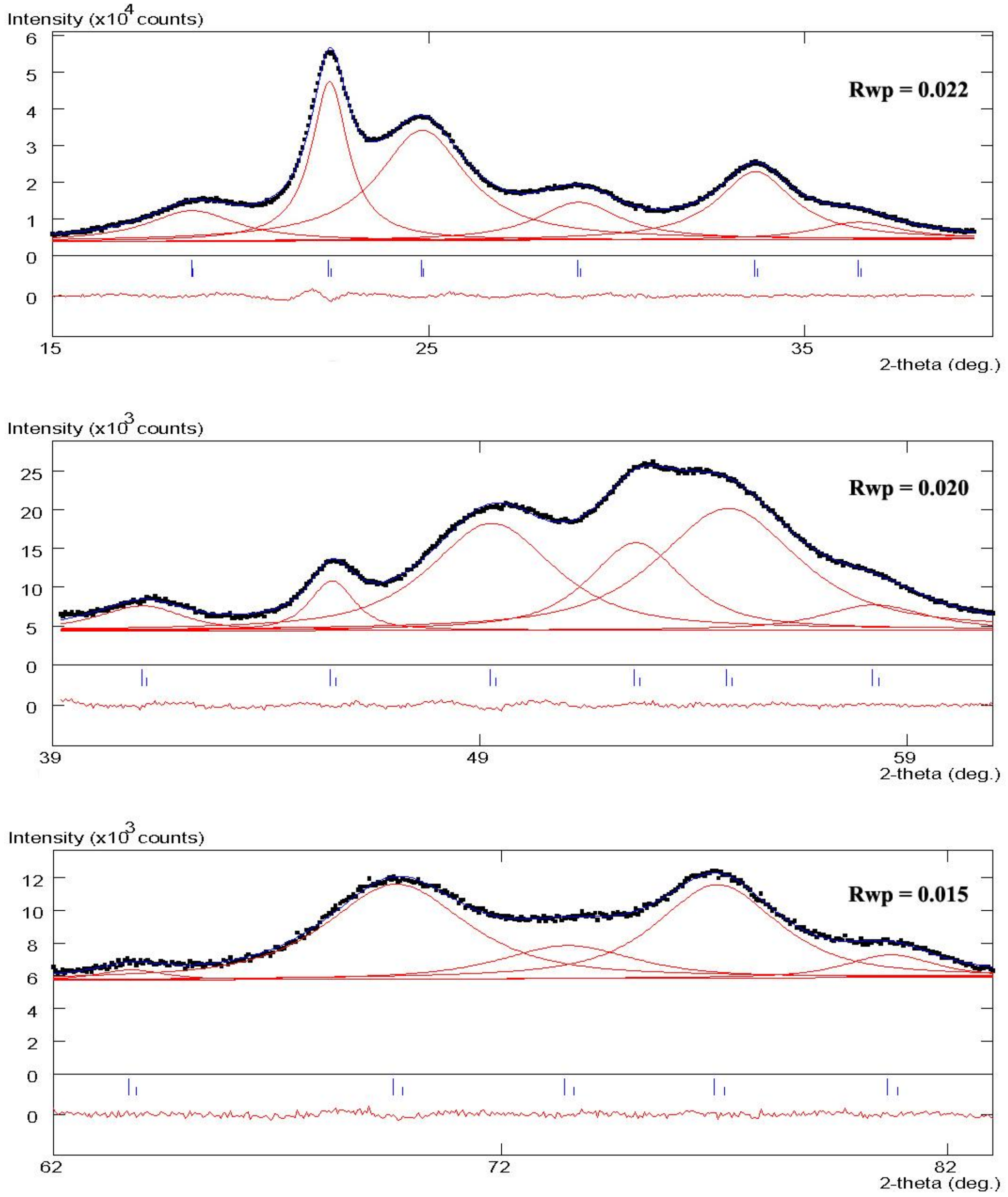

Figure AI1. Individual profile-fitting results for the as-prepared indium tin hydroxide in the three selected 2θ regions containing 5 to 6 diffraction maxima. The observed data are represented by black squares, the calculated profile for each diffraction line by red lines, the total calculated profile by a blue line, the difference between the observed and calculated profile by the red line at the bottom of the diagram on the same scale as the above. Long and short vertical bars mark the Cu $K\alpha_1$ and Cu $K\alpha_2$ positions of the reflections, respectively.

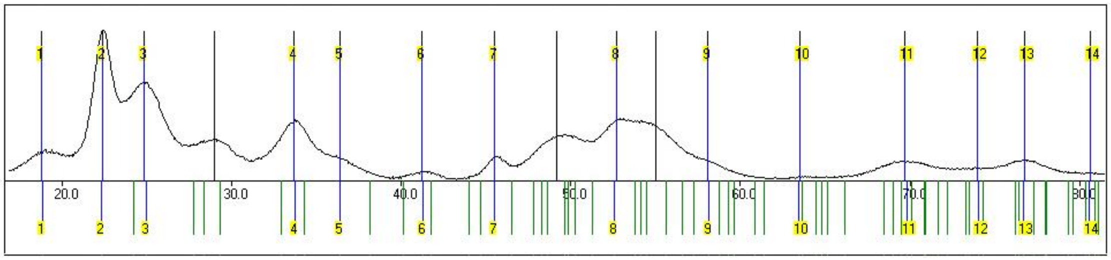

Figure AI2. The relation between the positions of the diffraction maxima in the XRD pattern of the as-prepared indium tin hydroxide and calculated diffraction line positions for the hexagonal lattice proposed by Qiu et al. [1] (program CheckCell). Black vertical bars above and green vertical bars below marks the positions of the observed and calculated diffraction lines, respectively. In case where the positions of the observed and calculated lines are almost the same (within a 2θ range of ±0.15°) the color of the bars is blue.

[1] Qiu, Y.; Bellina, P.; Jeurgens, L. P. H.; Leineweber, A.; Welzel, U.; Gerstel, P.; Jiang, L. Q.; van Aken, P. A.; Bill, J.; Aldinger, F., *Adv. Funct. Mater.* **2008,** *18*, 2572-2583.

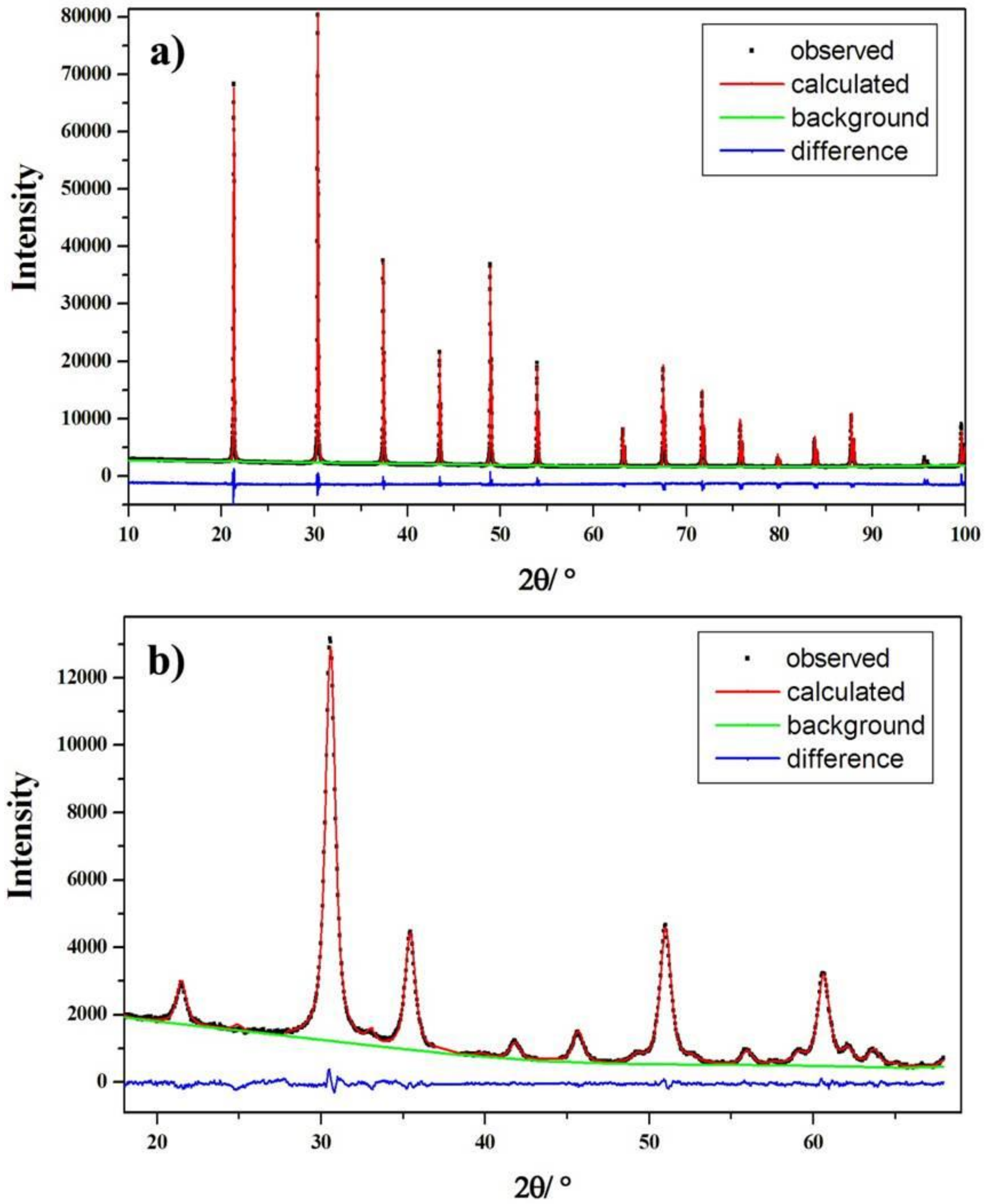

Figure AI3. The result of whole-powder-pattern profile refinement of (a) LaB_6 standard (R_{wp} = 0.050), used for the determination of the instrumental profile in line-broadening analysis, and (b) the mesoporous ITO film prepared from the preformed nano-hydroxides and treated at 300 ℃ in air followed by a treatment at 300 ℃ in N_2/H_2 (R_{wp} = 0.025). In the refinement of the ITO sample, 2θ regions from 37.0 ° to 38.5 ° and from 43.2 ° to 44.5 ° were excluded due to the presence of diffraction lines of the substrate.

Appendix II

Table AII1: The inverted BHJ solar cell performance with nanostructured ITO electrodes

OPVs	Isc	Voc	FF%	PCE%
Ref.1	6.3	486	37	1.13
Ref.2	6.14	490	39	1.16
Ref.3	6.52	507	37	1.21
Ref.4	7.02	506	37	1.31
Ref.5	6.86	507	37	1.28
Nonporous ITO-1	6.98	529	37	1.37
2	7.36	501	36	1.33
3	6.8	510	36	1.25
4	6.95	532	36	1.31
5	6.41	527	37	1.24
MacroITO-ca.70 nm-1	7.51	533	37	1.46
2	7.72	555	38	1.6
3	7.87	561	38	1.65
4	8.08	546	39	1.7
5	7.58	534	36	1.46
MacroITO-ca.250 nm-1	7.68	552	38	1.60
2	6.61	547	36	1.29
3	7.12	548	38	1.48
4	7.33	463	39	1.28
5	7.43	563	36	1.51

Publications and Presentations

1. Y. Liu, et.al. Nano-hydroxides as basic units for the assembly of macroporous indium tin oxide layers and their application in organic photovoltaics, in preparation.
2. Y. Liu, G. Stefanic, J. Rathousky, O. Hayden, T. Bein, D. Fattakhova-Rohlfing Nano-hydroxides as versatile primary units for the assembly of indium tin oxide mesoporous electrodes. Submitted to RSC journal Chemical Science.
3. Y. Liu, J. M. Szeifert, J.M. Feckl, B. Mandlmeier, J. Rathousky, O. Hayden, D. Fattakhova-Rohlfing, T. Bein. *ACS Nano* **2010**, 4, 5373-5381.
4. J. M. Szeifert, J.M. Feckl, D. Fattakhova-Rohlfing, Y. Liu, V. Kalousek, J. Rathousky, T. Bein. *J. Amer. Chem. Soc.* **2010**, 132, 12605-12611.
5. H. Němec, Z. Mics, M. Kempa, P. Kužel, O. Hayden, Y. Liu, T. Bein, D. Fattakhova-Rohlfing. *J. Phys. Chem. C* **2011**, 115, 6968-6974.
6. Y. Liu et.al. Niobium doped titania nanoparticles: synthesis, assembly into mesoporous films and electrical conductivity. NANO 2010, Rome, Italy (oral presentation).
7. Y.Liu et.al. Niobium doped titania nanoparticles: synthesis, assembly into mesoporous films and electrical conductivity. Deutsche Zeolith-Tagung 2011, Erlangen, Germany (poster).
8. Y. Liu et.al. Nano-hydroxides as basic units for assembly of macroporous ITO layers and their application in organic photovoltaics., CeNS workshop 2011, Venice, Italy (poster).

Curriculum Vitae

Basic information:

Name: Yujing, Liu (family name)

Birth date and place: 14.09.1985, Henan, China

Nationality: Chinese

E-mail: yujing.liu85@gmail.com

Education background:

Oct. 2008 –	Ludwig-Maximilians-Universität München (LMU), Germany
March 2012	PhD candidate in Physical Chemistry
August 2006 – July 2008	Tsinghua University, Beijing, China
	Master of Engineering in Materials Science and Engineering
Sept. 2002 –	China University of Geosciences, Beijing, China
July 2006	Bachelor of Engineering in Materials Science and Engineering

Scholarships:

DAAD/Siemens Scholarship for Post-graduate Research Project (2008.10-2012.03)

Scholarship for General Excellence of Tsinghua University (2007)

Outstanding Graduate of China University of Geosciences, Beijing (2006)

Top Ten Excellent Students of China University of Geosciences, Beijing (2005)

Scholarship of Chinese Academy of Sciences (2005)